CFD SIMULATION OF AN OVERTAKING MANEUVER USING SIMPLIFIED VEHICLE BODIES

by

Arune Dhiren Chellaram

A thesis submitted to the faculty of
The University of North Carolina at Charlotte
in partial fulfillment of the requirements
for the degree of Master of Science in
Mechanical Engineering

Charlotte

2016

Approved by:

_____
Dr. Mesbah Uddin

_____
Dr. Peter Tkacik

_____
Dr. Jerre Hill

ABSTRACT

ARUNE DHIREN CHELLARAM. CFD Simulation of an overtaking maneuver using simplified vehicle bodies. (Under the direction of DR. MESBAH UDDIN)

When two vehicle bodies are involved in a passing maneuver, interesting and intricate aerodynamic interactions occur between them. This has been an area of active interest in Motorsports for quite some time. The existing literature shows only few studies in this area, and, as such, very little is known about the complex aerodynamics of racing in proximity. The aim of this thesis is to develop a Computational Fluid Dynamics (CFD) methodology capable of describing the transient effects that occur in this scenario, and to subsequently analyze the flow field. This is achieved by simulating the flow over two tandem simplified vehicle bodies (the Ahmed body) in a virtual wind tunnel where one body is kept stationary while the other was allowed to move in the longitudinal direction with a small velocity. In order to achieve reliable CFD results when one of the solid objects is moving, a new meshing methodology, called the Overset mesh model, was implemented in the CFD process. The simulations were run using a commercial finite volume CFD code Star-CCM+ using the unsteady Reynolds Averaged Navier-Stokes (URANS) solver. The collected CFD statistics include all time dependent vehicle aerodynamic performance parameters like drag, lift, side-force, and three moment coefficients, in addition to the full 3D description of the flow field surrounding the two vehicles. Additionally, the CFD results were compared against fully transient and quasi-steady-state experimental results, and encouraging correlations between the CFD and experiments were observed. The

veracity of the CFD work presented in this thesis provided significant insight into the complex aerodynamics of a passing maneuver, and lays the foundation for further analysis in this area using more complex vehicle shapes and more complex tandem racing or passing maneuvers at a yaw angle.

ACKNOWLEDGMENTS

I would like to begin by thanking my advisor, Dr. Mesbah Uddin, for his constant guidance and motivation throughout the course of this thesis. His inputs and advice helped steer this research to its final goal. I would also like to thank Dr. Peter Tkacik and Dr. Jerre Hill for taking the time to review my thesis and offer their valuable insights. I'm grateful to the team members at CD-ADAPCO, specifically Mr. Chao Zhang and Mr. Bradley Shields, who aided me greatly in understanding the intricacies of using the overset mesh during the initial stages of this thesis. Finally, I would like to thank the Mechanical Engineering department of UNCC, and the College of Engineering as a whole for the tremendous amount of support I have received through the course of my research.

TABLE OF CONTENTS

LIST OF FIGURES

LIST OF TABLES

CHAPTER 1: INTRODUCTION

1.1 Vehicle Aerodynamics

Modern vehicles, especially race cars, are extremely complicated aerodynamic devices. Vehicle bodies simultaneously undergo effects of drag, lift, and side forces, all while being in very close proximity to the ground, further complicating the air flow patterns around them. Subtle changes in these flow patterns around vehicle bodies can result in large changes in various factors of vehicle dynamics, including the handling and stability of the vehicle. As a result the study of vehicle aerodynamics has become a field of great interest to many researchers. Studies on vehicle aerodynamics have been conducted for decades using wind tunnels, and more recently Computational Fluid Dynamics (CFD), to understand what the factors affecting vehicle aerodynamics are and the results of these effects. The studies have ranged from simple flows around single vehicle bodies to studies to understand the effect of multiple vehicles traveling in close proximity to each other under more complicated flow conditions.

The increase in capability of CFD simulations has allowed for the undertaking of even more intricate situations, and has allowed automotive developers to model the flow structures around vehicle bodies to a far greater extent than ever before.

1.2 Motivation

Whether on the racetrack or the highway, vehicle bodies are in constant aerodynamic interaction with each other. When two vehicle bodies pass within close proximity of each other, these interactions result in intricate changes in the aerodynamic fields surrounding both bodies. These changes can result in excitations to either body about its rolling, pitching, and yawing axes, the exact causes and effects of which have yet to be fully analyzed. In order to understand the underlying causes of these effects studies have been conducted involving two or more vehicle bodies in tandem. These studies were most often run in steady state, with the vehicle bodies kept at constant location relative to each other, and the flow patterns analyzed. While these studies have provided great insight into some of the more complicated flow structures generated around vehicle bodies, they do not fully model the transient effects that occur during an actual overtaking maneuver.

Modeling these transient effects in a wind tunnel has long been an expensive and difficult procedure; requiring one body to be in constant motion in a wind tunnel is almost impossible using full-scale vehicle bodies, and almost as difficult even with smaller scale models. Relatively few studies exist that attempt to model these transient effects in the wind tunnel ([1]). Considering the frequent overtaking maneuvers occurring both on the racetrack and the highway, the relative lack of information for this situation is difficult to comprehend.

CFD has helped to bridge some of the gaps in this knowledge. As with wind tunnel tests, several CFD simulations have been conducted with vehicles kept static

relative to each other, to analyze the effects their relative positioning to each other has affected the flow patterns around the bodies ([2], [3]). In addition, simulations depicting the two bodies in a series of relative position to each other (known as the quasi-steady approach) have been conducted as an attempt to model the overtaking maneuver. These simulations resulted in an even greater understanding of the effects of overtaking than before, but still could not fully describe the overtaking maneuver and its effects.

More recently, some studies have been conducted using CFD tools such as the sliding mesh to model an overtaking maneuver ([4], [5]). These simulations have gone a large way toward capturing the elusive transient effects that the quasi-steady simulations couldn't, and have resulted in a much better understanding of the overtaking maneuver than ever before. The sliding mesh simulations, however, are computationally demanding and require very fine meshing in almost all regions of the computational domain to fully capture the flow, resulting in the costs being prohibitive for most purposes.

With the aim of offering a more cost-effective and accurate solution than is currently available, an attempt to model an overtaking maneuver using a new meshing method, "The Overset Mesh", was undertaken. The overset mesh allowed for a refined mesh to be generated in only the areas of interest during the overtaking maneuver, and additionally allowed for the movement of the mesh as though it were a rigid body. This allowed for the refinement of the mesh around the vehicle bodies, which were the areas of most interest, while maintaining a reasonable domain size for the rest of the simulation. The ability to move the overset mesh along with the body ensured

that the flow around the body itself was captured fully.

The overset mesh method of modeling the overtaking maneuver proved a success, capably capturing the flow patterns and aerodynamic coefficient around both bodies, and matching well with the data available. This information can now be used to analyze how the different factors involved in an overtaking maneuver, such as body spacing, relative velocity, and angle of yaw affect the aerodynamic characteristics of the two vehicles involved in the overtaking maneuver.

1.3 Organization of Thesis

Chapter 1 Indicated the motivation for this thesis.

Chapter 2 provides a background of the various studies conducted relating to the overtaking maneuver. A brief background of the Ahmed body and the reasons for its selection in this experiment is also included.

Chapter 3 highlights the simulation setup used for this research, as well as an overview of the various computational models and meshing methods used through the course of the project.

Chapter 4 begins with the post processing of the data gathered to make it easier to analyze, as well as a look at the raw data gathered from the simulation. The data is then analyzed at various points of interest throughout the overtaking maneuver.

Chapter 5 highlights some of the conclusions reached in Chapter 4, as well as providing a scope for further analysis of the work contained within.

CHAPTER 2: OVERVIEW OF FLOW PAST SIMPLIFIED BODIES

2.1 The Ahmed Model

For decades the study of ground vehicle aerodynamics has been a source of great interest to researchers, however the variety in designs of vehicles made it very difficult to accurately model the aerodynamic behaviors associated with these bodies. To help combat this, Ahmed et al. [6] introduced the Ahmed body, a simplified bluff body with shape characteristics that broadly resemble those of a ground vehicle, which could be used to study the various aerodynamic phenomena occurring on a vehicle. The Ahmed body can be seen in figure 1. Ahmed et al. tested the Ahmed body in a wind tunnel at various ranges of slant angle ψ to ascertain the effects this angle had on the flow characteristics around the vehicle.

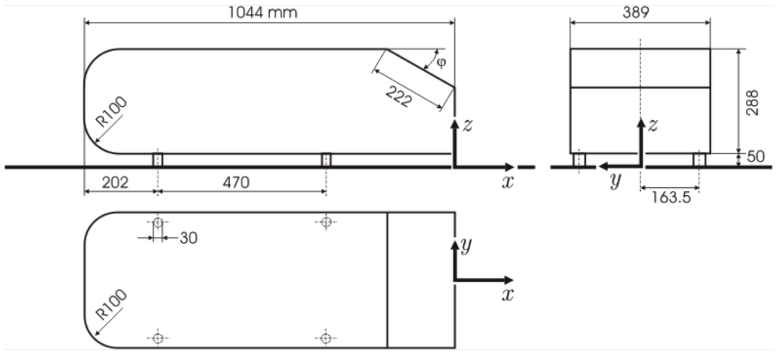

Figure 1: The Ahmed body $\psi = 25^o$ [7]

While varying the slant angle to understand its effects on the flow characteristics around the vehicle, Ahmed et al. found that almost 85% of the drag induced on the

body was due to pressure drag generated at the rear end of the vehicle body. A system of horseshoe vortices was generated at the rear of the vehicle, and the characteristics of these vortices were dependent on the slant angle (ψ) at the rear of the body. A plot of the drag coefficients associated with various slant angles is shown in figure 2. The pressure and force measurements were gathered by connecting the model to a strain gauge below the ground plain.

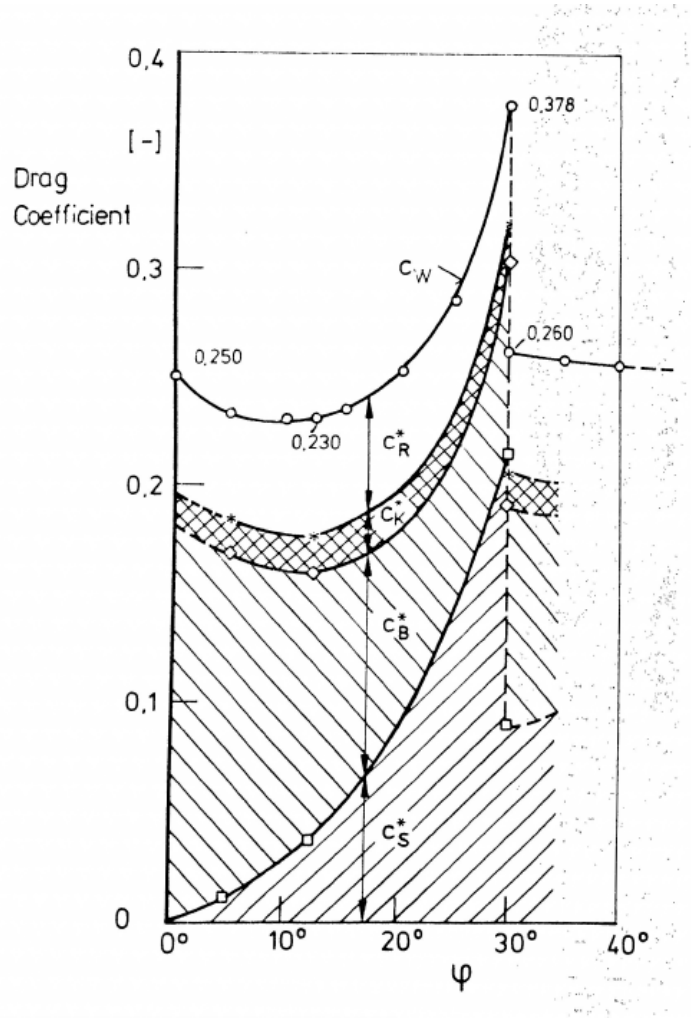

Figure 2: Variation in drag coefficient (C_D) values with base slant angle (ψ) [6]

While the relatively simple geometry of the Ahmed body make it an excellent tool, it is the complex flow structures it generates in its wake that explain its widespread

use in CFD analysis. As described by Ahmed et al., the slant angle at the rear of the vehicle had a strong effect on the vortex structure at the rear of the body. These complications in the wake structure of the Ahmed body are strongly dependent on the slant angle. As described earlier, the drag coefficient of the Ahmed body reaches a peak at a slant angle of 30^o. Below this angle, strong counter-rotating vortices are generated at the rear of the body, and there is separation of the flow along the top edge. This flow then reattaches further down the slope. For cases above the critical slant angle, however, these counter-rotating vortices are significantly weaker and no reattachment occurs [8].

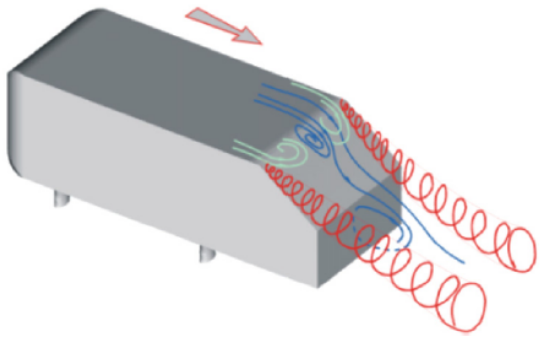

Figure 3: Development of the flow in the wake of the Ahmed body with slant angle 25^o [9]

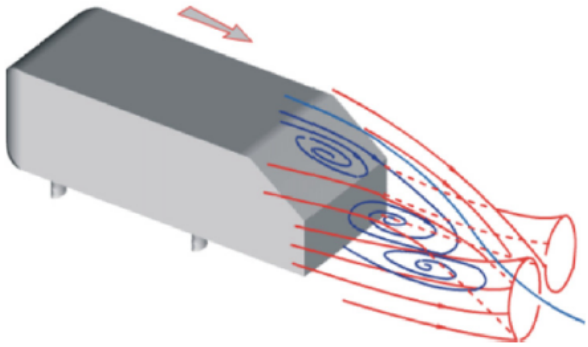

Figure 4: Velocity profile in the wake of the Ahmed body with slant angle 35^o [9]

Hinterberger et al. [8] conducted Large Eddy Simulations (LES) on an Ahmed body with slant angle 25^o to try and recreate the structures described above, and understand their evolution. Hinterberger found that the LES simulation very accurately predicted the flow structures in the wake of the Ahmed body, as shown in figure 5.

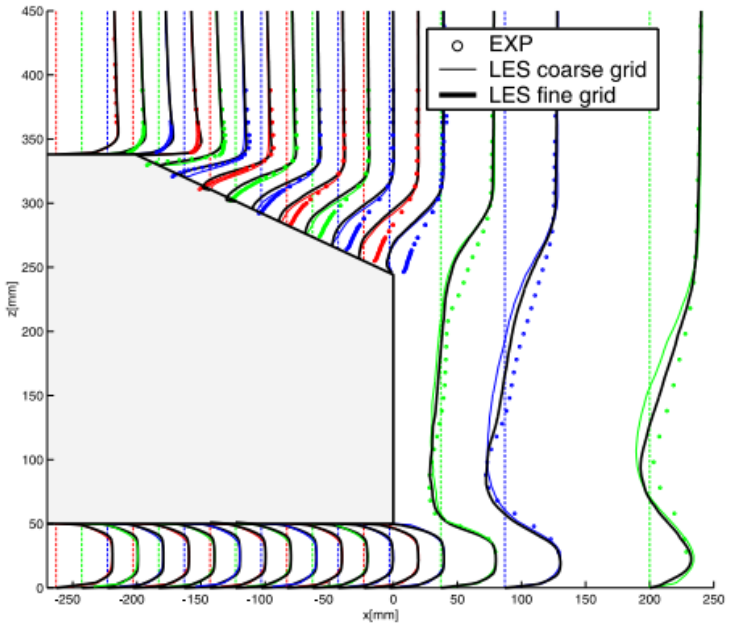

Figure 5: Development of the flow in the wake of the Ahmed body with slant angle 35^o [8]

Minguez et al. [10] also conducted experiments on the Ahmed body using LES, and once again found that the flow structure generated using this method matched very well with those gained from the experiments, however the system continually over-predicted the drag coefficient of the body. Higher resolution grids would be required to more accurately capture the boundary layer than the ones used in the simulation, and help to more accurately predict the drag. However, attempting to fully capture this boundary layer would result in grids that were far too computationally expensive when coupled with the LES solver. As a result the LES system was useful in describing

the flow structures around the Ahmed body very accurately, but not in solving for the aerodynamic coefficients of the body.

To better understand the flow patterns in the wake of the Ahmed body, Kapadia et al. [11] conducted Detached-Eddy Simulations (DES) on Ahmed bodies with slant angle of 25^o and 35^o, using the commercial solver Cobalt. They found that while DES simulation came very close to the experiment in predicting the drag values for the body, it did not accurately display the causes for this drag. The DES simulation over-predicted the drag at the rear of the body, while under-predicting it at the front. This was due the the DES simulation weakening the boundary layer of the flow around the body and allowing it to separate, subsequently weakening the vortices in the wake of the body for the 25^o slant angle case. In addition, the DES simulation had to use the single equation Spalart-Allmaras model for the flow due to the already high computing power required for DES. This resulted in some of the discrepancies between the expected aerodynamic coefficients, and the simulation results.

Guimineau [9] studied the flow around the Ahmed body using the less demanding Reynolds Averaged Navier-Stokes (RANS) equations, and a range of turbulence models. In the simulations for the body with slant angle 25^o, Guimineau was unable to exactly match the values predicted by the experiment, due to the simulation not displaying the reattachment of the flow along the slope of the Ahmed body. However the simulations for the 35^o slant angle matched extremely well with the experimental values. Guimineau also demonstrated that the RANS solver was capable of depicting the flow structures in the wake of the Ahmed body accurately, and could therefore provide a strong tool for the analysis of the flow.

The characteristics of the Ahmed Body were further explored by Serre et al. [7]. Their simulation involved a CFD analysis of the flow around an Ahmed Body with a slant angle of 25^o using both DES and LES simulations. Serre et al. determined from experiments that the drag coefficient for an Ahmed body in this configuration was supposed to be 0.298, however their simulations resulted in drag coefficients that were significantly higher at the chosen Reynolds number of $7.68\text{x}10^6$.

In their study Serre et al. [7] demonstrated that the LES method agreed with the experimental results at low Reynolds numbers, but could not achieve this at higher Reynolds numbers due to an unresolved boundary layer over the top of the Ahmed body. Rectifying these discrepancies would require the use of a much finer grid, causing the simulation to become extremely demanding computationally. While the DES required less computational power, it could not predict the values of the aerodynamic coefficients as accurately as the LES simulations in this case.

In order to further elucidate the complex flow structures in the near wake of the Ahmed model, Watkins et al. [12] conducted both time-averaged and time-dependent investigations of the Ahmed model in a wind tunnel. The study found that while the time averaged results matched extremely well with all of the previous studies conducted on the Ahmed body in the far wake, some complex structures were found in the near wake that had not been fully demonstrated in previous time averaged flows. Watkins et al. found that while the far wake flow structures were dominated by the counter-rotating vortices described previously, the near wake region was also affected by these vortices, resulting in no reattachment occurring over the slant as had been expected previously. Instead of reattaching along the slant, the flow structure

in this separated region appeared to mix with the large separated region at the rear of the vehicle body. This vortex impingement on the flow structure at the rear of the Ahmed body would later prove to be of vital importance to the study conducted in this project.

2.2 Interaction of Multiple Vehicle Bodies

While an understanding of a single Ahmed body and its flow structures was essential to this study, the complexity that arises when two or more Ahmed bodies are in close proximity was equally important. Before moving on to the more complex Ahmed body, however, research on the interaction of simpler objects was first required.

To understand how two bodies interact aerodynamically with each other, Martinuzzi and Havell [13] conducted an experiment on two wall mounted cube structures. They showed that for two objects in tandem, the flow pattern depended greatly on the spacing between the two objects. The upstream obstacle always caused the flow to separate, and the effect of this separation on the downstream cube was heavily dependent on the spacing between them. When the spacing was $< 1.4H$ (H being the length of the cube), the wake structures from the upstream cube helped promote reattachment on the surface of the downstream cube. Between $1.4H$ and $3.5H$, there was a significant increase in turbulence in the gap between the two cubes, caused by the entrainment of the flow off the rear of the first cube. For larger spacings the flow appeared to reattach in the gap, upstream of the second cube (figure 6).

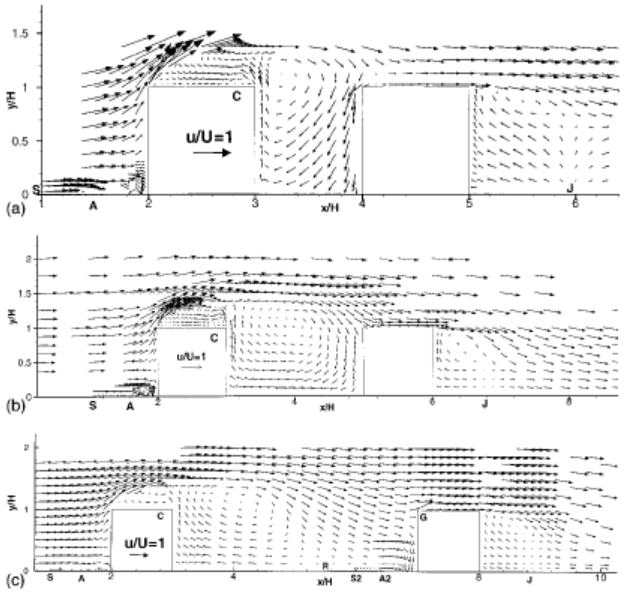

Figure 6: Vector representation of the mean velocity components at the symmetry plane. (a) S/H=1;(b) S/H=2; (c) S/H=4. [13]

While the interaction studied by Martinuzzi and Havell helped gain a large understanding of the interactions between two simple objects, the complexity of flow generated in the wake of the Ahmed Body created a need for a better understanding of their flow interactions. The purpose of the following studies was to highlight the potential benefits of multiple vehicle bodies traveling in convoy to reduce the overall drag of the system.

In a wind tunnel study conducted by Pagliarella et al. [14] to analyze the benefits and drawbacks of platooning (two or more vehicle bodies traveling in convoy in close proximity to each other) Pagliarella found that the Ahmed body behaved very differently from the simple cubes highlighted by Martinuzzi and Havell. The researchers found that when two Ahmed bodies were placed in convoy, the drag of the leading Ahmed body was usually reduced significantly, while that of the trailing body could

rise by up to 42% depending on the spacing between the two bodies. This dramatic, and surprising, change was the cause of much study into the interactions between multiple Ahmed bodies.

Vino [15] conducted wind tunnel experiments on the Ahmed Body at the RMIT wind tunnel to help gain an understanding into the aerodynamic interactions occurring between two Ahmed models in tandem. The aim of the thesis was to ascertain the aerodynamic advantages gained, if any, by traveling in convoy, a system proposed by the California Partners for Advanced Transit and Highways (PATH) as an attempt to increase the efficiency of passenger vehicles. Vino varied the spacing between the two Ahmed models in the wind tunnel in an attempt to understand how this gap affected the drag coefficients of the two bodies involved. Vino found that, surprisingly, the trailing model in the simulation had a larger drag coefficient than the leading model, or even a model in isolation, when the gap between the two was $< 1L$. The drag coefficient of the trailing model reached a peak value of drag 27 % higher than that of the isolated model in this range, prompting inquiries into the cause of this drastic change.

Conducting an analysis of the findings, Vino found that the trailing model wake did not appear to demonstrate a significant change in the wake structure from that of the model in isolation, implying that the cause for the unexpected increase in drag occurred at the front of the body. Varying the spacing between the two bodies demonstrated the causes for these effects. In the region of increased drag for the trailing body, the lead model was allowed to develop streamwise trailing vortices, as expected, along with a separation bubble. This resulted in the generation of a low

pressure, high-momentum flow at the rear of the lead body, which when interacting directly with the front end of the trailing model, resulted in an increase in drag for the trailing body. This flow was in keeping with the findings of Watkins et al. [12] who demonstrated that the flow at the rear of the Ahmed model does not necessarily reattach in the near wake, but instead interacts with the separated region at the rear of the Ahmed body resulting in wake impingement, developing this region of high momentum flow in the streamwise direction.

The exact causes and effects of this were of great interest and in order to increase understanding Pagliarella [2] also conducted wind tunnel experiments on multiple Ahmed bodies in a convoy arrangement. In his study, Pagliarella analyzed Ahmed models of two different rear slant angle configurations (25^o and 35^o) in various combinations of leading and trailing body to document the effects of the wake impingement on the drag of the two bodies. Pagliarella first conducted experiments on the bodies in isolation to ascertain that the values being generated were sound, while also developing a baseline of results against which the platooning experiments could be compared. Subsequently, two models were placed in the wind tunnel and their separation was varied to ascertain the effects this spacing had on the aerodynamic coefficients of the bodies. The maximum spacing studied was $2L$, with a variety of spacing tested between $0.125L$ and $2L$.

From the experiment Pagliarella came to a series of interesting conclusions. Pagliarella found that in a platooning situation, one in which the trail body was behind and perfectly in line with the lead body, the drag coefficient of the lead body was always decreased. This was as expected, and in keeping with the findings of Martinuzzi et

al. [13] as well as Vino [15]. For the trailing model however, the drag was always increased when compared to the model in isolation. This agreed with Vino's findings, but raised some interesting questions as to the cause for these effects. Pagliarella also found that the net drag for the entire system was always reduced in the platooning situation, i.e. the decrease in drag for the leading body was always of greater magnitude than the increase in drag for the trailing body.

Paglarella found that the maximum drag increase in the trailing model was 38% from that of the model in isolation, a very significant amount. This position of maximum drag for the trailing model corresponded to the position of minimum drag for the leading model, again resulting in a net loss of drag for the system. Pagliarella found that one possible reason for this increase in drag for the trailing model was due to the raising of the stagnation point at the front of the model from that of an isolated model. This change in position of stagnation point could be directly attributed to the wake impingement off the rear of the lead model, especially at close spacings.

For the leading model, it was found that there were several underlying causes that led to the decrease in drag coefficient observed. The vortices off the rear of the vehicle body were weakened by the presence of the trailing model, which inhibited the full development of these vortices. In addition the trailing model also impeded the low velocity flows from the rear of the lead model, resulting in an increase in pressure in the gap between the two bodies. These changes in the wake of the lead body caused a large change in flow at the front of the trailing body from a body in freestream conditions. The vortices impinging on the front of the trailing body resulted in a significant increase in pressure at the front of the trailing body, while having a

negligible effect on its wake. It was this increase in forebody drag that caused the increase in drag for the trailing body in all the configurations tested by Pagliarella. A plot of the drag trends with spacing, as well as the various configurations tested, can be seen below as figure 7.

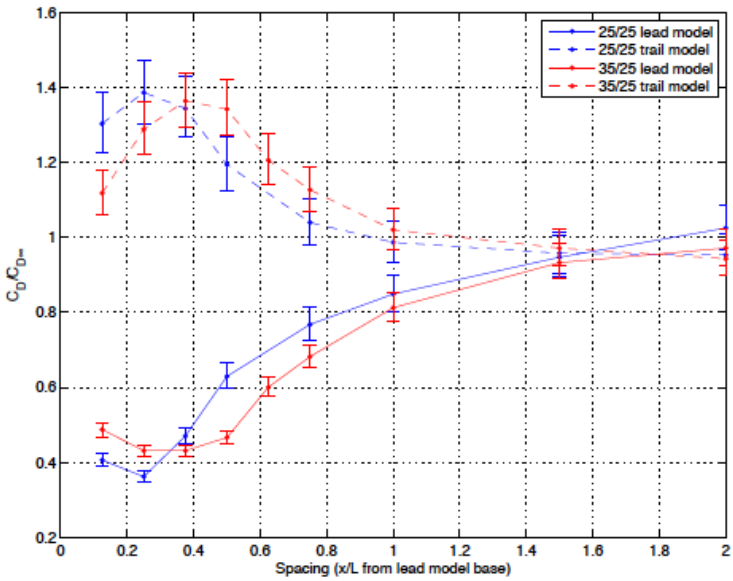

Figure 7: Normalized C_D for lead and trail model in platooning formation at various spacing. [2]

In addition to the wind tunnel experiments conducted by Vino [15] and Pagliarella [2], Rajamani [16] conducted CFD investigations into the effects of vehicle platooning using Ahmed bodies of various slant angles and at a range of separation distances. Rajamani's study utilized the FLUENT CFD solver and was conducted using the Realizable $k-\epsilon$ turbulence model. Along with the CFD simulations, Rajamani conducted experiments in the wind tunnel to provide an additional source of data for his study, while also comparing against the data gathered by both Vino and Pagliarella.

In addition to analyzing the effect that vehicle spacing had on the system, Rajamani also investigated the effect of changing the rear slant angle of the Ahmed bodies used during the simulation.

Rajamani found that his CFD simulations were extremely close to the experimental results gathered by Pagliarella for the case of two Ahmed bodies in tandem when the separation was small. At larger separations ($> 2L$), however, Rajamani found that while using CFD the effects of the lead body on the trailing body still being demonstrated, which was in contrast to the results of Pagliarella, which stated that at separations of $2L$ the trailing body had reverted to behaving as a model in isolation. The results of Rajamani's simulation can be seen below as figure 8, which when compared to Pagliarella's results (Figure 7) highlight both the similarities and differences between the two results.

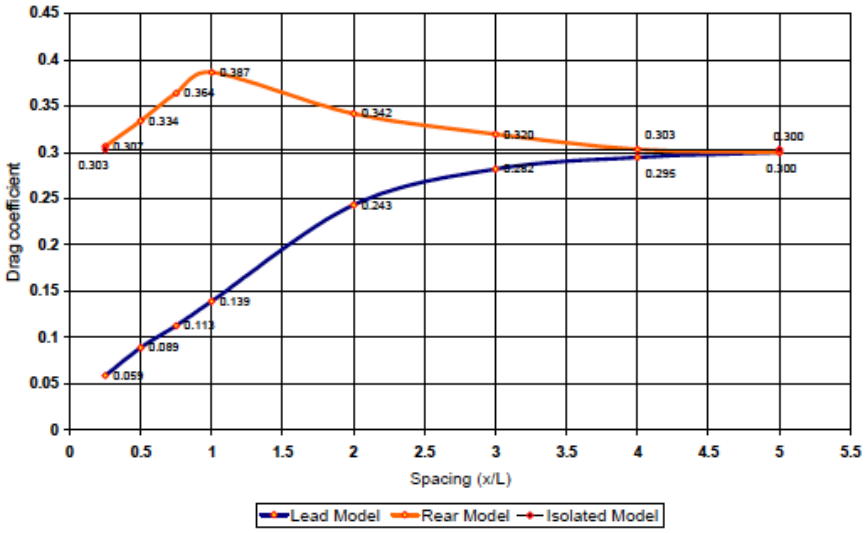

Figure 8: C_D for lead and trail model in platooning formation at various spacing from CFD. [16]

Once again, Rajamani found that at close vehicle spacings, the impingement of the

flow from the rear of the leading body on the front of the trailing body resulted in an increase in drag force of the trailing body, while the subsequent suppression of the low pressure region at the rear of the lead body caused a decrease in the drag of the lead body. These changes were highlighted in the velocity and pressure scenes generated by Rajamani at various spacings, which can be seen below as figures 9 to 11.

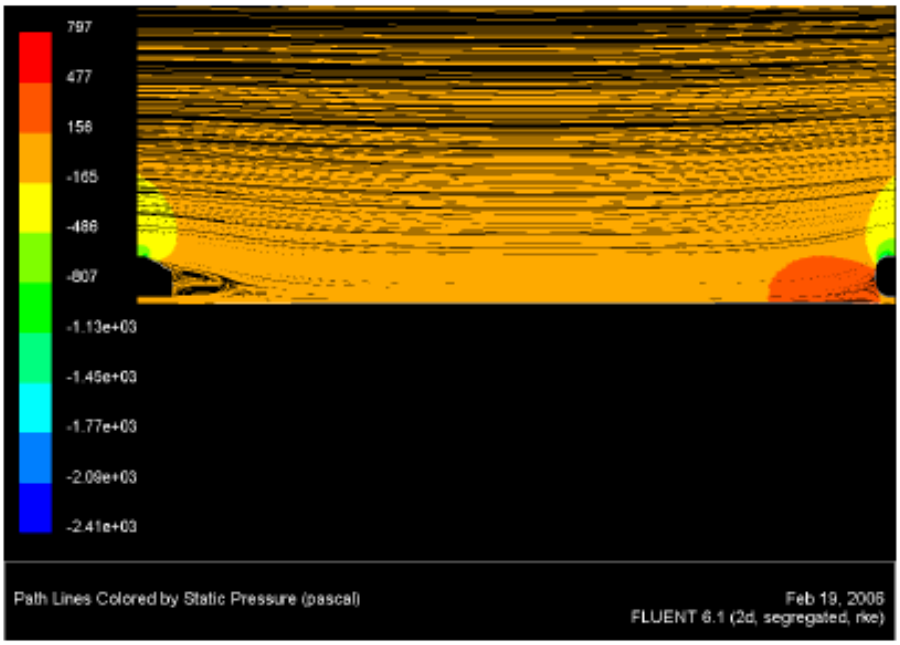

Figure 9: Pressure path lines at $x/L = 5$. [16]

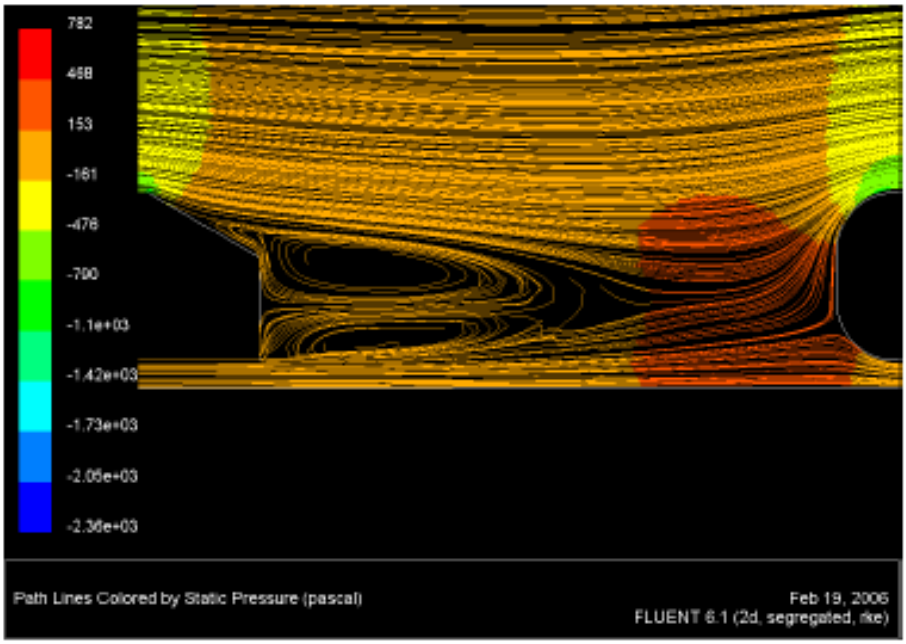

Figure 10: Pressure path lines at $x/L = 1$. [16]

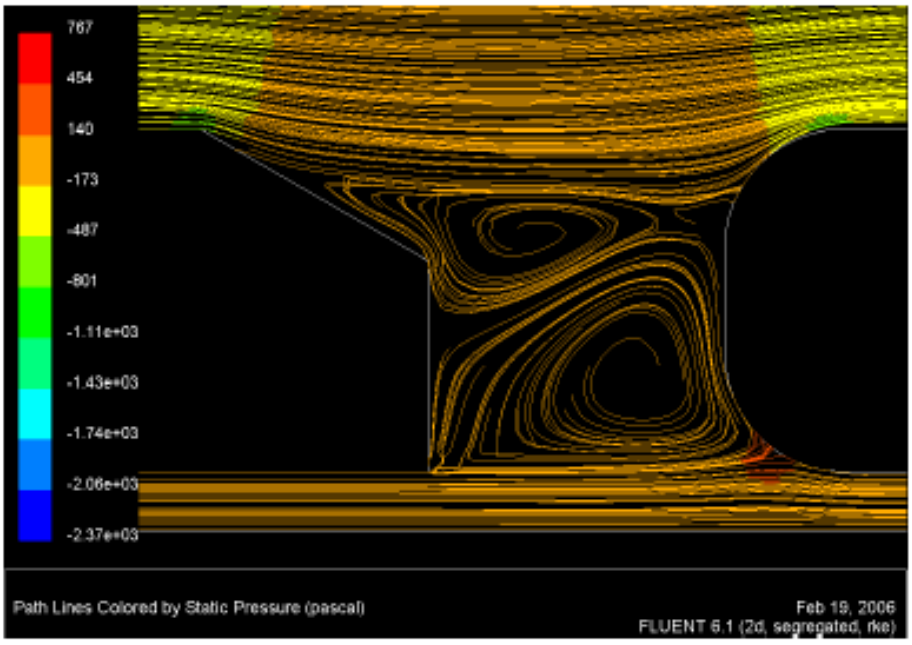

Figure 11: Pressure path lines at $x/L = 0.25$. [16]

From the images presented above, the interaction between the wake of the lead Ahmed body and the front of the trailing Ahmed body became clear. At large sepa-

rations the wake of the leading body was allowed to develop fully, and subsequently revert to being effectively a free-stream flow, allowing the bodies to behave as two isolated bodies at a separation of $5L$. At $1L$ separation however, the flow was not allowed to redevelop entirely, resulting in the significant changes in drag observed above. At the very close spacing of $0.25L$, the wake of the lead body was suppressed considerably, resulting in a region of significantly higher pressure in the gap between the two bodies, thereby increasing the drag at the front of the trailing body, while reducing the drag at the rear of the lead body.

Rajamani's study provided evidence of the causes for the effects described previously by both Vino and Pagliarella, while also demonstrating the effectiveness of CFD to highlight the causes for these effects.

In another CFD study of the effects of platooning, Watts [17] conducted simulations using both the Ahmed body, as well as more complicated truck shapes to analyze the effects of multiple bodies behaving in tandem. Watts conducted his simulations using both DES and URANS simulations. Once again, Watts found that the trailing Ahmed body saw an increase in drag coefficient when compared to an isolated model. Watts' study highlighted the cause for these changes by demonstrating that for the lead body, the main source of drag was the wake structures at the rear of the body, as was expected when comparing to the previous studies conducted on the Ahmed body [6]. For the trailing body, however, the largest source of drag was found to be at the front of the vehicle. These results can be seen below as figures 12 and 13.

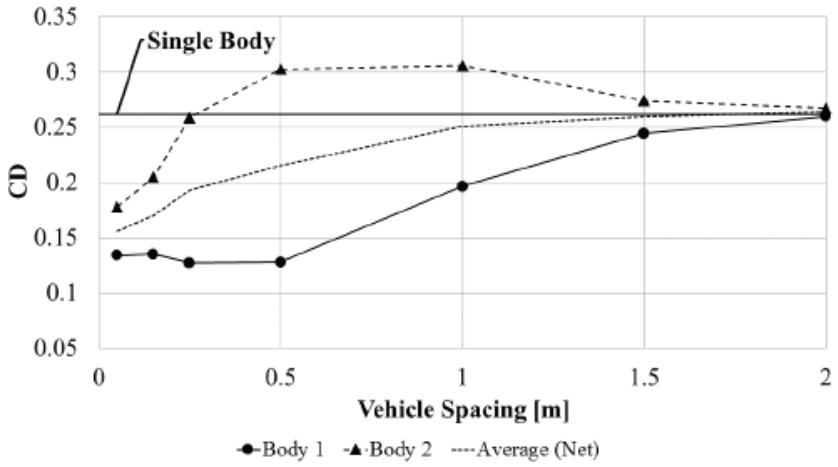

Figure 12: C_D of the two Ahmed bodies in platoon using CFD. [17]

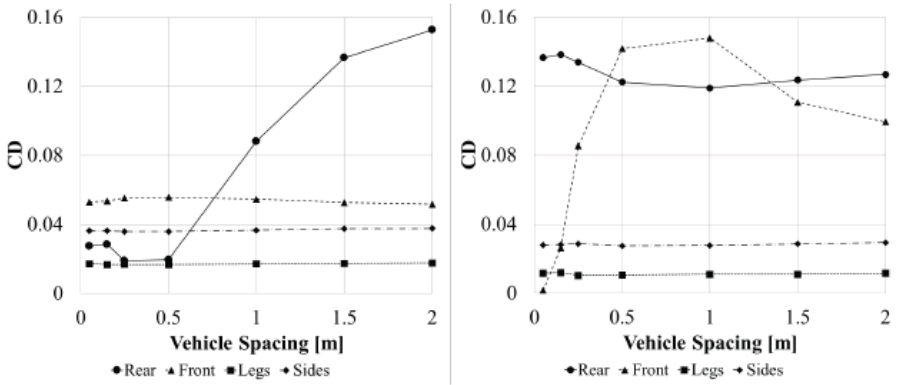

Figure 13: C_D of the two Ahmed bodies in platoon broken down by region of the body using CFD (a) Lead body. (b) Trailing body. [17]

Watts' results highlighted the difference in source of drag for the two bodies in the simulation. As had been demonstrated by Ahmed et al. [6], the major source of drag in the Ahmed body was the rear of the vehicle body, as evidenced by the drag breakdown of the lead body. At close separation, this drag effect was reduced significantly, directly causing the dramatic decrease in drag described for the lead body. For the trailing body, however, the front of the vehicle showed a significant

increase in contribution to overall vehicle drag, while the rear of the trailing body did not undergo any significant changes. As a result the drag of this body increased dramatically.

In addition to confirming the results demonstrated by the experiments conducted by Vino [15] and Pagliarella [2], as well as the simulations conducted by Rajamani [16], Watts' study on the aerodynamic interaction between two tractor-trailers in platoon also provided a reason for the discrepancies between the experimental results and CFD simulations demonstrated by Rajamani. Watts conducted simulations using both the DES method, as well as URANS using the Realizable $k - \epsilon$ model for turbulence. In order to understand the effects of these different methods Watts carried out simulations wherein the two truck bodies were at a very large separation of 1000ft. the velocity profiles generated by the two methods can be seen below as figure 14.

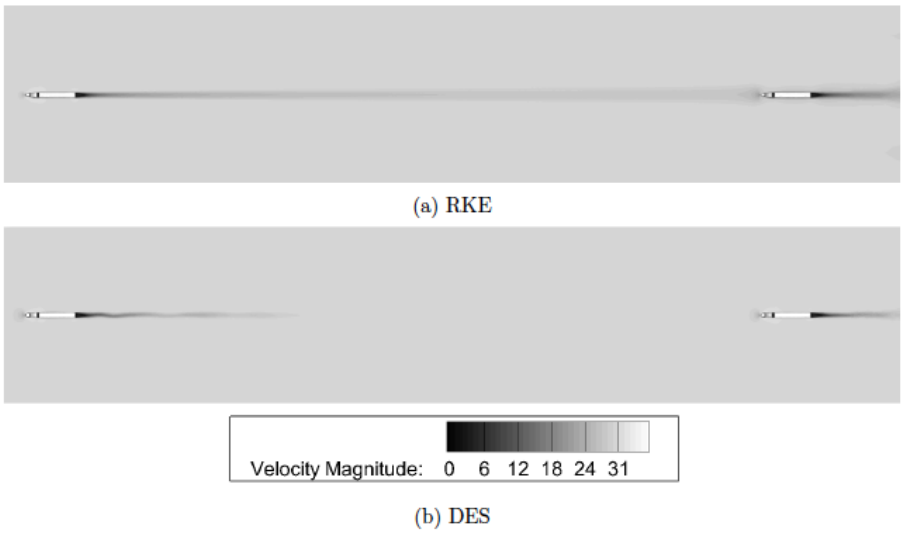

Figure 14: Velocity profile of two trucks at a separation of 1000 ft using (a) Realizable $k - \epsilon$ and (b) DES . [17]

From the figure it became immediately clear that the Realizable $k - \epsilon$ model never

fully terminated the wake from the leading body, while DES did so successfully. As a result the DES simulation demonstrated that at this extremely large separation, there was no effect from the wake of the leading body on the trailing body, which was as expected. For the Realizable $k-\epsilon$ simulation, however, this wake propagated for a seemingly infinite distance behind the lead body, never becoming "Re-laminarized" [17]. These differences were further highlighted when analyzing the turbulent kinetic energy in the wake of the leading model, using both methods as shown below in figure 15. Once again it became clear that the DES simulation successfully resolved the flow behind the leading model, while the Realizable $k-\epsilon$ model was unable to do so.

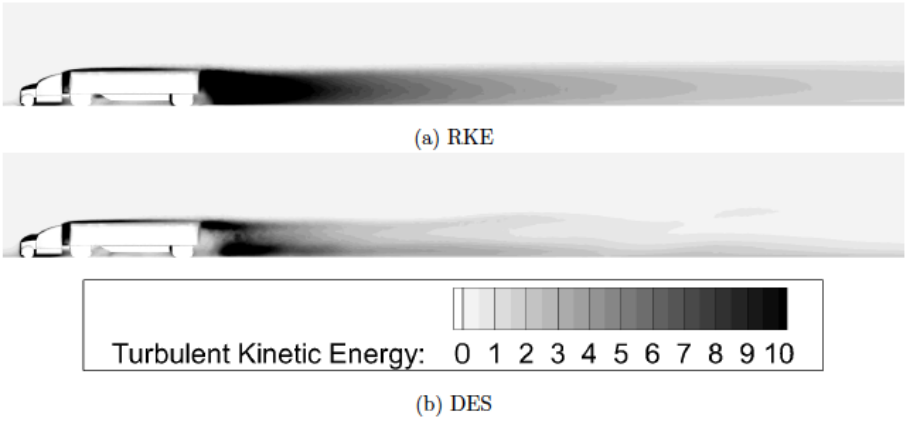

Figure 15: Turbulent Kinetic Energy of two trucks at a separation of 1000 ft using (a) Realizable $k-\epsilon$ and (b) DES . [17]

These discrepancies at large separation did not invalidate the results of the realizable $k-\epsilon$ simulation though, because as demonstrated the values at close spacing were extremely close to those from both the experiment as well as the DES simulation.

2.3 The Overtaking Maneuver

The studies of Ahmed bodies in convoy provided an extremely valuable source of information for the simulation conducted. However, when an actual overtaking maneuver is performed the flow interactions between the two bodies become even more complicated and interesting. Studies concerning an overtaking maneuver have proven to be extremely inconvenient in the wind tunnel due to the difficulty of keeping a body moving, while still being able to take accurate measurements of the aerodynamic coefficients acting on the bodies. Meanwhile, the computational power required to model the maneuver using CFD has also proved to be a point of difficulty. Regardless, the following studies attempted to model the maneuver using both wind tunnels and CFD, and have provided a strong database of information from which a new study on the overtaking maneuver could springboard.

In their 2004 paper Noger et al. [1] claimed that passenger vehicles are now more sensitive to passing maneuvers due to the increase in aerodynamic deign considerations undertaken when developing vehicles today. However, the ability to properly test the effects under the conditions of a passing maneuver was a difficult concept, especially on full-scale car bodies. Instead, most tests conducted used scale models and instead of being conducted on a moving body, were simply conducted by testing the effects two or more scale models had on each other at various discrete locations in relation to each other. However, Yamamoto et al. [18] showed that even small values of relative velocity (V_r) could result in significant differences in the aerodynamic forces acting on the two vehicles. To fully understand this Noger et al. used a wind

tunnel with an experimental bench as shown below in figure 16.

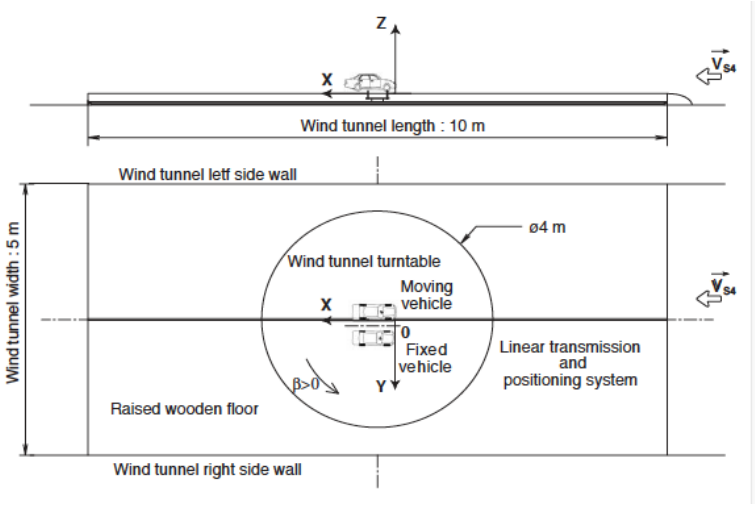

Figure 16: Test set up used by Noger et al. [1]

The test system pictured in figure 16 spanned the wind tunnel used by Noger et al. and allowed for varying various factors in the experiment, including the longitudinal spacing (X/L), transverse spacing (Y/W), yaw angle (β), wind tunnel velocity (V_o), as well as the relative velocity (V_r). The moving body could be moved longitudinally at speeds ranging from 0-10 m/s, with extremely quick acceleration and deceleration rates ($40\ m/s^2$). In addition to this the authors developed a dimensionless coefficient, k, which is defined as follows:

$$k = \frac{V_r}{V_o} \tag{1}$$

Noger et al. demonstrated that the aerodynamic effects of the two bodies could be broadly characterized based on the distance between the two bodies, as well as the relative velocities between the two. As the transverse spacing between the two bodies was decreased, the aerodynamic interaction between the two bodies increased

significantly, as evidenced by the changes in the C_s and yawing moment values in figure 17. It was interesting to note that the location of the peaks of these forces was not affected by altering the transverse spacing, only their magnitude. As the two vehicles cross each other, the peaks appeared to change signs. The effect of varying relative velocity had a very small effect on side force and yawing moment for the overtaken vehicle body, as can be seen in figure 18.

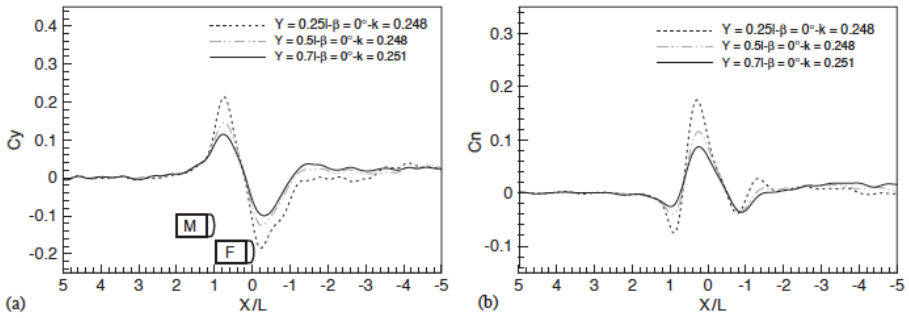

Figure 17: Demonstrating the effects of varying transverse spacing between the two bodies on (a) Coefficient of Side Force on the Overtaken body. (b) Coeffecient of Yawing moment on the Overtaken body [1]

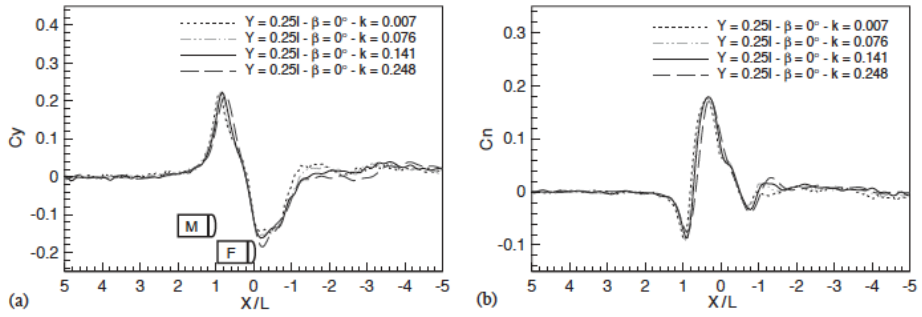

Figure 18: Demonstrating the effect of varying relative velocity V_r (a) Coefficient of Side Force on the Overtaken body. (b) Coeffecient of Yawing moment on the Overtaken body [1]

The authors also tested the effects of varying transverse spacing and relative velocity on the drag coefficient of the overtaken vehicle. As can be seen in the plot in figure

19, the C_D of the overtaken vehicle appeared to reach a minimum when the high-pressure area at the front of the overtaking vehicle was positioned directly behind the overtaken vehicle. After this point the C_D value of the overtaken vehicle began to rise rapidly until the bodies were almost side by side, where it falls very quickly to zero. The drag values of the overtaken vehicle then began to drop rapidly, reaching a minimum when the low-pressure region at the tail of the overtaking vehicle was in line with the nose of the overtaken vehicle. Beyond this point the C_D value of the overtaken began to rise again, however it was found that even when the overtaking vehicle was far ahead of overtaken vehicle, the overtaken vehicle was still affected by the wake of the overtaking vehicle and never fully recovered the drag coefficient of a single vehicle body.

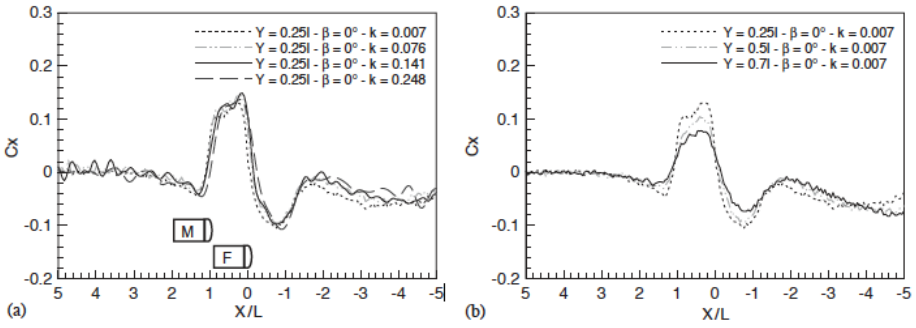

Figure 19: (a) Effect of varying relative velocity V_r on C_D of overtaken body. (b) Effect of varying transverse spacing on C_D of overtaken body [1]

Noger also conducted another study on the overtaking phenomenon, using the same test set up described before. This time however, the experimental data was used to compare against data generated using CFD. Gillerion and Noger [3] used a quasi-steady simulation, which involved measuring the aerodynamic coefficients of drag, side force, and yaw on two vehicle bodies at several discrete locations relative to each

other. They did so using the $k - \omega$ turbulence model and two Ahmed bodies in close proximity to each other. Since the simulation was unable to accurately model for the transient nature of the overtaking process, the experimental test bench from Nogers previous study was once again used to understand the deficiencies in their CFD simulation.

The experiment was run at the same conditions as the CFD simulation, a free stream velocity V_o of 30 m/s and V_r of 10 m/s. The plots of the simulation data were then compared to those from the experiment, and it became clear that while a quasi-steady simulation could accurately predict the trends of side force coefficient and yawing moment, it could not fully account for the transient effects demonstrated by the experimental set up. This was made clear by the difference in values between the plots generated by the experiment and simulation (figure 20).

In addition to calculating the aerodynamic coefficients present during the overtaking process, Gillerion and Noger also found that these coefficients undergo a pseudo-harmonic vibration, and provided values for the Strouhal numbers associated for these. Using the experimental test bench set up the researchers found that for the overtaking case the Strouhal number was 0.2, a value which would become important later on in the simulation.

Gillieron and Noger were not the only ones to attempt to model the overtaking maneuver using CFD. Corin et al. [4] conducted a simulation using the 2D PARAD model (Figure 21) and a sliding grid. To that point, most simulations had used the quasi-steady approach discussed above, which failed to capture fully the transient factors affecting the simulation. To help better understand these factors Corin et

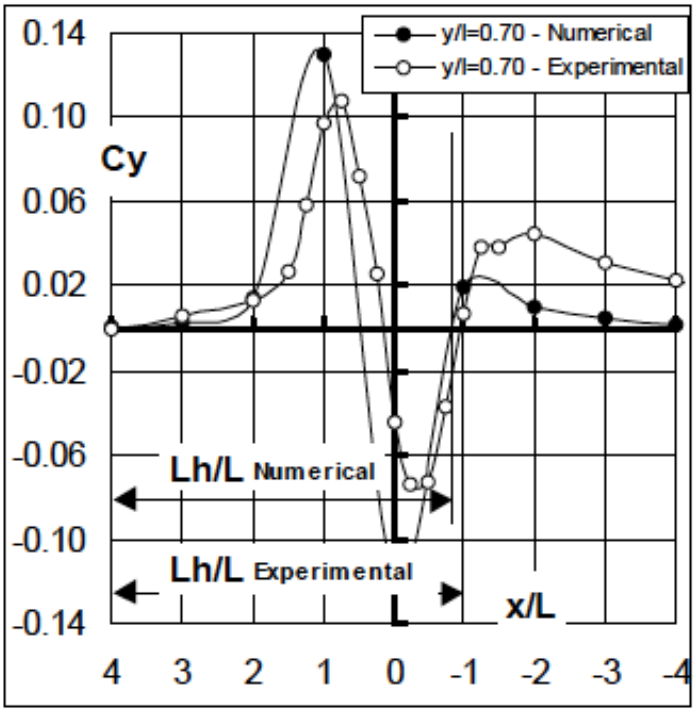

Figure 20: Plot of side force for the overtaken vehicle demonstrating the difference between the experimental and numerical results [3]

al. ran the simulation in 2D using an unsteady solver in addition to the sliding grids shown below in figure 22. The simulation was run in 2D due to limited computational resources.

The results from the qausi steady and unsteady analyses would be compared based on the values of C_D, C_s, C_p, and C_{ym} (Yawing moment coefficient). The unsteady simulation used a four-step Runge-Kutta time marching scheme, with a multi grid scheme. The computational domain was set to be 2L either side of the vehicles, and 6L long. This relatively small domain was due to limited computational resources, a factor which also dictated the total number of cells be limited to 5×10^4, while further limiting the number of surface cells to 250 per body.

The outer boundaries of the system had prescribed stagnation pressure, temper-

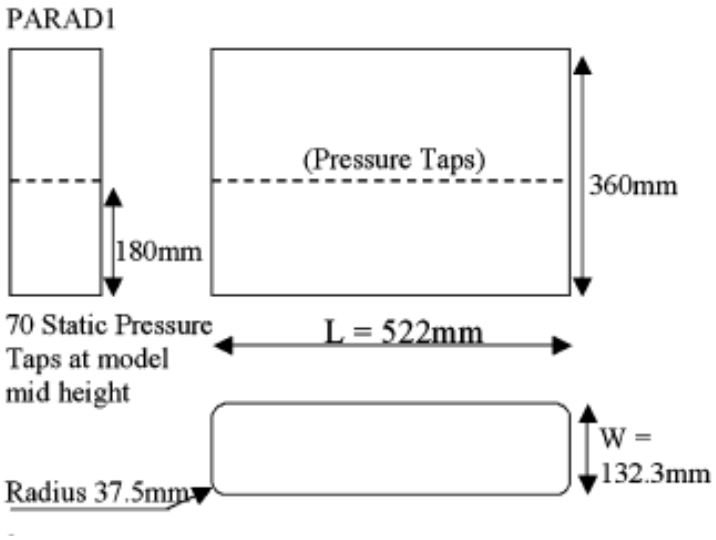

Figure 21: Dimensions of the PARAD vehicle model used by Corin et al.[4]

ature, and flow velocity. At the interface between the two blocks, the boundary condition was determined using linear interpolation between the two blocks. For the blocks undergoing relative motion, a second order interpolation and correction method was used to transfer data directly across the interface. When the two blocks were no longer in line, which happened for the majority of the simulation, a periodic boundary condition was applied.

The limited number of surface cells on each body, caused by the limited computational resources, resulted in a mesh that was insufficient to properly resolve the boundary layer around the bodies. As a result, the surface shear stress was determined using the log law, while a slip wall determined velocity. The single equation Spalart-Allmaras model was used in the simulation, and it was allowed to run at steady state until a converged solution had been reached to ensure the aerodynamic coefficient values matched those of the experimental data. Once again it was found that they could not accurately predict flow separation due to the lack of a properly

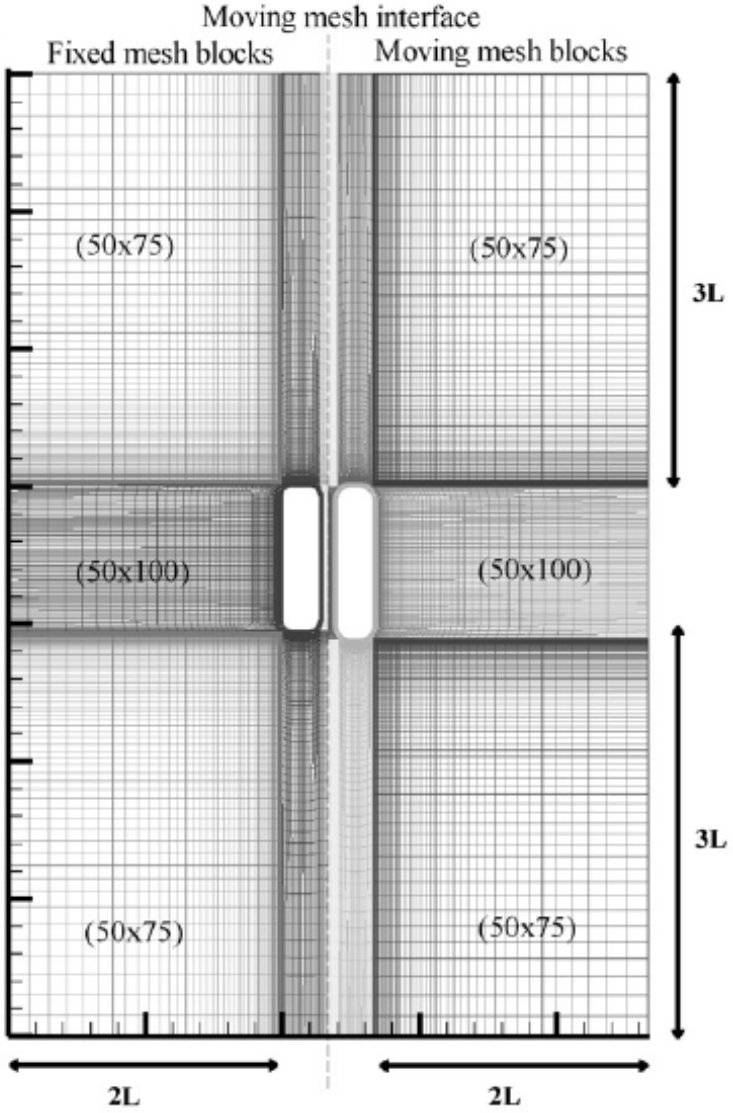

Figure 22: Sliding mesh set up used by Corin et al. for the 2D simulation on the PARAD model. [4]

defined boundary layer.

The simulation was run in both the quasi steady state and using the sliding mesh. In the unsteady case there was difficulty in modeling the yawing moment for the overtaking body due to its motion. In addition, the unsteady simulation was run at various values of transverse spacing as well as V_r, to properly understand the effect of these two factors on the aerodynamic forces acting on the bodies. The plots for

the simulation, comparing the values of C_D and C_s between the quasi-steady and unsteady simulations can be seen below in figure 23.

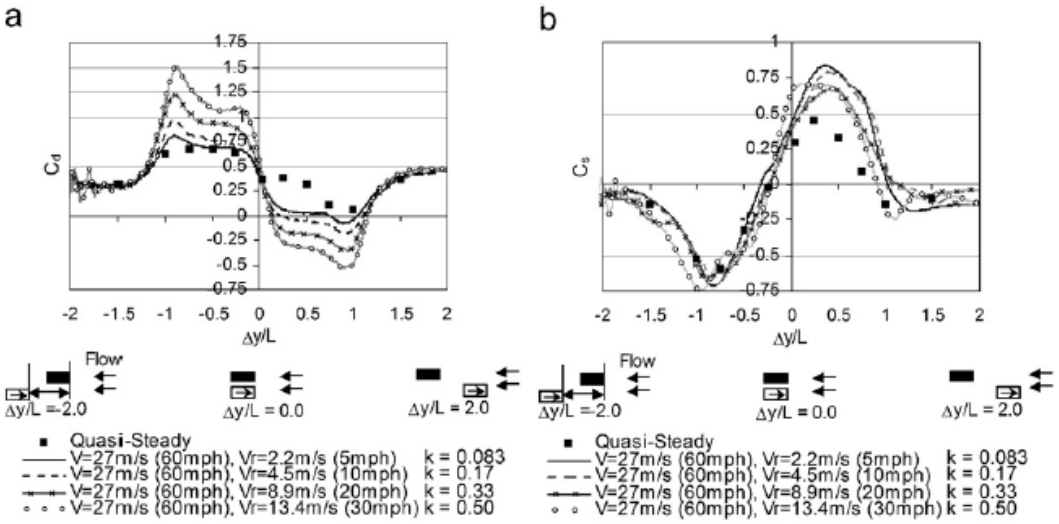

Figure 23: (a) Variation in C_D for the overtaken body at different values of V_r (b) Variation in C_s for the overtaken body at different values of V_r [4]

As can be seen there was a significant difference between the quasi-steady and the unsteady simulation. However, both simulations appeared to follow a similar trend, with the unsteady simulation describing on average far higher magnitude for the aerodynamic forces. This was due to the unsteady simulation taking into account the transient effects that the quasi-steady simulation was incapable of accounting for. It could also be seen that C_D changed quite significantly with changes in V_r, while C_s did not appear to be as affected by these changes. These results appear to be in agreement with those found by Noger et al. [1].

In addition to modeling C_D and C_s values, values of pressure coefficient were also plotted. Due to the additional relative velocity of the overtaking body, it appeared to consistently have a higher Cp value than the overtaken body.

At Chalmers University, Uystrepruys and Krajnovic [5] took the works of Noger

and Corin one step further by modeling the simulation in 3D, using a similar sliding-deforming mesh to measure the aerodynamic coefficients on the Ahmed body. For this simulation a 70% scale Ahmed model was used along with the $\zeta - f$ turbulence model. The computational domain used was significantly larger than any of those previously used, and thus allowed for better resolution..

Accuracy of the results was checked by running the simulation with various mesh conditions until a suitable mesh size was obtained. The simulation was then run at a range of V_r values for the overtaking body, and then compared to the experimental data (figure 24). Once it was confirmed that the experimental data and the simulation data were in agreement, the unsteady simulation was run at various velocity values. However, the researchers normalized all values with the velocity of the overtaken vehicle, which caused a decrease in the peak value of the aerodynamic coefficients as velocity was increased.

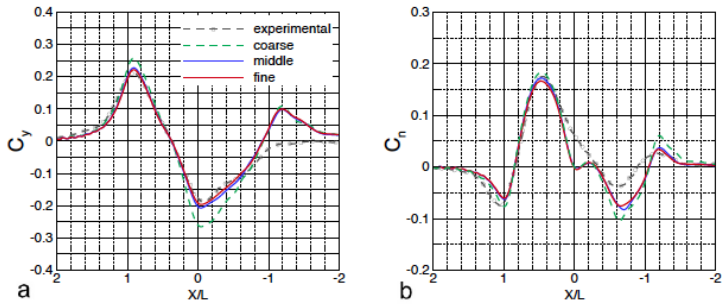

Figure 24: (a) Coefficient of Side Force on the overtaken body at various mesh resolutions. (b) Coefficient of Yawing Moment on the overtaken body at various mesh resolutions. [5]

Similarly, the simulation was run at different values of transverse spacing which showed that as the spacing between the vehicle bodies is increased, the effects on the aerodynamic coefficients are decreased as can be seen in figure 25

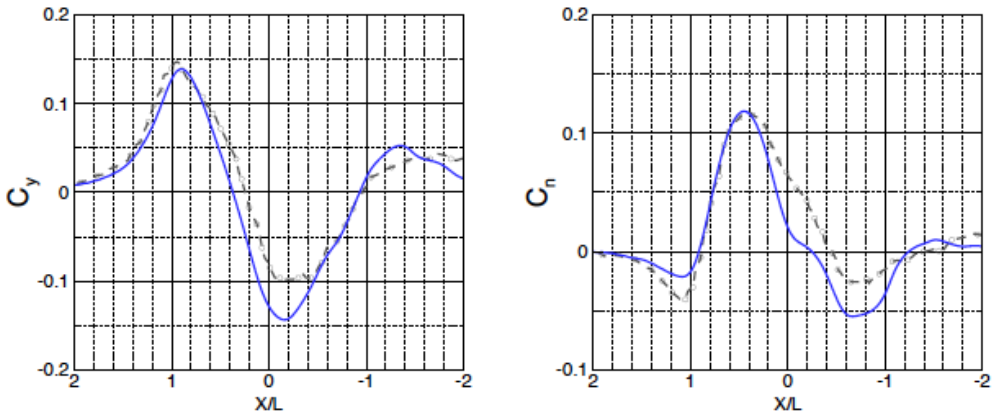

(a) $Y = 0.5W$

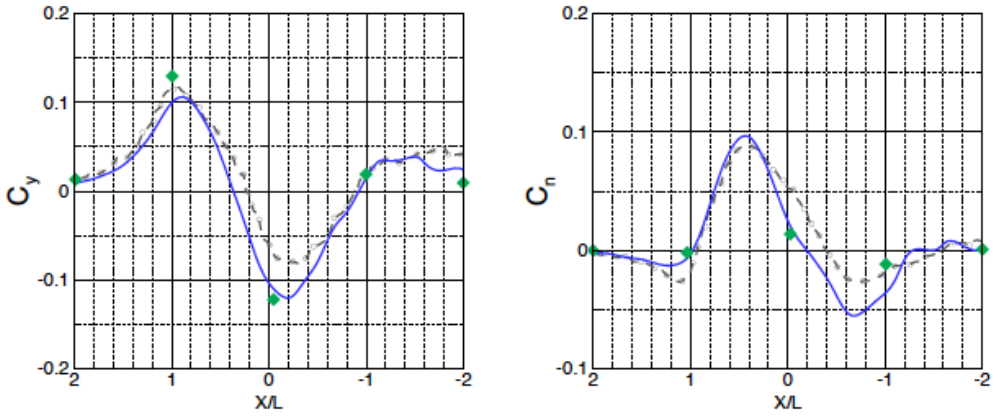

(b) $Y = 0.7W$

Transverse spacing effects on the overtaken body. Side force (left) and yawing moment (right) coefficients. (⊖) experimental, (—) numerical. For $Y = 0.7$, (◆) quasi-steady numerical results of Gilliéron and Noger

Figure 25: Plot and description from [5] showing the effect of Transverse spacing on the coefficients of side force and yawing moment of the overtaken body

Once these values had been gathered, points of interest along the overtaking maneuver were analyzed in greater detail. It was found that as the high-pressure region at the front of the overtaking vehicle approached the rear of the overtaken vehicle, it caused a significant increase in the drag coefficient of the overtaken vehicle. At this point the side force of the overtaken vehicle also increased dramatically as a result

of the difference in the pressures between the regions. As the overtaking vehicle continues past the overtaken vehicle, the side force coefficient began to decrease as the low-pressure region on the side of the overtaking body caused the overtaken body to pulled towards it. The drag coefficient continued to increase, and then dropped dramatically as the vehicles drew side by side. The side force also decreased dramatically and became negative on the overtaken vehicle. Once the bodies had crossed the effect was reversed, the low-pressure region at the rear of the overtaking vehicle caused a significant drop in the drag coefficient of the overtaken vehicle. Once the overtaking body was significantly ahead of the overtaken body, the values of the coefficients began to return to their original values.

The simulations showed that a 3D model of an overtaking maneuver was possible, and could yield quite significant results. It showed that as the transverse spacing between the bodies increases, the aerodynamic coefficients decrease significantly. A similar trend was noted with a change in velocity.

The experimental study conducted by Noger [1] was pivotal in all subsequent studies conducted on an an overtaking maneuver, and remains the largest source of information for any future studies in this field. Noger et al. provided experimental data against which the capability of all future simulations and experiments could be compared, while highlighting some of the transient effects that had so far not been fully understood. The study also demonstrated the drawbacks in the quasi-steady modeling of the overtaking maneuver and highlighted a need for an efficient method to simulate a passing maneuver in the transient state. While this was attempted using the sliding mesh set up, the computational demands of this method made it difficult

to implement effectively. Still, the results from the sliding mesh simulation gave a clearer indication of the interactions between the flow fields during a passing maneuver, and strongly contributed to its analysis. A clear understanding of the expected trends in aerodynamic coefficients during this process, and a solid experimental base to compare against, allowed for the development and verification of the overset mesh method used in this simulation.

CHAPTER 3: SIMULATION DETAILS

Armed with a strong understanding of the aerodynamic characteristics of the Ahmed body, both as an isolated body as well as with multiple Ahmed bodies interacting, research into the new method for conducting an overtaking simulation could begin. The overset mesh was known to be able to model complex motions in a CFD simulation, and therefore research was undertaken into the methods of its implementation. In addition, the selection of the physics model to be utilized in the simulation was of paramount importance. This chapter contains details regarding the capabilities and implementation of the overset mesh, as well as an overview of the physics model selected for the simulation, followed by an insight into the set-up of the simulation itself.

3.1 Mesh and Physics selection

Due to the inabilities of the quasi-steady and sliding grid approach being able to fully define the flow around the vehicles in the overtaking maneuver, an alternative method was sought. The overset-grid technique on complex body geometries was first used in 1988 for the Integrated Space Shuttle Launch Vehicle (SSLV). This grid contained less than a million cells, but still required over 12 months to generate due to the severe lack of computational power as well as the lack of purpose-built tools to generate Overset grids on complicated body geometries. In the years following how-

ever, overset grid generation took large strides forwards. Several software packages were developed that could easily generate overset grids with minimal user defined input. [20]

The Overset, or Chimera method allowed for the generation of independent meshes for the various components present in the computational domain, and to then connect these various domains to obtain a single universal solution [21].The method offered several advantages:

- Simplified mesh generation since the various components present could each be given a separate mesh with parameters most suited to the flow effects around that component
- Greater local refinement in areas where more accuracy was required.
- Simulations with moving components were made much easier because the independent meshes were moved as rigid bodies and the solution was automatically re-integrated into the overall solution when required (i.e. at each time step). This allowed for simulations to preserve boundary layers and local refinement around the moving bodies more easily, while maintaining reasonable computational size.

The main advantage of the Chimera mesh with regard to moving bodies came in its ability to treat a mesh region as a rigid body and update it from one time step to the next while still maintaining a good solution. The coupling of regions only affected the cells in the vicinity of the interface, and could be considered negligible provided

the interface was kept a reasonable distance away from the bodies in question, or the interface was defined as being in close proximity to the bodies. StarCCM+ is able to generate overset grids relatively easily, provided a good geometry and well defined regions. When generating overset grids in StarCCM+ a few factors were taken into consideration [22]:

- Cells in the overset region and the background region had to be of comparable size in the overlap zone to ensure a reasonable solution.
- Motion had to be limited to 1 cell per time-step for the overlap zone.

Most overset grid generation tools follow 4 basic steps:

1. Geometry processing
2. Surface-grid generation
3. Volume-grid generation
4. Domain connectivity.

Most major bottlenecks in the overset grid generation process occurred in the geometry processing phase, where difficulties arose with complex body shapes and errors in the geometry such as missing body shapes and self intersecting faces. Once a proper geometry was defined the following steps could be undertaken relatively easily.

On a properly defined geometry the surface- and volume-mesh generations proved to be relatively straightforward. Once the meshes had been defined, the domain

connectivity step was of utmost importance. This step defined how the overset mesh interacted with the outer background mesh, or in the case of multiple overset-grids how they interacted with each other. There were several factors that came into play when connecting multiple domains of an overset grid. Projection involved the shifting of surface grid points to prevent the effect of surface-discretization errors. Hole cutting allowed for the removal of grid points from one grid when they were placed inside the solid wall boundary of another grid. Fringe points are boundary points which are updated by the solver using interpolation, a factor which must be specified beforehand. With modern software packages, the majority of these issues were able to be resolved during the simulation.

Overset meshes have been used on increasingly complex geometries recently, with the ability to define an overset region as a rigid body and prescribe it a motion being one of the key factors in its use. Li et al.[23] demonstrated the efficacy of the overset mesh method by modeling a rotating turbine blade. The simulation used by Li et al. compared RANS and DES while using a series of overset meshes on a wind turbine (figure 26). These overset meshes allowed for the variation in factors such as the pitch, angle of attack, etc. with relative ease. The simulation showed that for both the RANS and DES simulations, the simulation matched well with the experimental results. The overset mesh method allowed for the refinement of the mesh in areas of interest, and a variation in the motion prescribed. The simulation demonstrated the ability of the overset mesh to model complex motions while still maintaining reasonable simulation size.

With the ability to generate the overset mesh to help complete the simulation, a

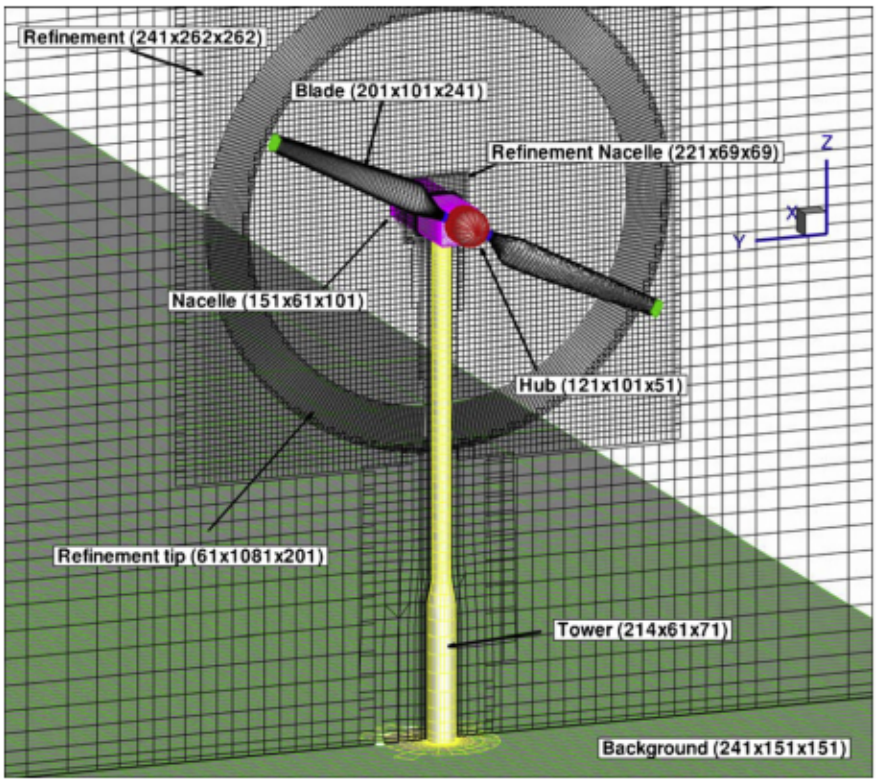

Figure 26: Overset mesh used by Li et al. on a wind turbine [23]

brief analysis of the various physics models available was undertaken. Iaccarino et al. [24] used studies of an unsteady flow around a wall mounted cube, for which the experimental data did not concur with the CFD results obtained using a steady state flow solver. This was due to the inability of the steady flow solver to accurately predict the the periodic shedding of vortices. To help combat this issue Iaccarino et al. ran unsteady RANS simulations over the wall mounted cube using the $v^2 - f$ turbulence model. The study showed that the unsteady simulation was far more accurate than the steady simulation in predicting the flow structures behind the cube, and was in far better agreement with the experimental data than the steady-state simulation.

Davis et al. [25] conducted a study of the effect of various physics models on a

wall mounted square cylinder. Using experimental results as a baseline, Davis et al. found that the Realizable $k-\epsilon$ physics model, with two-layer wall treatment provided the most accurate results of the models tested. The results from this physics model surpassed those of the $k-\epsilon$, v^2-f, and $k-\omega$ models, even in the viscous sublayer where it was expected to suffer.

Gorji et al. [26] conducted simulations of a flow in closed channel using various turbulence models and comparing these results to results obtained from DNS. The simulations were run in the unsteady state with the Reynolds number increasing from an initial value of 9308 to 29650, at various rates of acceleration. The studies found that the $k-\epsilon$ turbulence model could accurately predict values of wall shear stress that matched very closely with DNS values across the entire range of Reynolds numbers.

In order to understand the effects of physics model selection over a body, Eleni et al. [27] conducted simulations over a NACA 0012 airfoil using a range of turbulence models. The simulations were conducted in 2D and at various angles of attack for the wing, at a Reynolds number of $3x10^6$. The models tested were the single equation Spalart-Allmaras model, the realizable $k-\epsilon$ model, and the SST $k-\omega$ model. The results of the simulation were compared with experimental results to depict which turbulence model best captured the flow structures around the body. From the simulation it was found that in the mid range of angles of attack, the realizable $k-\epsilon$ and the SST $k-\omega$ models both matched the experimental data for C_D and C_L extremely well, but at higher values of angle of attack the $k-\omega$ model fared slightly better.

To better understand the physics of the simulation, or of any flow, the first step is

the Navier-Stokes equation [28]:

$$\frac{\partial \tilde{u_i}}{\partial t} + \tilde{u_j}\frac{\partial \tilde{u_i}}{\partial x_j} = -\frac{1}{\rho}\frac{\partial \tilde{p}}{\partial x_i} + \nu\frac{\partial^2 u}{\partial x_j \partial x_j} \tag{2}$$

The Navier-Stokes equation provides a description of the flow structure at all points in the fluid as a factor of its velocity, pressure, density, time, and location. While it is possible to describe the flow at all points in time and space using the Navier-Stokes equation, this is not a computationally feasible approach to modeling the turbulence structures in a simulation. Instead, the Reynolds Averaged Navier-Stokes equation is used:

$$\frac{\partial \tilde{u_i}}{\partial t} + \tilde{u_j}\frac{\partial \tilde{u_i}}{\partial x_j} = \frac{1}{\rho}\frac{\partial}{\partial x_j}\tilde{\sigma_{ij}} \tag{3}$$

$$\frac{\partial \tilde{u_i}}{\partial x_i} = 0 \tag{4}$$

In the equations above $\tilde{\sigma_{ij}}$ is the stress tensor and is defined by the equation:

$$\tilde{\sigma_{ij}} = -\tilde{p}\delta_{ij} + 2\mu\tilde{s_{ij}} \tag{5}$$

where $\tilde{p}$ is the hydrodynamic pressure, and δ_{ij} is the Kronecker delta, which is equal to 1 if $i = j$ and zero otherwise. μ is the dynamic viscosity of the fluid, and $\tilde{s_{ij}}$ is the rate of strain, defined by:

$$\tilde{s_{ij}} = \frac{1}{2}\left(\frac{\partial \tilde{u_i}}{\partial x_j} + \frac{\partial \tilde{u_j}}{\partial x_i}\right) \tag{6}$$

the velocity function described in the RANS equation $\tilde{u_i}$ can be broken down into two parts, the mean flow U_i and the fluctuating flow u_i using the equation:

$$\tilde{u_i} = U_i + u_i \tag{7}$$

$$\frac{\partial U_i}{\partial t} = 0 \tag{8}$$

If the equations are time averaged, the fluctuating velocity is negated and the RANS equations become:

$$\frac{\partial U_i}{\partial t} + U_j \frac{\partial U_i}{\partial x_j} = \frac{1}{\rho} \frac{\partial}{\partial x_j} \tilde{\sigma_{ij}} \tag{9}$$

$$\tilde{\sigma_{ij}} = 2\mu \tilde{s_{ij}} \tag{10}$$

$$\tilde{s_{ij}} = \frac{1}{2} \left(\frac{\partial U_i}{\partial x_j} + \frac{\partial U_j}{\partial x_i} \right) \tag{11}$$

While the RANS equation could be used to solve for all flows that were time independent, the nature of the simulation conducted here required that the fluctuating component of velocity was also included in the system. As a result equations 3-6 were used instead.

In order to analyze the flow, Star-CCM+ required the selection of a physics models to solve for some of the unknowns in the equations described above. In this simulation, the physics model chosen was the Realizable $k - \epsilon$ model. This is a two equation

model commonly used in CFD, and generates and solves the following equations for Turbulent Kinetic Energy (k) and the turbulent dissipation (ε):

$$\frac{d}{dt}\int_V \rho k\, dV + \int_A \rho k(\mathbf{v}-\mathbf{v_g})\cdot\, d\mathbf{a} = \int_A (\mu + \frac{\mu_t}{\sigma_k}) \bigtriangledown k\cdot \mathbf{a} + \int_V [f_c G_k + G_b - \rho((\varepsilon-\varepsilon_0) + \Upsilon_M) + S_k]\, dV \quad (12)$$

$$\frac{d}{dt}\int_V \rho\varepsilon\, dV + \int_A \rho\varepsilon(\mathbf{v}-\mathbf{v_g})\cdot\, d\mathbf{a} = \int_A (\mu + \frac{\mu_t}{\sigma_\varepsilon}) \bigtriangledown \varepsilon\cdot \mathbf{a} + \int_V [f_c C_{\varepsilon_1} S_\varepsilon + \frac{\varepsilon}{k}(C_{\varepsilon_1} C_{\varepsilon_3} G_b) - \frac{\varepsilon}{k+\sqrt{\nu\varepsilon}} C_{\varepsilon_2}\rho(\varepsilon-\varepsilon_0) + S_\varepsilon]\, dV \quad (13)$$

ε_0 is the ambient turbulence value in the source terms that counteracts turbulence decay

f_c is the curvature correction factor

G_k is the turbulent production term and is defined by the equations:

$$G_k = \mu_t S^2 - \frac{2}{3}\rho k \bigtriangledown\cdot \mathbf{v} - \frac{2}{3}\mu_t(\bigtriangledown\cdot \mathbf{v})^2 \quad (14)$$

in the equation $\bigtriangledown\cdot \mathbf{v}$ is the velocity divergence and $\mathbf{S}$ is the modulus of the mean strain rate tensor

$$S = \mid \mathbf{S} \mid = \sqrt{2\mathbf{S}:\mathbf{S}} \quad (15)$$

$$\mathbf{S} = \frac{1}{2}(\bigtriangledown \cdot \mathbf{v} + \bigtriangledown \cdot \mathbf{v}^T) \tag{16}$$

G_b is the production due to buoyancy and is defined by the equation:

$$G_b = \beta \frac{\mu_t}{\sigma_t}(\bigtriangledown T \cdot \mathbf{g}) \tag{17}$$

where β is the coefficient of thermal expansion, $\mathbf{g}$ is the gravitational vector, $\bigtriangledown T$ is the temperature gradient vector, and σ_t is the turbulent Prandtl number.

Υ_M is the dilation dissipation, defined by the equations

$$\Upsilon_M = \frac{C_M k \varepsilon}{c^2} \tag{18}$$

where c is the speed of sound, and $C_M = 2$.

The turbulent viscosity μ_t in the realizable $k-\epsilon$ model is computed by the following equations:

$$\mu_t = \rho C_\mu \frac{k^2}{\varepsilon} \tag{19}$$

$$C_\mu = \frac{1}{A_0 + A_s U^{(*)} \frac{k}{\varepsilon}} \tag{20}$$

$$U^{(*)} = \sqrt{\mathbf{S} : \mathbf{S} + \mathbf{W} : \mathbf{W}} \tag{21}$$

$$\mathbf{S} = \frac{1}{2}(\bigtriangledown \cdot \mathbf{v} + \bigtriangledown \cdot \mathbf{v}^T) \tag{22}$$

$$\mathbf{W} = \frac{1}{2}(\bigtriangledown \cdot \mathbf{v} - \bigtriangledown \cdot \mathbf{v}^T) \tag{23}$$

$$A_s = \sqrt{6}\cos(\phi) \tag{24}$$

$$\phi = \frac{1}{3}\arccos(\sqrt{6}W) \tag{25}$$

$$W = \frac{S_{ij}S_{jk}S_{ki}}{\sqrt{S_{ij}S_{ij}}^3} \tag{26}$$

$$A_0 = 4.0 \tag{27}$$

The remaining model coefficients from the $k-\epsilon$ transport equations are defined as follows:

$$C_{\varepsilon 1} = \max\left(0.43, \frac{\eta}{5+\eta}\right) \tag{28}$$

$$\eta = \frac{Sk}{\varepsilon} \tag{29}$$

$$C_{\varepsilon 2} = 1.9 \tag{30}$$

$$\sigma_k = 1.0 \tag{31}$$

$$\sigma_\varepsilon = 1.2 \tag{32}$$

3.2 Simulation Set-up

Given the vast number of studies conducted on the Ahmed body, and the ease of availability from the data these studies provided, the Ahmed body was chosen as the test model for this simulation. An Ahmed body was constructed using SolidWorks according to the dimensions in the drawing shown earlier in figure 1. In addition to the Ahmed bodies, a hollow block of dimensions $27L \times 10L \times 10L$ was constructed to be the computational domain. The dimensions of the block were chosen to ensure fully developed flow in front of the two bodies, and proper resolution of the flow in the wakes of the two bodies.

Once the various parts had been constructed, they were all placed together in an assembly. The lead car (Overtaken body) was placed at a distance of $10L$ from the inlet, and the overtaking body was placed at a distance of $4.7L$ downstream from the lead body, keeping in mind the study conducted by Martinuzzi and Havell [13], and a distance of $0.5W$ to the side of the body.

This assembly was then imported into StarCCM+ for CFD analysis. The block was broken down into different sections. The Inlet section was defined as a velocity inlet, and given a velocity value of 40 m/s in the X direction. The Ahmed bodies, as well the ground, were all defined as no-slip walls, with the ground also being given a tangential velocity of 40 m/s to account for the under-body flow. The ceiling, near field, and far field of the block were all defined as slip walls, while the outlet was

made a pressure outlet. Once these initial designations had been set, analysis could begin.

The first step of the analysis was to conduct a mesh sensitivity study at steady state conditions. The overtaking body was temporarily removed from the simulation to allow for a quicker solution. The single car case was then run at varying mesh sizes until no significant change in the C_D value of the body was noted between studies. The results of these simulations can be seen in table 1 of the results. The inlet velocity chosen for this and all subsequent simulations was 40m/s, a value which corresponds to a Reynolds number (Re) of 2.6×10^6. This velocity had been used in a series of previous studies for the Ahmed body, and therefore the corresponding coefficients were well known. These cases were all run using the standard $k - \omega$ model at steady state.

The chosen mesh had a base size of 7.5 mm, which corresponded to 40 million cells in the single car case, and 45 million cells in the overtaking case. To ensure optimal use of computational resources a volume growth rate of 1.1 was applied, allowing the cells farther away from the bodies to be larger in size. Surface controls were added to the Ahmed bodies themselves to ensure proper capture of the boundary layer, while a volumetric control was created around the region of overtaking to ensure proper capture of the wake and interaction between the two bodies.

Once the C_D value of the single Ahmed body had appeared to reach a steady value regardless of mesh size, the chosen mesh was then used to decide the physics model for the study. The single car simulation was run in four separate cases, all as implicit unsteady simulations with a time-step of 0.001s. The physics models chosen were the

Standard $k-\omega$ model, SST Menter $k-\omega$, Standard $k-\epsilon$, and Realizable $k-\epsilon$. It was subsequently found that the Standard $k-\epsilon$ model could not adequately capture the flow conditions and did not attain convergence. The results of the three remaining models can be seen in the results section as figure 30.

The choice of physics model was based on the agreement of the C_D values from each model with results of the experiment conducted by Serre et al [7], a value of 0.298. It was found that the Realizable $k-\epsilon$ case came closest to this value in the unsteady simulation.

Once the physics models and mesh parameters had been selected, the overtaking body was brought back into the simulation. A block was placed around the overtaking body. The block was made so that it had dimensions $0.25L$ in front of and behind the body, $0.4W$ to either side of the body, and $0.5H$ above the body. The ground was placed to coincide with the ground of the tunnel. This block, along with the Ahmed body inside it would become the overset region for the simulation. The dimensions were chosen so as to ensure adequate cells surrounding the overtaking body on all sides between the overset region and the background region. The face of the block in contact with the ground was then separated from the rest of the faces. This was done so that a tangential velocity could be applied to this face which accounted for increased tangential velocity caused by the motion of the overtaking body. The remaining parts of the block were then assigned as an overset mesh, with the Ahmed body still defined as a no-slip wall. The entire Overset block as well as the overtaking body were then assigned to a separate region from the wind tunnel and overtaken Ahmed body. The overtaking Ahmed body was given the same mesh parameters as

the overtaken body to allow for a smooth solution.

Once the two regions had been constructed, an Overset mesh interface was created between them. Due to the close proximity in which the two cars would be passing, as well as the proximity of the bodies to the ground, the close proximity option was also selected to ensure a clear solution. Finally, a relative motion with a value of 2 m/s in the X direction was created, but not assigned to any region as yet.

With the set-up complete, the simulation was allowed to run with the implicit unsteady solver at a time step of 0.001s, an internal iteration count of 12, and a max time of 0.5s, with the chosen physics models, but no motion prescribed to either body as yet. This was to ensure that the simulations began from a fully converged solution without having to account for the motion. In addition to C_D monitor, monitors for C_s and C_L were set up on both bodies. Additional monitors were set up to measure the pitching, rolling, and yawing moment coefficients of the lead car. These moment coefficients were difficult to set up on the overtaking body due to its constant motion.

This baseline simulation was then allowed to run. Once convergence had been achieved, the solution history was cleared while keeping all the field results. This ensured that the converged solutions for the various coefficients measured remained at their final values, and the simulation could be run again with these values as initial conditions. The motion parameter defined earlier was then applied to the overset region. The number of inner iterations was increased to 16 to help ensure a converged solution in each time step, while still maintaining a reasonable computational time. The physical time was then set to 4 seconds to capture the full overtaking maneuver between the two cars.

In addition to the various aerodynamic coefficients being measured on the bodies, scalar scenes were created to properly understand the flow dynamics occurring in the simulation. In the XY plane, slices were created at 6 different values of Z to capture the interaction between the two bodies as they passed each other. Similarly, in the XZ plane, 11 slices were defined corresponding to 4 cutting through each body, while 3 slices were created in the gap between the two bodies to help fully analyze the flow.

The motion of the body in the X direction made it difficult to capture images of the moving body in the YZ plane, however 4 slices were created along the length of the stationary body, with an additional slice being placed in the wake of the stationary body, at a distance of 0.25L downstream from the stationary body. These would allow for the capture of the flow interaction as the overtaking body passed the overtaken body.

In total 21 different planes were created to help analyze the flow interactions between the two bodies as they passed each other. Images showing where these planes were placed can be seen below in figure 27. At each of these planes, scalar scenes of Pressure Coefficient (C_p), Total Pressure Coefficient (C_t), Turbulent Kinetic Energy (k), Velocity components (V_x, V_y, V_z), and Vorticity (ω) were created. The simulation was set up to save images of these scenes automatically after every 5 time-steps. This resulted in over 110,000 images saved per simulation, which would later be used for a detailed analysis of the overtaking maneuver.

Once all the scenes had been created, and the baseline simulations were completed, the motion was applied to the overset region and the simulation was allowed to run for the 4 second physical time. Each simulation took approximately 9 days to run on

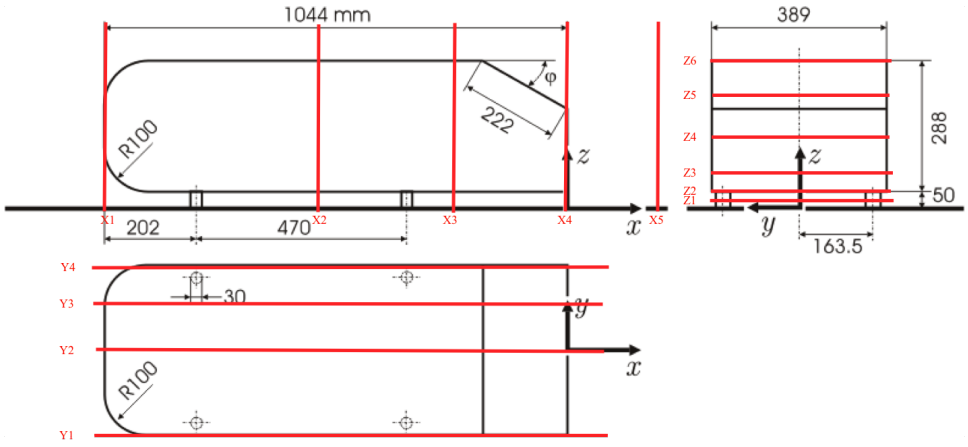

Figure 27: Locations of slices for scenes generated during the course of the simulation [7]

96 cores of 8-gigabyte RAM each.

CHAPTER 4: RESULTS AND ANALYSIS

With the mesh and physics set-up complete, and the initial run to convergence completed for the simulation, the simulation was allowed to run for the prescribed time. During the simulation data for drag coefficient (C_D), lift coefficient (C_L), side force coefficient (C_s), rolling moment (M_x), pitching moment (M_y), and yawing moment (M_z) were gathered and plotted, along with scenes generated for various parameters of the flow field surrounding the bodies. This chapter begins with the results of the mesh and physics selection studies on the single Ahmed body case, and then proceeds to analyze the results of the various force measurements and the underlying causes through the course of the simulation. The overtaking maneuver is broken down into various pieces of interest and the changes occurring highlighted in each of them. The section concludes by highlighting the limitations of the simulation.

4.1 Mesh Sensitivity Analysis

The single car simulation was first run at steady state using the $k-\omega$ turbulence model to determine the mesh size required to run the simulation. Various mesh sizes and structures were tested until a value of C_D for the single body case matching that of Serre et al. [7] was achieved, while also not changing with a further reduction in mesh size. The details of the final mesh used can be found in table 1, while images of the mesh distributions around the Ahmed Body and the entire computational domain

can be seen as figures 28 and 29, respectively. The mesh parameters chosen resulted in a mesh of 40 million cells for the single car case, and 45 million cells for the overtaking case.

Mesh Parameter	Value
Base Size	7.5 mm
Number of Prism layers	32
Prism layer Thickness	20 mm

Table 1: Mesh Parameters

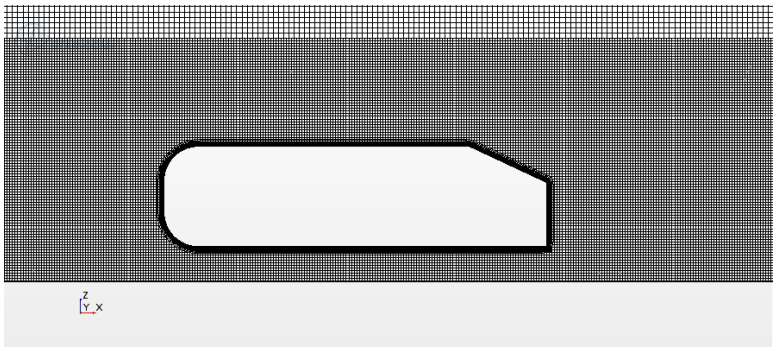

Figure 28: Mesh structure around the Ahmed body

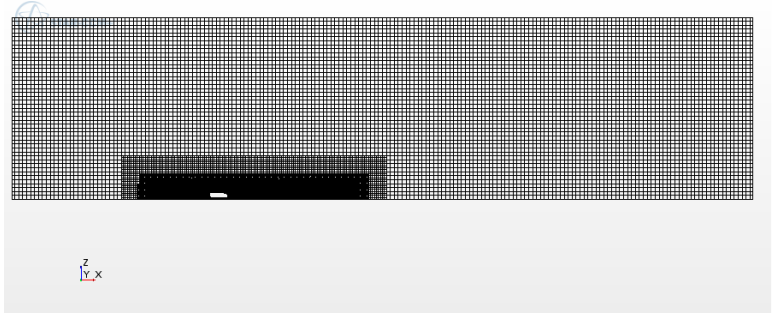

Figure 29: Mesh Structure of entire computational domain

The mesh structure selected was further reduced in base size and various other parameters to ensure the simulation had achieved mesh independence. The results showed that the simulation had indeed achieved this, with no significant change in results with a smaller base size. This state of mesh independence allowed for the

simulation to be tested using the different physics models to ascertain which one provided the most accurate results for the simulation in the unsteady state, in which the final simulation would be conducted.

4.2 Physics Model Selection

Once an appropriate mesh had been generated, the single car case was once again used to determine the physics model to be chosen for the unsteady simulation. To do so, the Realizable $k-\epsilon$, Standard $k-\omega$, and SST-Menter $k-\omega$ models were applied to 3 separate transient, URANS simulations and the system was allowed to run for a physical time of 0.5s, with a time step of 0.001s, consisting of 12 inner iterations per time step. This resulted in a total of 6000 iterations per simulation. Once again, the C_D value achieved was what was used to determine which physics model would be chosen for the overtaking simulation. A plot of the results of this simulation can be seen as figure 30.

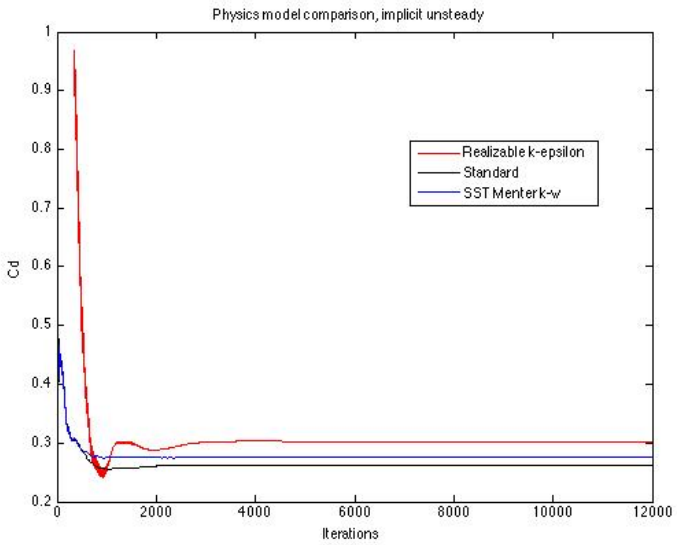

Figure 30: Plot of C_D using various turbulence models to see which came closest to the value defined by Serre et al. [7]

Once it became clear that all of the simulations had achieved convergence within the chosen number of iterations, the values of drag coefficient were analyzed to find which had come closest to the experimental results. The results of these simulations can be seen in table 2

	C_D Value
Experiment [7]	0.298
Realizable $k-\epsilon$	0.302
Standard $k-\omega$	0.280
SST Menter $k-\omega$	0.284

Table 2: Drag coefficient for single Ahmed body case for each turbulence model

From the plot and table generated it was clear that in an unsteady configuration, the Realizable $k-\epsilon$ model came closest to the experimental value of C_D obtained by Serre et al. [7], with a value of 0.302. As a result this was the chosen physics model for the simulation. The values obtained using this turbulence model, and the mesh parameters described earlier, were within 2% of the values described by Serre et al. and also in line with those described by Pagliarella's experiments [2] as well as Rajamani's [16] simulations. This helped to highlight the validity of the mesh and physics parameters selected, and provided a starting point for the overtaking simulation.

In order to further ensure the validity of the mesh and physics set up, and to confirm that the viscous sublayer was being captured by the selected physics model, scenes of wall y^+ values on the body were also generated and can be seen below as figure 31. In addition, a histogram showing the frequency distribution of y^+ values was created. The low y^+ values across the entire body, as well as the favorable

distribution, indicated that the simulation was successfully capturing the flow in the viscous sublayer using the realizable $k - \epsilon$ physics model.

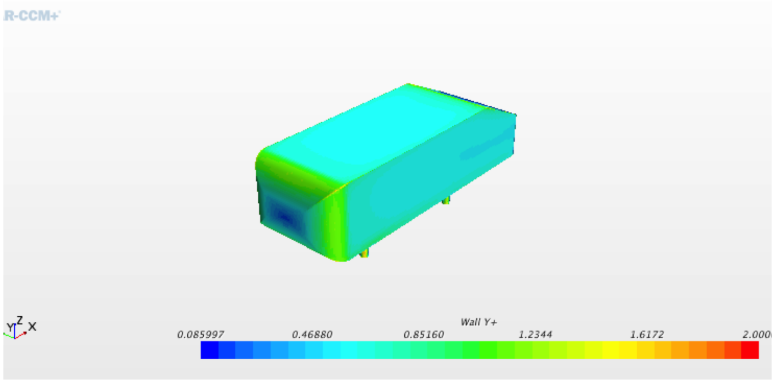

Figure 31: y^+ distribution on the lead Ahmed Body using the k-ϵ physics model

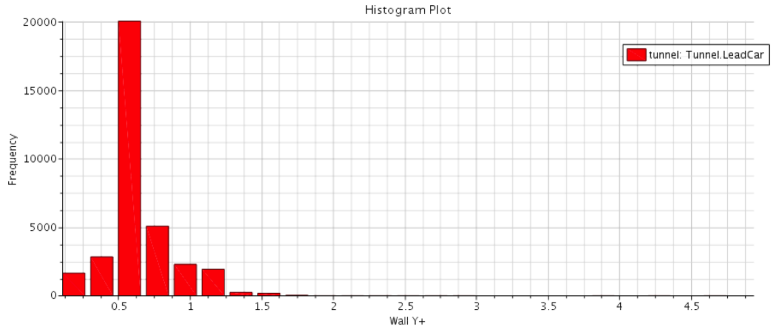

Figure 32: Frequency distribution of y^+ on the lead Ahmed Body using the k-ϵ physics model

Once the mesh and physics parameters had been selected, the overtaking body was added back to the simulation and the overset mesh surrounding it was defined. The mesh parameters around the overtaking body were the same as those around the static body, and can be seen in table 1. The simulation was then allowed to run with no motion condition until convergence had been achieved. Once this was done the motion parameter was applied to the Overset region, and the simulation was set to run for a physical time of 4 seconds, in time steps of 0.001s with 16 inner iterations

each, to ensure convergence before the overtaking body was moved. These values resulted in an overall simulation of 64,000 iterations, which took approximately 9 days to complete on 96 cores.

4.3 Data Reduction Approach

Once the simulation was complete and the initial results analyzed it became clear that significant post processing was required. While the plots for drag coefficient in figure 33, side force coefficient, as well as the moments appeared to follow the trends demonstrated by Noger's experimental studies [1] (see figure 36) as well as the CFD results obtained by Gillerion's studies [3] [19], it was apparent that there was significant noise present in the system. In order to help with the analysis of results a method of data smoothing was required.

The noise present in the system emanated from the numerical noises as the grid was not refined enough to resolve smaller scale motions below a certain frequency. The mesh chosen was coarser than that required by LES or DNS to ensure an acceptable solution time, while still maintaining a reasonably accurate engineering solution, as a result the contributions of the higher frequency modes to the force coefficients could be considered unphysical, representing numerical noise and needed to be removed.

Only large scale turbulence structures could be resolved spatially within the simulation due the coarser grid, and high velocity with which the simulation was run. These grid and time step values were chosen so as to keep the Courant number, a factor necessary for the convergence of the simulation, as small as possible while still maintaining a reasonable time for the simulation to run. The Courant number, C is

defined by

$$C = \frac{V\Delta t}{\Delta x} \tag{33}$$

In the equation above, V is the local velocity, Δx is the cell size, and Δt is the time step.

The dominant frequency in a system like this can be represented by the Strouhal number, which is defined as:

$$St = \frac{fL}{V_o} \tag{34}$$

Where f is the frequency of vortex shedding, V_o is the free-stream velocity in the system, and L is the characteristic length of the body. Gillerion et al. in [19] had found the maximum Strouhal number of two vehicles in an overtaking maneuver to be 0.2, which corresponds to a dominant shedding frequency of 8 Hz . Considering that current URANS methods only resolve the dominant large scale structures it is anticipated that the smaller structures with higher frequency may have insignificant effects on the force coefficeint variations. It is heuristically assumed that motions 1 order of magnitude smaller than this dominant frequency would have negligible results on the force coefficeint . As such, the force coefficient data were filtered as frequency of 64 Hz, using a MATLAB program developed by the author. The plots of raw data and smoothed data using the above procedures can be seen in figures 33 and 34 for drag and pitching moment coefficients, respectively. Cutoff frequencies larger than 64 Hz (128 Hz) were tried, and were seen to still contain some noise, while

anything below 64 Hz appeared to over-smooth the data, and eliminate some of the interesting trends.

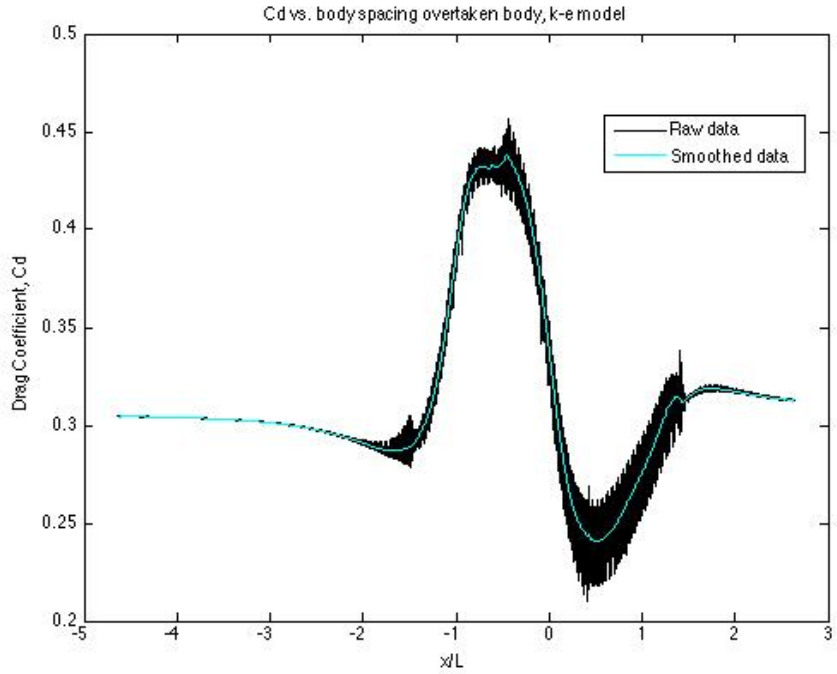

Figure 33: Drag coefficient of the overtaken body showing both the raw data and the smoothed data from the filtering procedure

As could be seen from the plots, the method chosen to smooth the raw data was effective in maintaining the trends followed, while eliminating a significant amount of noise from the system. The C_D and Pitching moment plots were chosen to test this method as they were the cleanest and most noisy sets of data, respectively. From the results above it became clear that procedure employed was capable of filtering the data.

4.4 Aerodynamic Coefficient Analysis

Running the data sets for the various coefficients through the smoothing function described above allowed for a far more accurate analysis of the effects of the passing

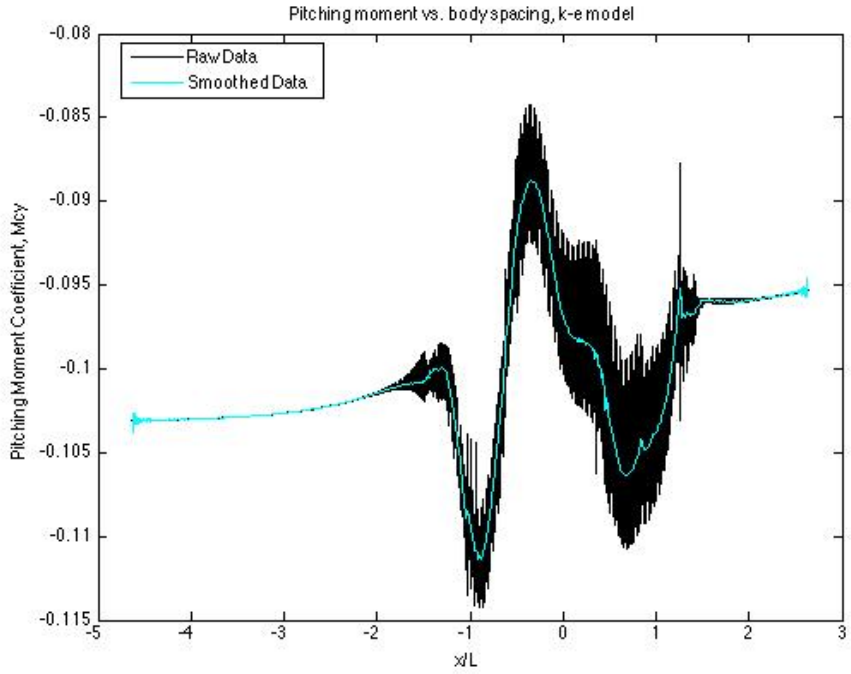

Figure 34: Pitching moment coefficient of the overtaken body showing both the raw data and the smoothed data from the filtering procedure

maneuver on the two bodies. First the plots of drag coefficient for the vehicle bodies using the selected physics models were generated, and can be seen below as figure 35.

The trends from the simulation appeared to match closely with the results from Noger et al. [1] for the overtaken body (figure 36). However, while the experimental results from Noger et al. described a maximum change in drag coefficient for the overtaken body of 0.16, the change shown in the simulation results were slightly smaller with the maximum change for the overtaken body being 0.13. This difference in values was probably due to the experiment having been conducted at a closer transverse spacing of $0.25W$, while the simulation being studied had the bodies separated by a distance of $0.5W$. As demonstrated by Noger et al. in figure 19 in chapter 2, as the separation between the two bodies increased, the effects of the overtaking maneuver

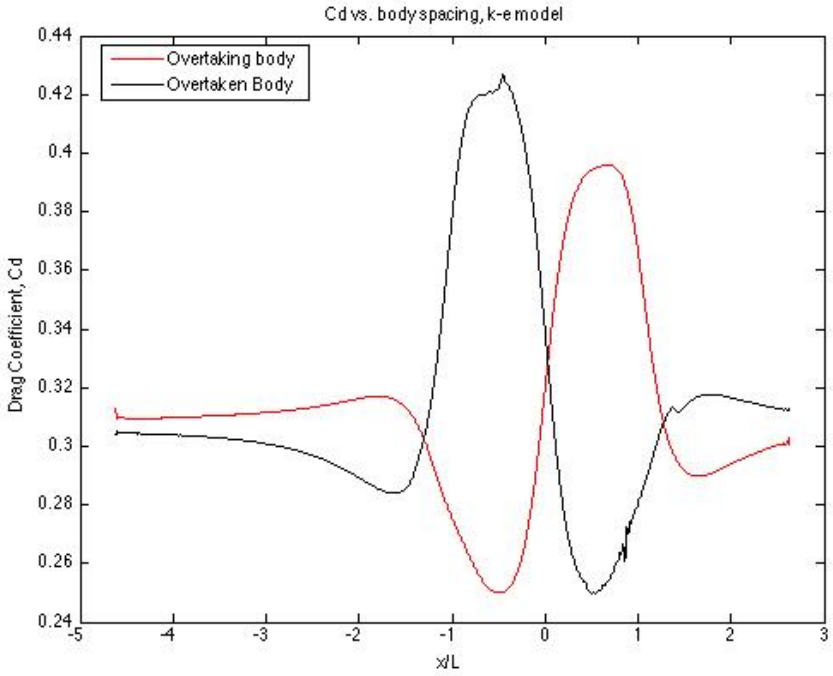

Figure 35: Drag coefficient of both bodies

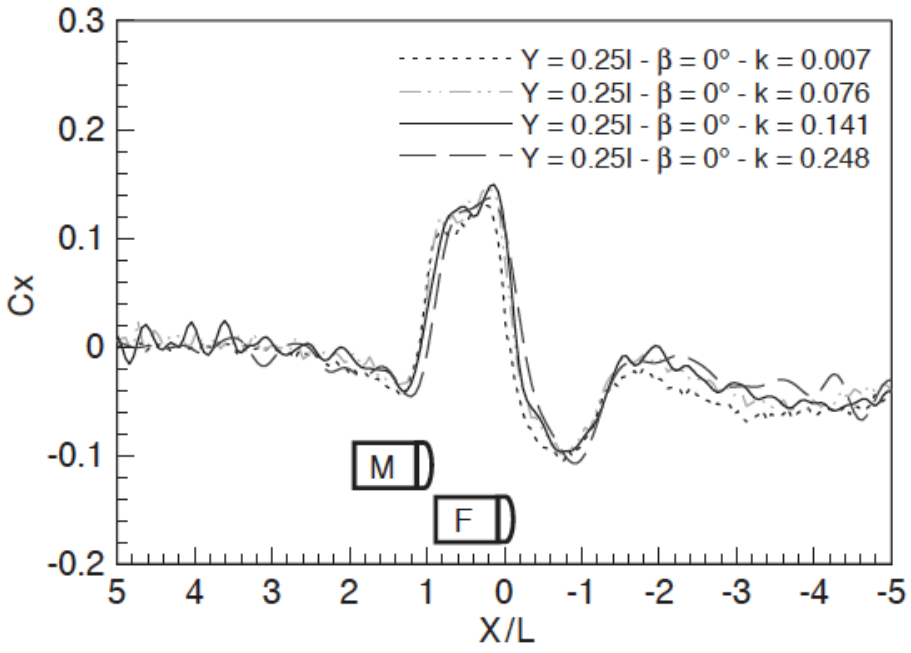

Figure 36: Effect of varying relative velocity V_r on C_D of overtaken body at a separation of $0.25W$. [1]

on the drag coefficient of the overtaken body decreased in magnitude, while maintaining the same trends. Noger's study did not contain data for the drag coefficient of the overtaking vehicle due to the difficulty of measuring these trends on the moving body.

From figure 35, which represents the drag coefficients of both bodies in the simulation, the first thing that became apparent was that at the initial separation the drag coefficient values of the two bodies were not the same. In fact, the drag coefficient of the overtaking body was significantly higher than that of the overtaken body. This result was in keeping with the studies conducted by Pagliarella [2], Watkins [14], Vino [15], Rajamani [16], and Watts [17], who had demonstrated that for two or more Ahmed bodies in convoy, there was an increase in drag on the trailing bodies. While the studies conducted by these researchers had been on Ahmed bodies in convoy, and not offset as in the simulation described here, the same principle effects were the causes for this phenomenon. The flow in front of the overtaken body was turbulent, but almost perfectly horizontal, while for the overtaking model this flow was affected by the wake impingement of the overtaken body in front of it, resulting in a higher pressure region at the front of the overtaking body and an increase in drag.

There was also a noticeable change in velocity of the Y and Z directions caused by the upstream body. For the overtaken body, the flow in front of it was almost perfectly horizontal, with no velocity in the Y and Z directions at all. However the interference of the body induced velocity components in both the Y and Z directions, the effects of which could still be seen at the front of the overtaking body. While the magnitude of velocity at the front of the overtaking body remained unchanged, its

components were affected causing a change in the drag coefficient of the overtaking body at these initial stages.

As the two bodies approached each other the drag coefficient for the overtaking body could be seen to increase slowly until the bodies were approximately 3 car lengths apart, with the drag coefficient of the overtaken body slowly declining until the same point. These trends follow those described by Rajamani's simulations [16], and show that the effects of wake impingement are felt even when the two bodies are not perfectly in line with each other.

Beyond that point the drag coefficient of the overtaken body began to decline more rapidly, reaching a first minimum at $X/L = -1.5$. The drag coefficient of the overtaking body in this same period rose slightly, reaching a local maximum at $X/L = -1.5$ At this point the front of the overtaking body was $0.5L$ behind the rear of the overtaken body, resulting in a strong interaction between the high pressure region at the front of the overtaking body and the rear of the overtaken body. Once again, these trends follow closely with those of Rajamani [16] as well as Pagliarella [2]. In the studies conducted by these researchers, the drag coefficient of the trailing body had appeared to reach a peak in this region, a result caused by the dramatic wake suppression of the leading Ahmed body, and the subsequent increase in pressure at the front of the trailing body. These results were highlighted in Chapter 2 of this report.

Beyond $-1.5L$ the drag coefficient of the overtaken body began to rise extremely rapidly, reaching a maximum when the front of the overtaking body was between $1L$ and $0.5L$ behind the front of the overtaken body. This peak in C_D for the overtaken

body at $X/L = -0.5$ also corresponded to a minimum in C_D for the overtaking body. The likely cause for these sudden and dramatic changes were changes in the interaction between the pressure fields of the two bodies, a factor which is studied in greater detail later in this report.

As the overtaking body pulled closer to being alongside the overtaken body from $X/L = -0.5$, the drag coefficient of the overtaken body began to drop rapidly, while that of the overtaking body began to rise. The drag coefficients of both bodies became equal as the two bodies became side-by-side. It was interesting to note, however, that the drag coefficients for both bodies at this point were higher than the free-stream drag coefficient of either body, a result which would be investigated in greater detail later on.

Once the overtaking body was past the overtaken body, the trends from above were reversed, resulting in a rapid rise for the overtaking body, and a rapid decline in that of the overtaken body. Beyond this point, the drag coefficient of the overtaking body dropped below that of the overtaken body where it remained until the end of the simulation.

In addition to the trends for C_D, the plots of side force coefficient (C_s) were also generated, and can be seen as figure 37. The results of this simulation corresponded well to those demonstrated by Gillerion and Noger [3], which can be seen for the overtaken body as figure 38. Once again, the experimental results only described the trends for the overtaken body. The experimental data provided by Gillerion [3] was for a separation of $0.7W$, and therefore had a slightly lower peak value of 0.13 than the 0.17 described by the simulation which had a separation of 0.5 W. Once

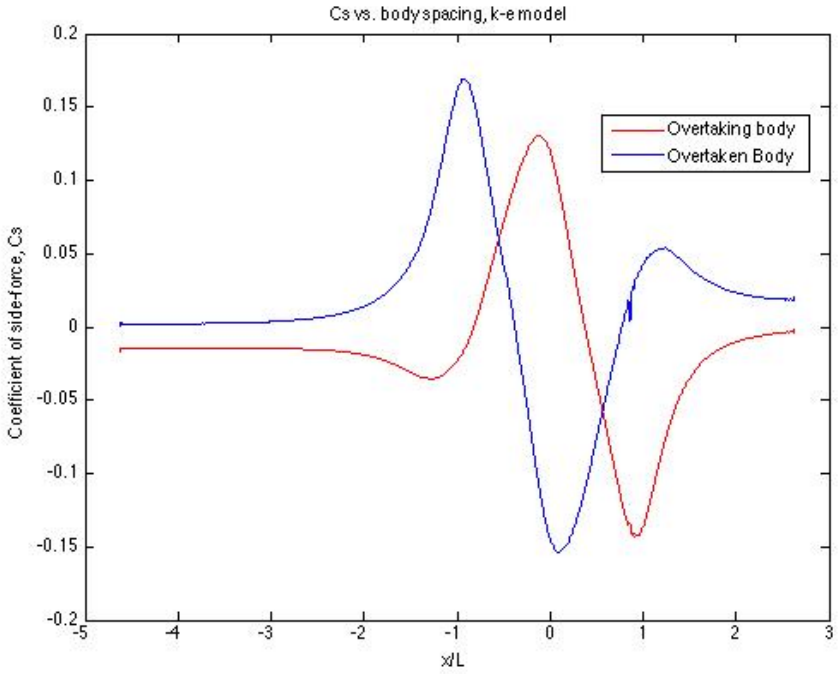

Figure 37: Side force coefficient of both bodies

again, as demonstrated by Noger et al. [1] and highlighted in figures 17 and 18, as the transverse spacing between the bodies increased, the side force coefficient of the overtaken body reduced.

For the overtaken body the side force appeared relatively constant until the overtaking body was within three car lengths of the overtaken body. At this point the side force began to rise rapidly, reaching a peak when the front of the overtaking body was in line with the rear of the overtaken body. This was likely caused by the interaction of the high pressure region at the front of the overtaking body and the low pressure region at the rear of the overtaken body, a factor which would later be confirmed when the scalar scenes generated at this point were more closely analyzed. This also corresponded to a change in the side force on the overtaken body in the opposite direction, indicating that the difference in pressure caused the nose of the overtaking

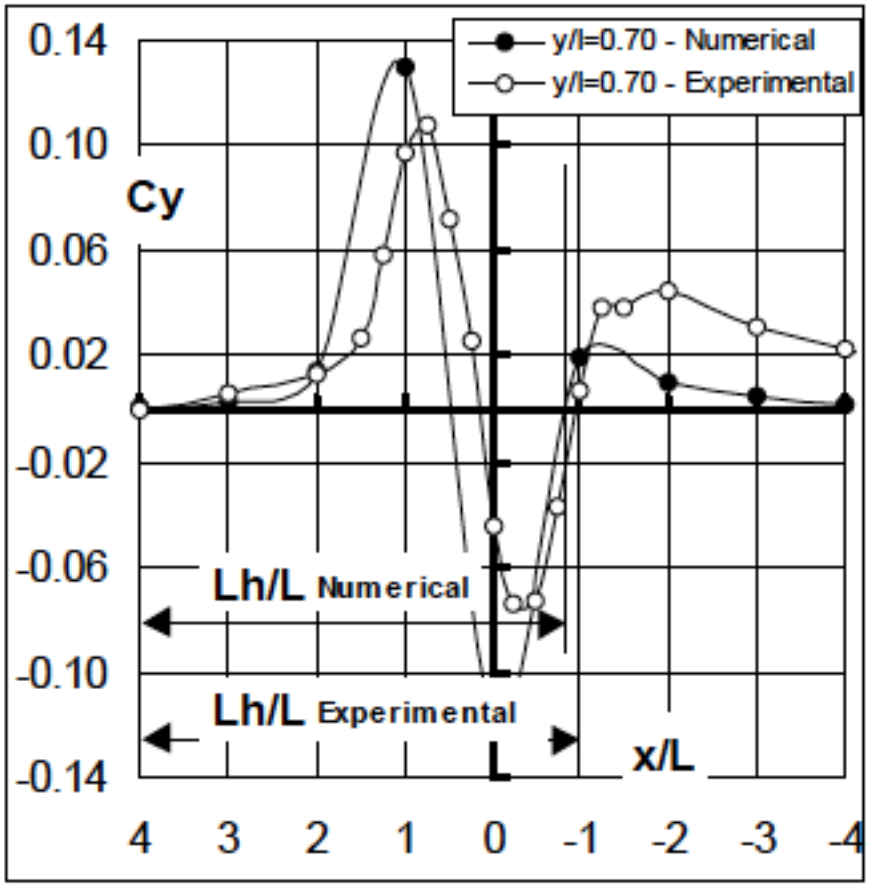

Figure 38: Plot of side force for the overtaken vehicle demonstrating the difference between the experimental and numerical results [3]

body to push against the tail of the overtaken body, a fact that was confirmed by the yawing moment of the overtaken body. As the two bodies moved side by side, the side force on the overtaken body and the overtaking body became approximately equal in magnitude, but opposite in direction indicating that the pressure region between the two bodies caused them to exert a force of almost equal magnitude on each other in the Y direction.

Once the overtaking body was ahead of the overtaken body, the trends from before were reversed. The side force coefficient of the overtaking body reached a peak value, in the direction opposite that of the overtaken body, when the nose of the overtaken

body was at its tail. Once again, this was likely caused by the high pressure region at the front of the overtaking body interacting strongly with the rear of the overtaken body, effectively pushing against it.

The similarity between the simulation results for drag coefficient and side force coefficient, and the results obtained by Gillieron [3] and Noger [1] highlighted the capability of the simulation to produce valid results, and subsequently allowed for a further analysis into the various force and moment components acting on the bodies, a feat which had not been undertaken before. The plot for lift coefficient for both bodies can be seen below as figure 39.

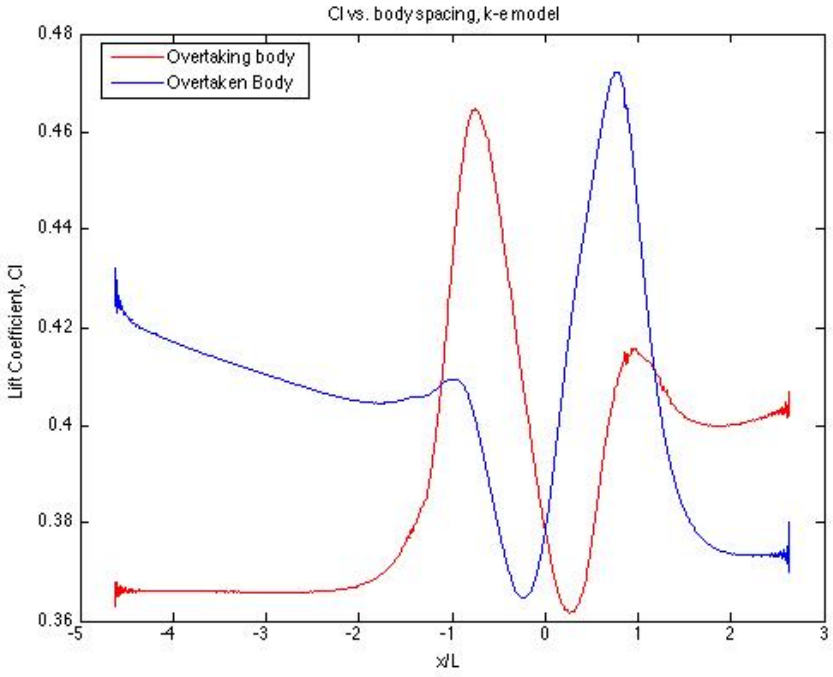

Figure 39: Lift coefficient of both bodies

From the plot generated it could be seen that the overtaken body initially produced a significant amount more lift than the overtaking body did. As the overtaking body moved closer to the overtaken body, the lift coefficient of the overtaken body began

to decrease slowly, while that of the overtaking body appeared to remain constant until a separation of $-2L$

Once the overtaking body was within 1 car length of the tail of the overtaken body ($-2L$ separation), its lift coefficient began to rise rapidly, reaching a peak when the nose of the overtaking body was at $0.75L$ behind the nose of the overtaken body. During the period from $-2L$ to $-0.75L$ the lift coefficient of the overtaken body began to rise slightly, reversing its previous trend. Beyond $-0.75L$ however, the lift coefficients of both bodies began to drop rapidly.

At $-0.25L$ separation, when the nose of the overtaking body was a quarter car length behind the nose of the overtaken body, the lift coefficient of the overtaken body reached a minima, and began to rise once again. As the two bodies pulled side-by-side ($0L$), their lift coefficients became equal, a factor which was expected.

Once the overtaking body began to pull ahead of the overtaken body, the trends were once again reversed, with the overtaking body reaching a minimum value of lift generated at $0.25L$, and the overtaken body reaching a maximum value of generated lift at a separation of $0.75L$. At larger separations, the lift generated by the overtaking body was now greater than that of the overtaken body, a reversal from the initial status of the two bodies.

Due to the relative motion of the overtaking body, implementing a coordinate system to analyze the moments on the body was made difficult. As a result, the moment plots were generated only for the overtaken body. Despite this limitation, the effects of the overtaking maneuver on the moment coefficients of the overtaken body were fascinating to see.

About the X-axis, the rolling moment coefficient for the overtaken body (figure 40) showed a very interesting trend, changing dramatically when the overtaking body was between $2L$ and $1L$ behind the overtaken body. The high pressure region at the front of the overtaking appeared to cause the overtaken body to roll until the overtaking body was directly at the rear of the overtaken body, beyond which it rose rapidly reaching a peak just past the where the two bodies were side-by-side.

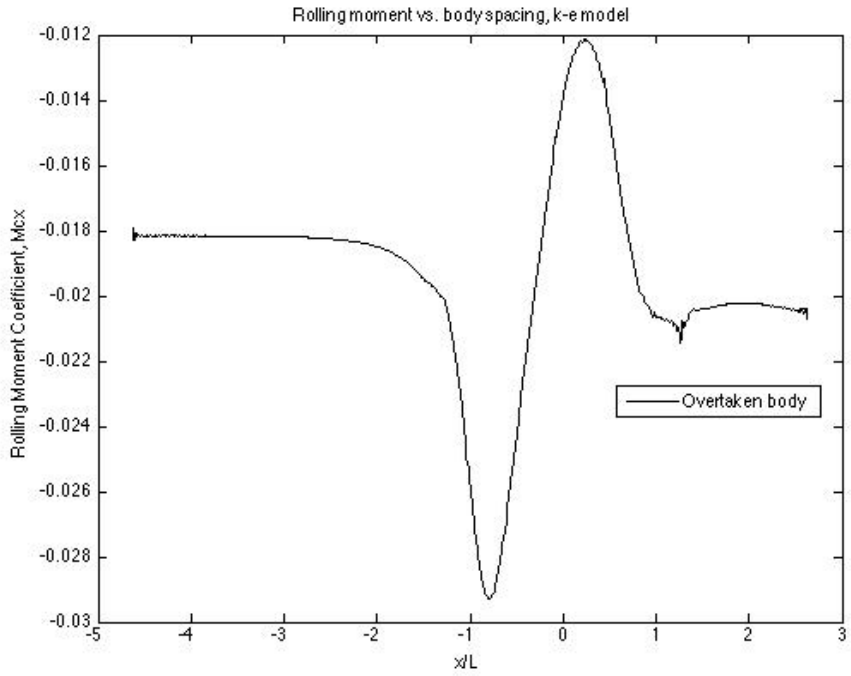

Figure 40: Rolling moment of the overtaken body

The pitching moment (about the Y-axis) was the set of data gathered that contained the most noise. The smoothed plot displayed in figure 41 shows the trends of the overtaken body as the overtaking body passed it. It reached a minimum value when the two bodies were side-by-side, but increased where the high- and low-pressure regions at the front and rear of each vehicle were interacting.

Noger et al. [1] showed the effect of the passing car on the yawing moment of the

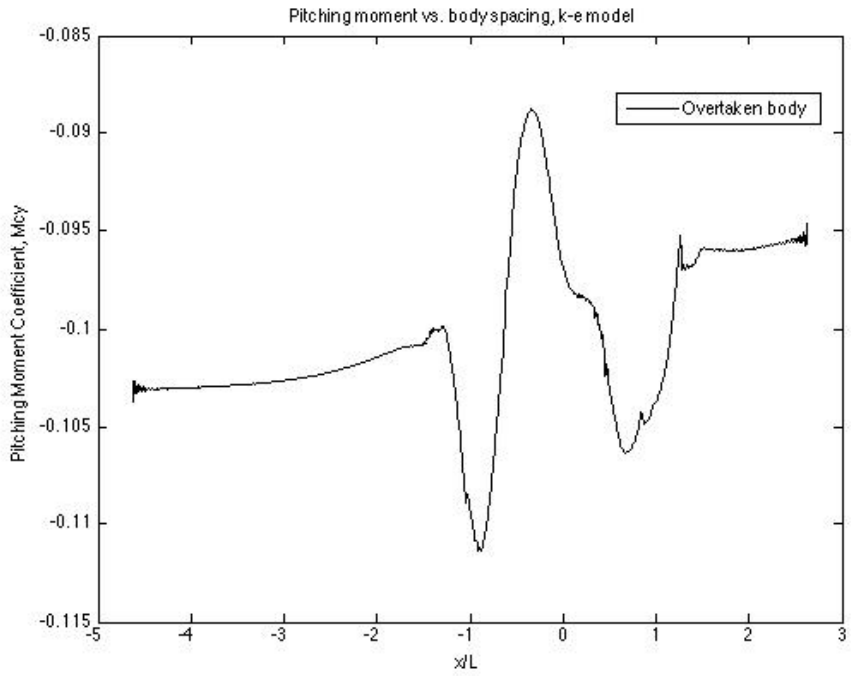

Figure 41: Pitching moment of the overtaken body

overtaken car (figure 17 and 18), and the plot generated by this simulation (figure 42) appeared to match the trend displayed. Between $-2L$ and $-1L$ the yawing moment decreased due to the interaction of the high- and low-pressure regions of the two bodies, beyond which it rose dramatically, changing direction, and reaching a maximum value in the positive direction when the nose of the overtaking body was halfway up the length of the overtaken body. Beyond this point the value began to fall again reaching a value of 0 as the cars were side-by-side. The value continued to drop until once again a peak was reached when the nose of the overtaken body was in line with the halfway point of the overtaking body. The value then began to rise again until it reached its original value when the overtaking body was $1.5L$ in front of the overtaken body.

To fully understand the causes for these trends, the analysis for the simulation was

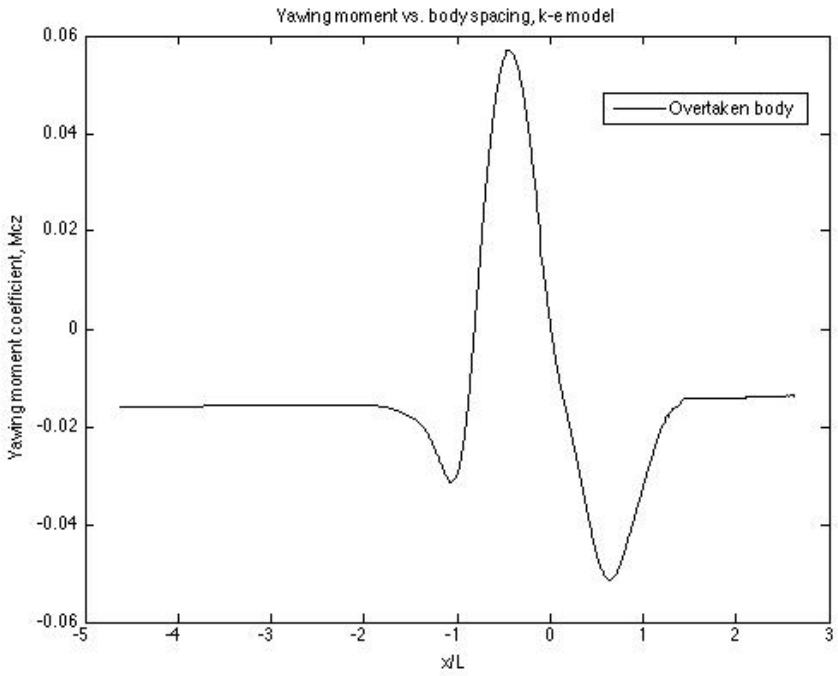

Figure 42: Yawing moment of the overtaken body

broken down into several smaller steps based on distance between the two bodies, and was analyzed in greater detail.

4.5 X/L from Initial to -1.5

To help more fully analyze the various effects occurring the passing maneuver, several scalar scenes were generated throughout the course of the simulation. In this section, these scenes are analyzed for the overtaking body being in positions between its initial position and $1.5L$ behind the overtaken body. During this phase of the simulation the drag coefficients of the body stayed very close to their initial values until the overtaking car was $3L$ behind the lead car. At this point the drag coefficient of the overtaking body began to rise slightly while that of the overtaken body began to drop, as can be seen in figure 35. These trends continued until the overtaking body

was about $1.5L$ behind the overtaken car, where the curves reached a local maximum and minimum, respectively. In the same region, the side force coefficient of the lead car stayed constant until the overtaking body was $3L$ behind it, at which point it began to rise gradually. This rise was accelerated when the overtaking body was within $2L$ of the lead body. During this phase, the side force on the overtaking body rose slightly from the initial position until it was $2.5L$ behind the overtaken body, at which point it began to drop until it reached a local minima at $1.5L$ behind the overtaking body.

These changes in C_D once again corresponded well with the results highlighted by the convoy studies of Watts [17] and Rajamani [16], and also with the overtaking experiments conducted by Noger [1]. The wake impingement described in the studies of Pagliarella and Rajamani, which caused the increase in drag for the trailing body, affected the trailing body significantly, and led to this increase in drag. Pagliarella's experimental study [2] had shown that the interaction between the two bodies began at this separation of $3L$ ($2L$ in that study, which measured distance from tail to nose, and not nose to nose as is used here), however as had been described by both Watts and Rajamani, when using CFD this effect is felt at much larger separations due to the limitations of the realizable $k - \epsilon$ turbulence model. As a result the effects of the wake impingement could be seen before this point, but became significantly more pronounced as the bodies drew closer to each other.

To properly understand the cause of these changes required investigating the scalar scenes generated during the simulation. Figure 43 shows the pressure coefficient across the middle of both bodies in the XY plane when the bodies were 3 car lengths apart,

nose to nose. In the image it could be seen that the low pressure region in the wake of the lead body was interacting very slightly with the high pressure region at the front of the overtaking body, indicating a part of the reason for the change in drag coefficients at this point. This interaction resulted in a mild suppression of the wake of the overtaken body, while slightly increasing the pressure at the front of the overtaking body.

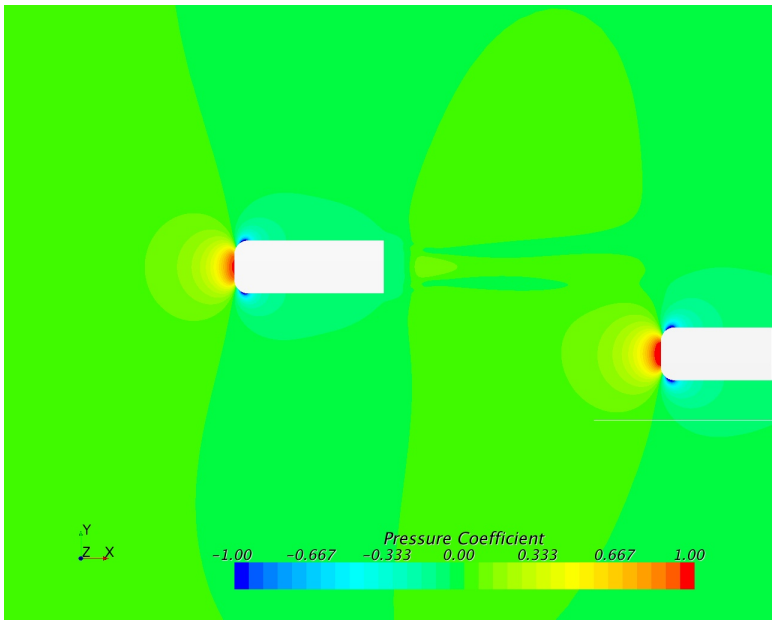

Figure 43: Pressure coefficient across the mid-plane of both bodies in the Z direction at $X/L = -3$

The scenes of velocity in the X, Y and Z (figures 44, 45, and 46, respectively) directions in this same plane give further evidence into the causes of the changes at this point. The velocity in the Y and Z directions in front of the overtaken body were negligible, however since the overtaking body lay in the wake of the lead body at this point, there was a significant change in these values, as could be clearly seen in the scenes generated. This interaction of low and high pressure regions and changes in velocity displayed likely causes for the trends observed in the drag coefficient and side

force coefficient of the two bodies. In the X-direction, the velocity in the wake of the overtaken body, on the side closest to the overtaking body, was in direct interaction with the front of the overtaking body, resulting in it being slowed in the X direction, a fact highlighted by the difference in the velocity field on the other side of the overtaken body.

The impingement of the wake on the front of the overtaking body, and the subsequent changes in velocity and pressure in both the wake of the overtaken body as well as the front of the overtaking body, provided a clear insight into the causes for the changes in drag coefficient for both bodies in the simulation.

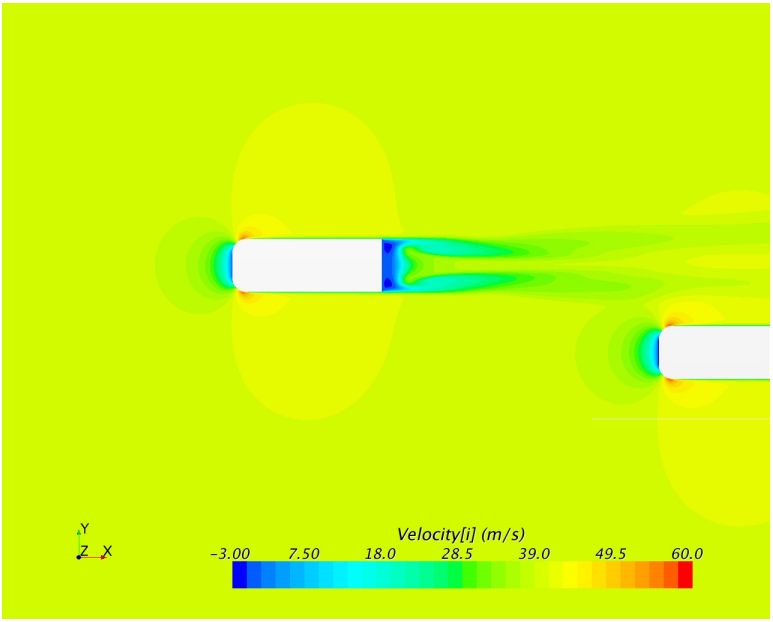

Figure 44: V_x across the mid-plane of both bodies in the Z direction at $X/L = -3$

As the overtaking body approached the rear of the overtaken body, these effects became more pronounced in the scalar scenes. When the overtaking body was $2.5L$ behind the overtaken body, the high pressure region at the front of the overtaking body began to interact more significantly with the wake of the overtaken body (figure

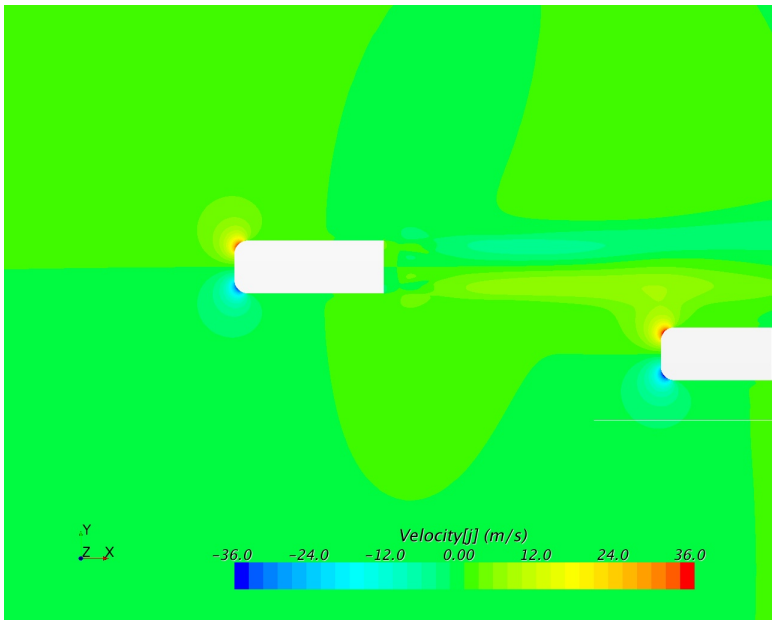

Figure 45: V_y across the mid-plane of both bodies in the Z direction at $X/L = -3$

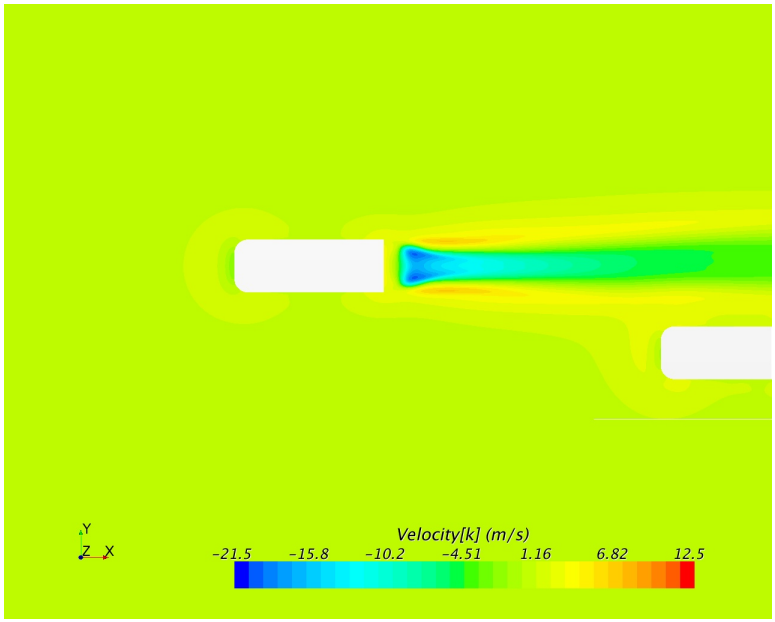

Figure 46: V_z across the mid-plane of both bodies in the Z direction at $X/L = -3$

47). It was at this point the side force on the overtaking body began to decrease slowly.

The effects of this interaction were also displayed in the scenes of velocity in the X, Y, and Z directions (figures 48, 49,50, respectively). As could be seen in the scenes of velocity components at this point, the front of the overtaking body began to notably

influence the velocity profile in the wake of the overtaken body. Comparing the figures of Vy at $X/L = -3$ and $X/L = -2.5$ (figures 45 and 49, respectively) showed the clearest indication of this effect. As the overtaking body pulled closer to the rear of the overtaken body, it began to slow down the velocity of the flow at the rear of the overtaken body, consequently changing the pressure field in the wake of this body.

During this phase the drag coefficient of the overtaken body was continually decreasing, while that of the overtaking body was rising at an almost equal rate 35. Once again, the two bodies were behaving similarly to two bodies in convoy. Despite being offset, the wake of the overtaken body was interacting enough with the front of the overtaking body that similar trends could be observed in both bodies.

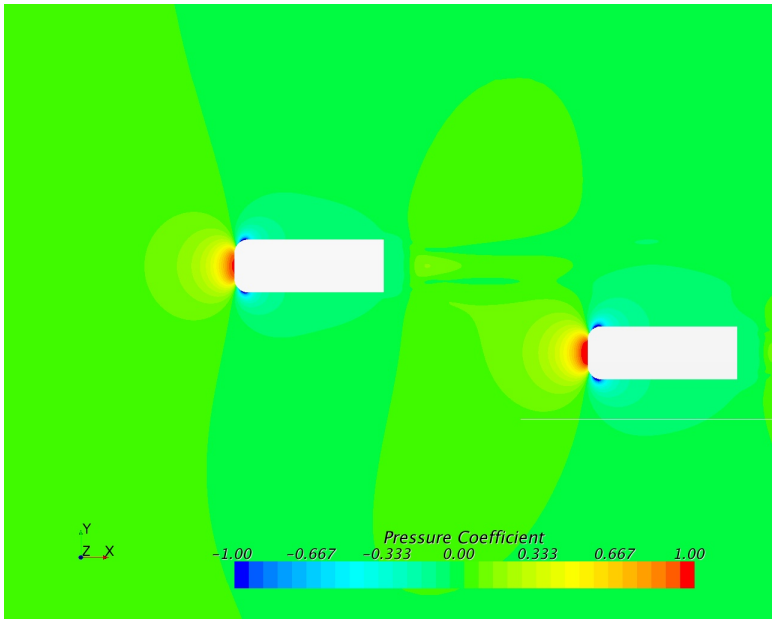

Figure 47: Pressure coefficient across the mid-plane of both bodies in the Z direction at X/L=-2.5

As the overtaking body advanced to a distance of 2L from the front of the overtaken body, the changes described above continued to increase in magnitude. The high pressure region of the overtaking body began to push further into the low pressure

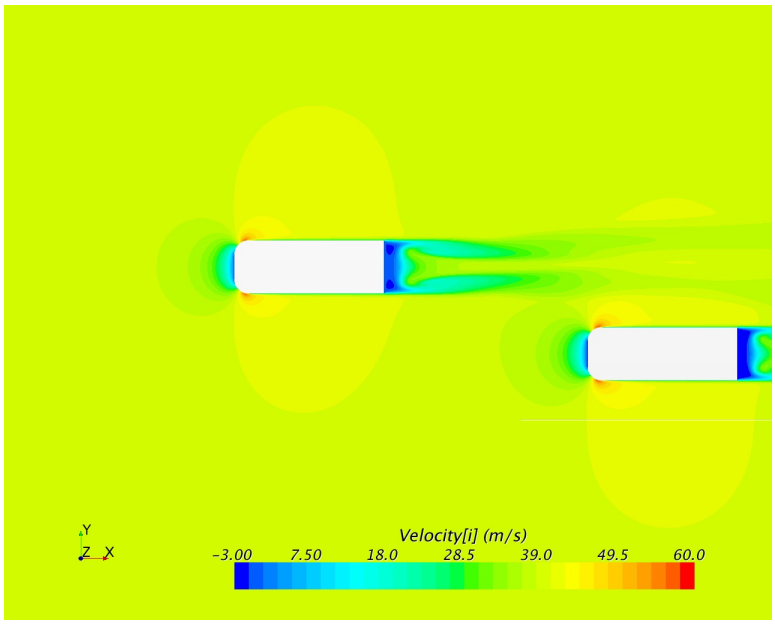

Figure 48: V_x across the mid-plane of both bodies in the Z direction at $X/L = -2.5$

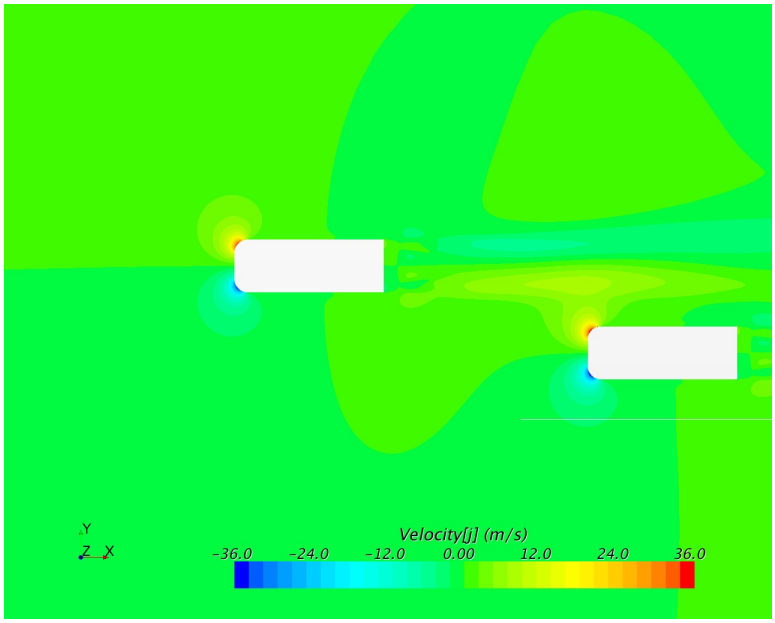

Figure 49: V_y across the mid-plane of both bodies in the Z direction at $X/L = -2.5$

region of the overtaken body, and consequently affect it to a greater extent.

It was beyond this point that more significant changes began to occur. When the overtaking body was $1.5L$ behind the overtaken body, the drag coefficient of the overtaken body began to rise rapidly, while that of the overtaking body began to drop.

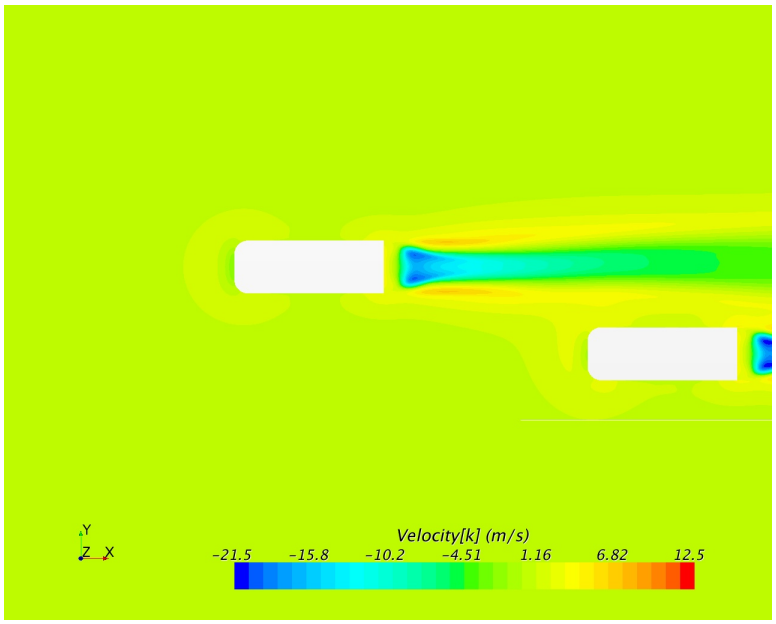

Figure 50: V_z across the mid-plane of both bodies in the Z direction at $X/L = -2.5$

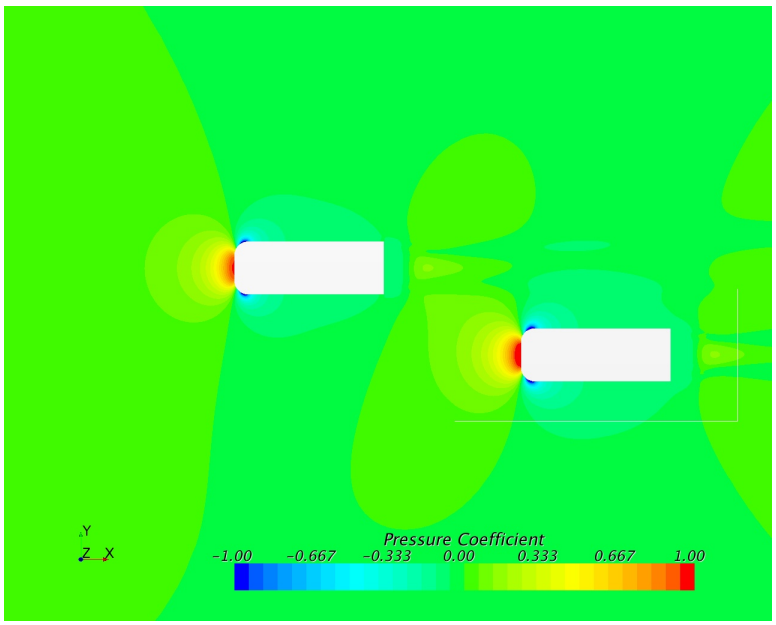

Figure 51: Pressure coefficient across the mid-plane of both bodies in the Z direction at $X/L = -2$

The side force coefficient of the overtaking body also began to rise more rapidly at this point, while that of the overtaking body dropped slightly. As can be seen in the scene for pressure coefficient (figure 55) at this point, these changes were due to the

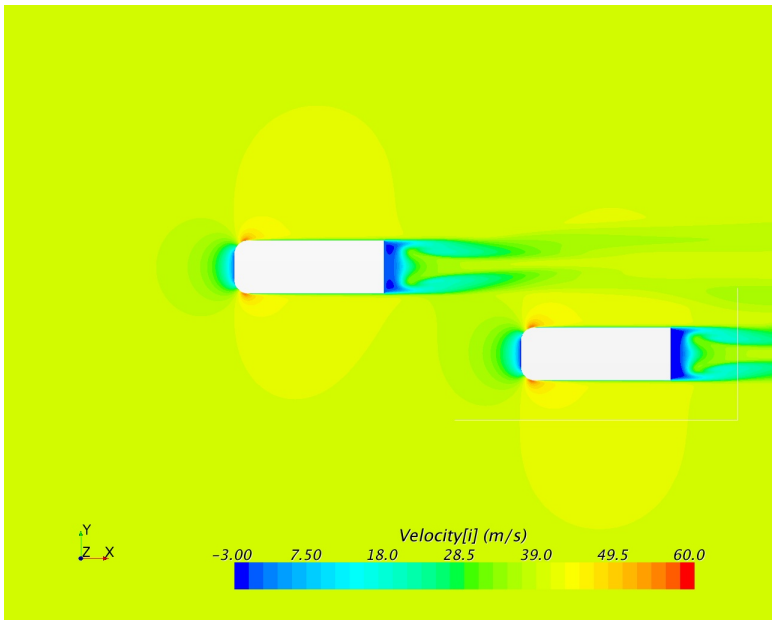

Figure 52: V_x across the mid-plane of both bodies in the Z direction at $X/L = -2$

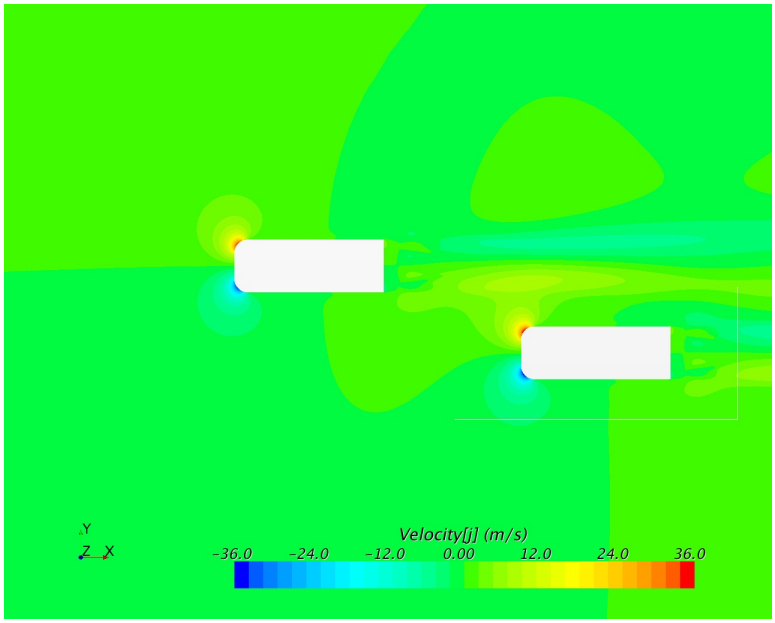

Figure 53: V_y across the mid-plane of both bodies in the Z direction at $X/L = -2.5$

difference in pressure between the two regions, the high pressure region at the front of the overtaking body interacting more directly with the low pressure region of the overtaken body, and inducing a moment on the overtaken vehicle, a change that can be seen in the plot of moment coefficient for the overtaken body (figure 42). To help

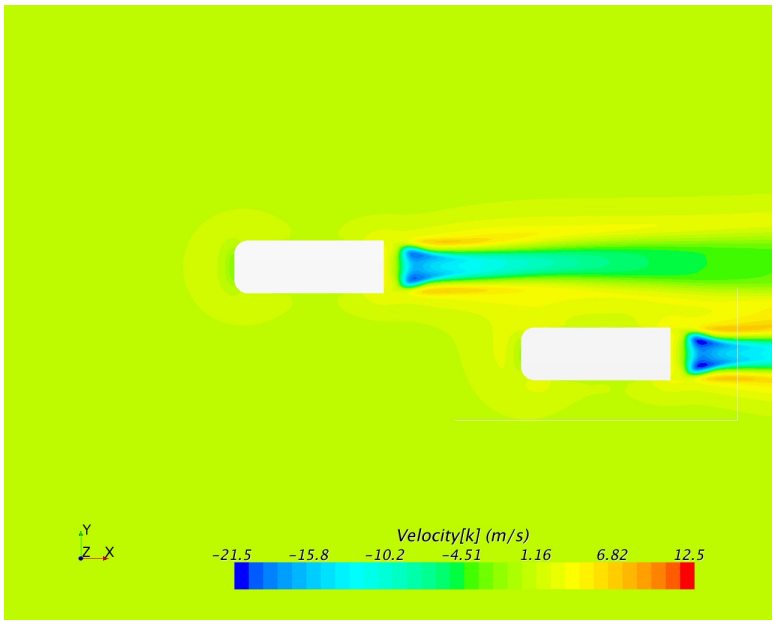

Figure 54: V_z across the mid-plane of both bodies in the Z direction at $X/L = -2.5$

fully understand the significant changes occurring to the flow structures at this point, plots of $C_p, C_t, V_x, V_y, V_z, k$, and ω are displayed in figures 55 to 61.

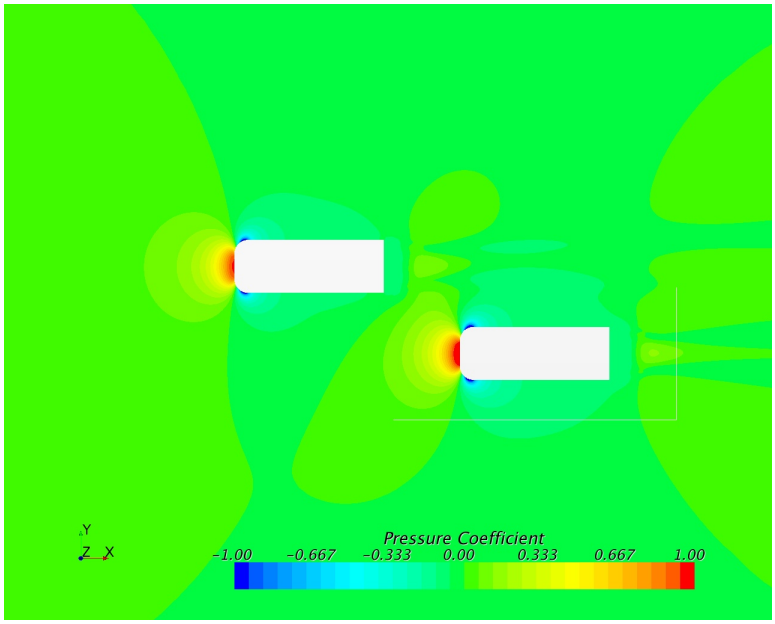

Figure 55: Pressure coefficient across the mid-plane of both bodies in the Z direction at $X/L = -1.5$

To help better understand the interaction of the wake of the overtaken body and

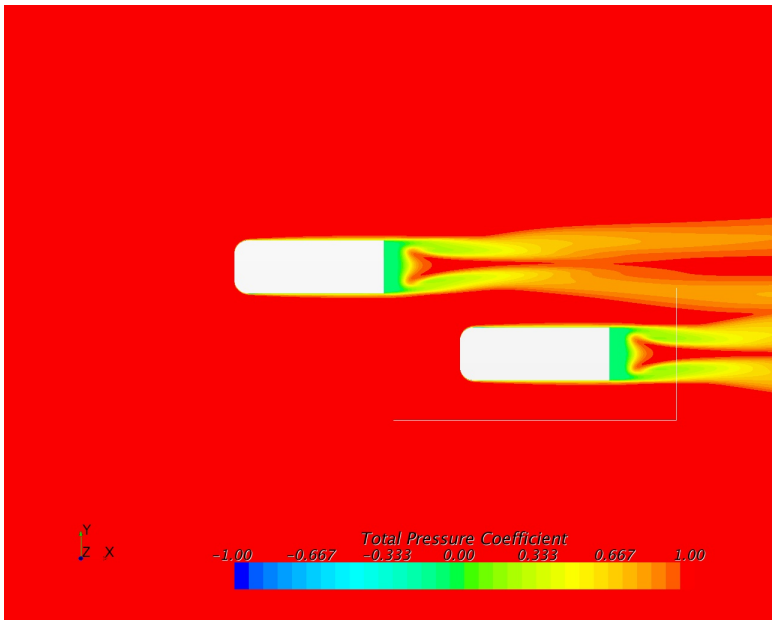

Figure 56: Total pressure coefficient across the mid-plane of both bodies in the Z direction at $X/L = -1.5$

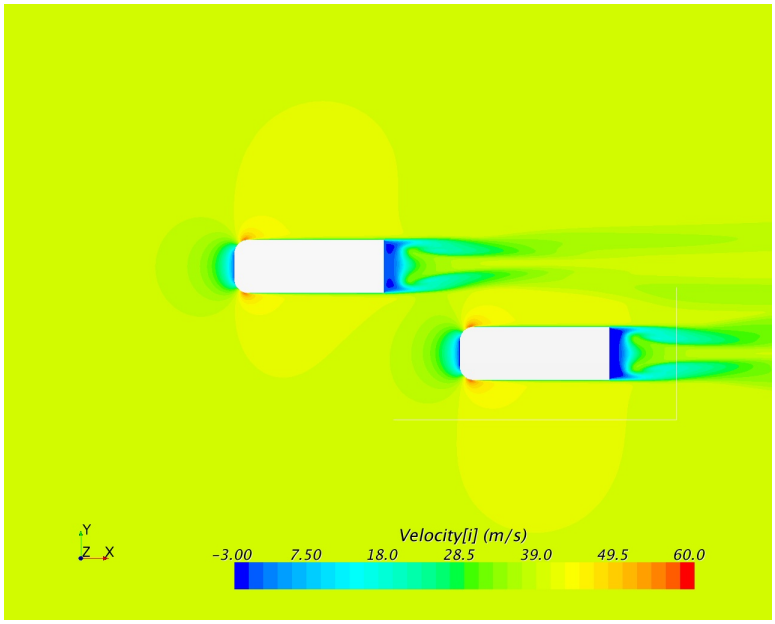

Figure 57: V_x across the mid-plane of both bodies in the Z direction at $X/L = -1.5$

the front of the overtaking body, scalar scenes were generated in the YZ plane at a distance of 0.25L behind the overtaken body, and can be seen below as figure 62. It was clear from this scene that the pressure field at the front of overtaking vehicle

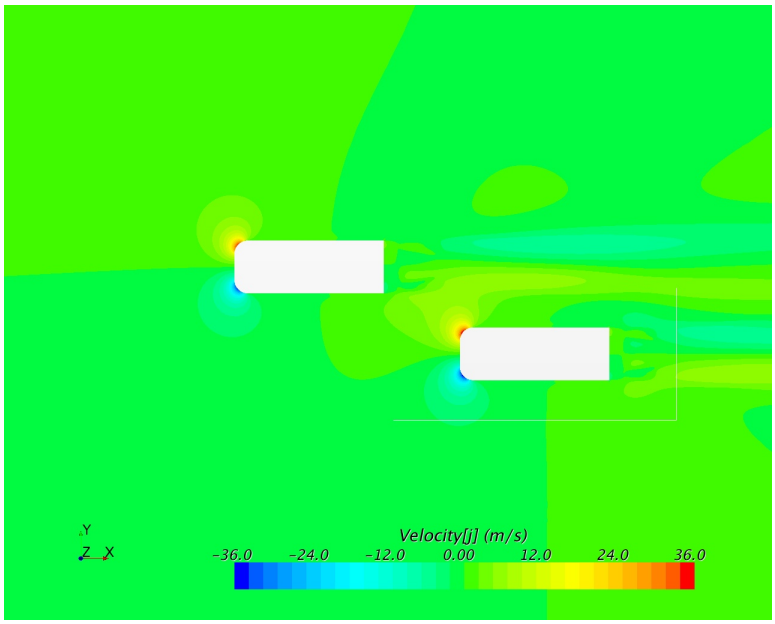

Figure 58: V_y across the mid-plane of both bodies in the Z direction at $X/L = -1.5$

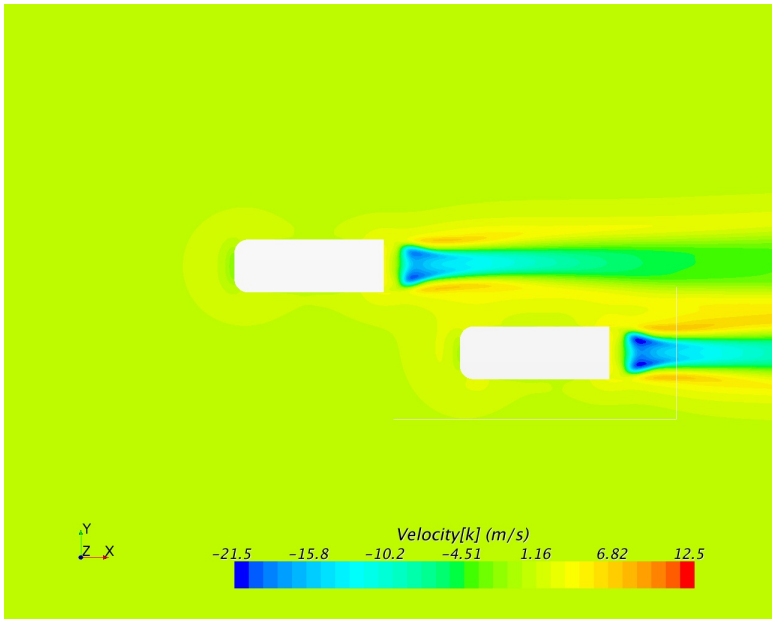

Figure 59: V_z across the mid-plane of both bodies in the Z direction at $X/L = -1.5$

(highlighted by the high pressure regions in the middle of the image) was already interacting quite significantly with the wake of the overtaken vehicle, even when the tail of the overtaken body was a full $0.5L$ in front of the nose of the overtaking body. As can be seen in the scene, the pressures across the two bodies was almost equal,

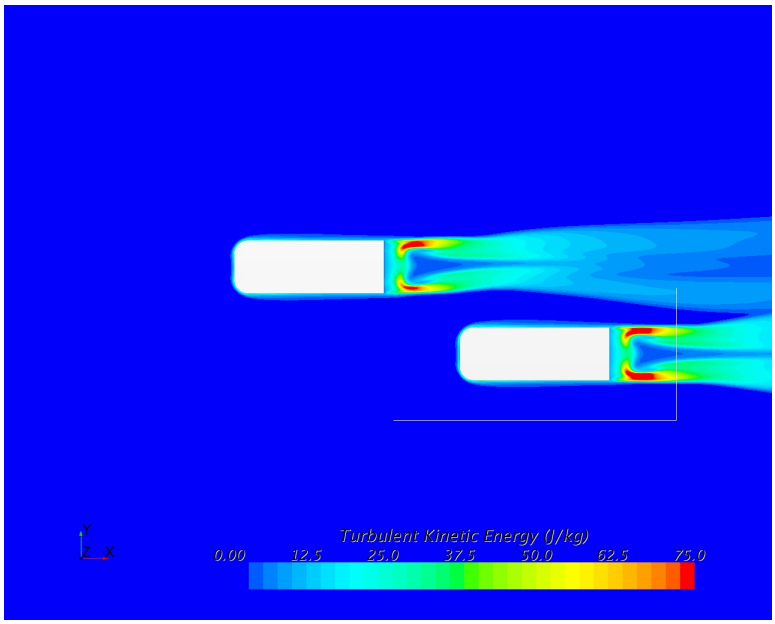

Figure 60: Turbulent Kinetic Energy across the mid-plane of both bodies in the Z direction at $X/L = -1.5$

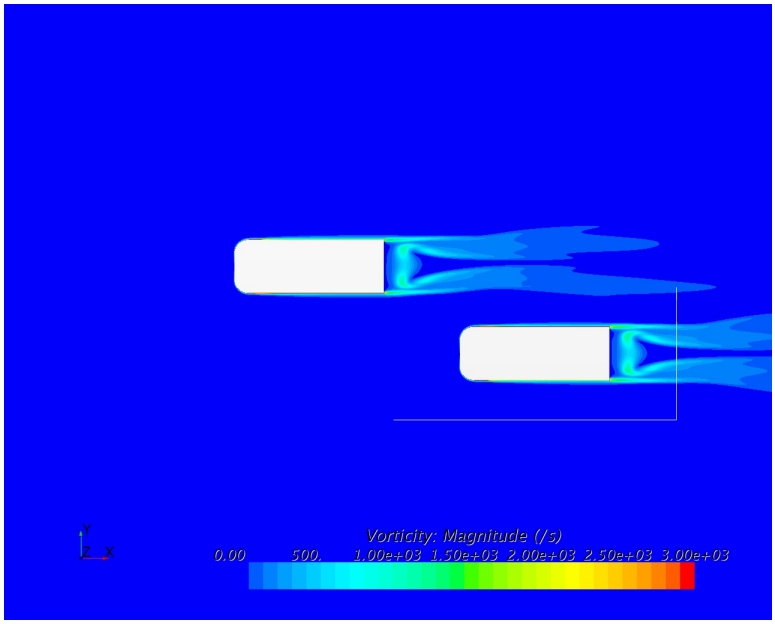

Figure 61: Vorticity across the mid-plane of both bodies in the Z direction at $X/L = -1.5$

where before there was a region of lower pressure in the trail of the overtaken body.

It was close to this separation of $-1.5L$ that Watkins [14], Vino [15], Pagliarella [2], Rajamani [16], and Watts [17] had all described the drag coefficient of the trailing

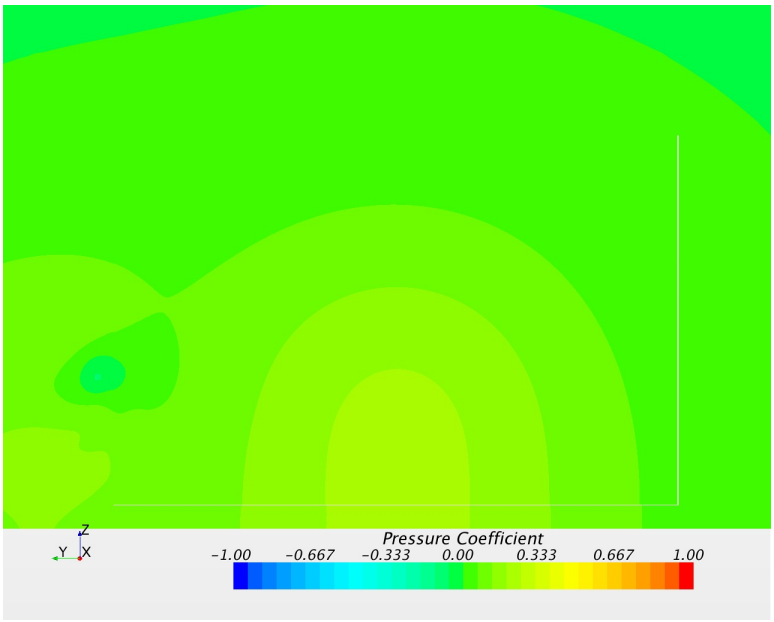

Figure 62: Pressure coefficient at a distance of $0.25L$ from the rear of the overtaken body in the YZ plane, $X/L = -1.5$

body in the convoy arrangement, corresponding to the overtaking body in this case, reaching a maximum. In the case of the overtaking maneuver, this also held true to an extent. The drag coefficient of the overtaking body reached a local maximum at this point, while that of the overtaken body (Lead body in the other studies) reached a local minimum. At this separation, the wake impingement effects were the most pronounced, with the high pressure region at the front of the overtaking body clearly suppressing the wake of the overtaken body far more than before, resulting in a region of higher pressure in the gap between the two bodies in the streamwise direction.

In addition to agreeing with the trends described by the convoy studies, the drag coefficient trends for the overtaken body matched very closely with those described by Noger et al. [1], which showed a similar minima for the drag coefficient of the overtaken body (figure 36). Beyond this separation of $-1.5L$ the bodies no longer behaved as much as a convoy as they had up to this point, and new and interesting

flow interactions began to develop. With the effects of both bodies on each other now being much larger, the subsequent interactions in the flow were analyzed in greater detail.

4.6 X/L from -1.5 to -1

When the overtaking body was between $1.5L$ and $1L$ behind the overtaken body significant changes could be observed in the various aerodynamic coefficients. At $-1.5L$, the drag coefficients of the overtaking and overtaken bodies had reached a local maxima and minima, respectively. The C_D of the overtaken body then began to rise extremely quickly, while that of the overtaking body decreased at a similar rate. The drag coefficient of the two bodies were equal when the overtaking body was $1.25L$ behind the overtaken body. It was at this point the side force on the overtaking body also reached a local peak, while the side force on the overtaken body began to rise more rapidly than before (figures 35 and 37).

The causes for this sudden change in attitude for both bodies were investigated using the scalar scenes. An explanation began to emerge when studying the scalar scene for pressure coefficient at $X/L = -1.25$ (figure 63). As the overtaking body began to draw closer to the rear of the overtaken body, the pressure field at its front was no longer interacting only with the wake of the overtaken body, but also with the body itself and the low pressure region along its side. This resulted in a suppression of the pressure field at the front of the overtaking body on the side of the overtaken body. This change in the pressure field was caused by the change in the velocity fields surrounding both bodies, as can be seen in figures 64 to 66. In the figure for V_x,

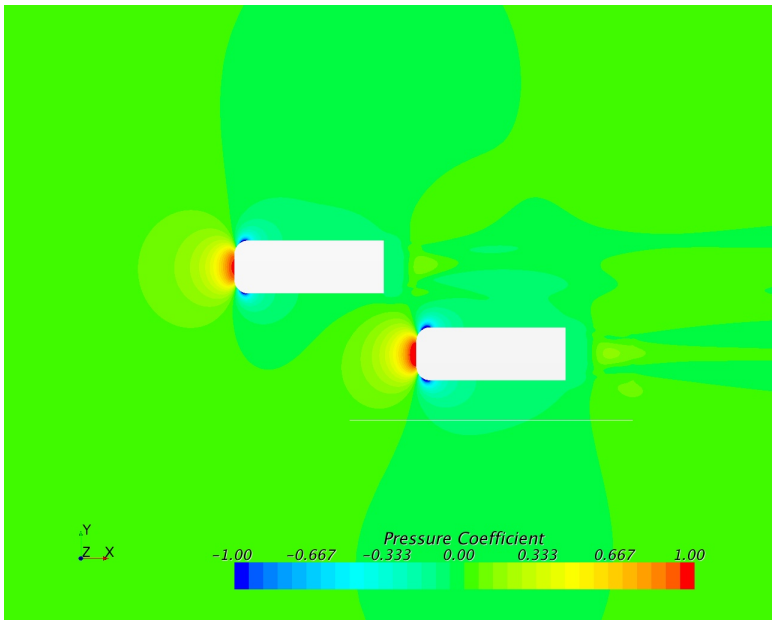

Figure 63: Pressure coefficient across the mid-plane of both bodies in the Z direction at $X/L = -1.25$

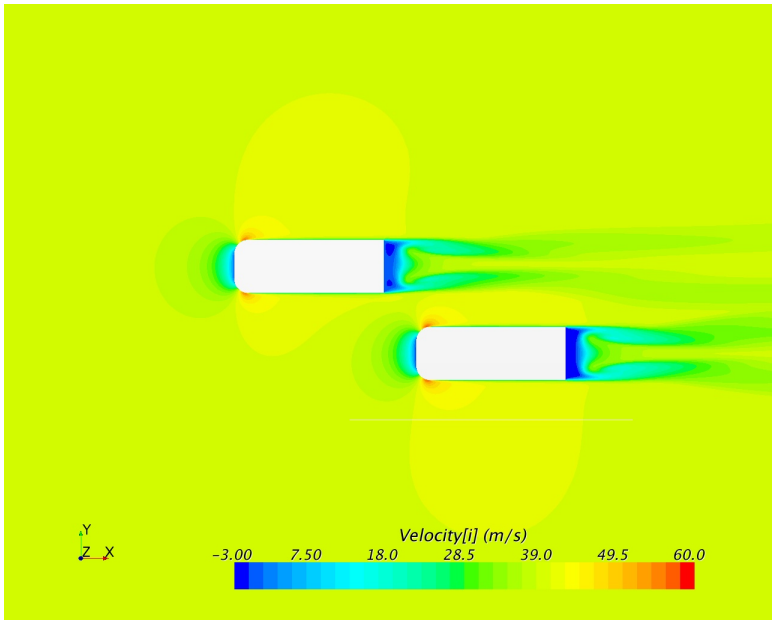

Figure 64: V_x across the mid-plane of both bodies in the Z direction at $X/L = -1.25$

the velocity field in front of the overtaking body showed a distinct change in shape, an effect caused by the high velocity flow in the gap between the two bodies. To compensate for this change in velocity in the X-direction, a region of higher velocity

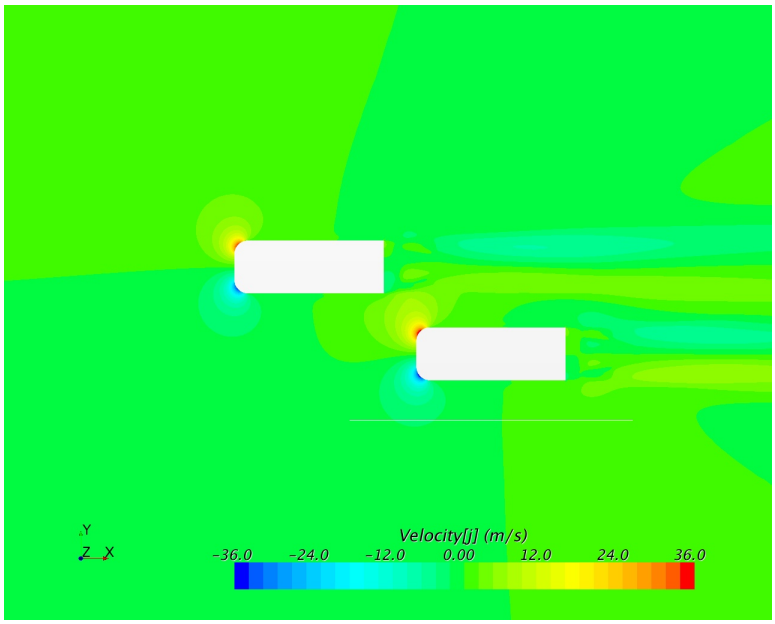

Figure 65: V_y across the mid-plane of both bodies in the Z direction at $X/L = -1.25$

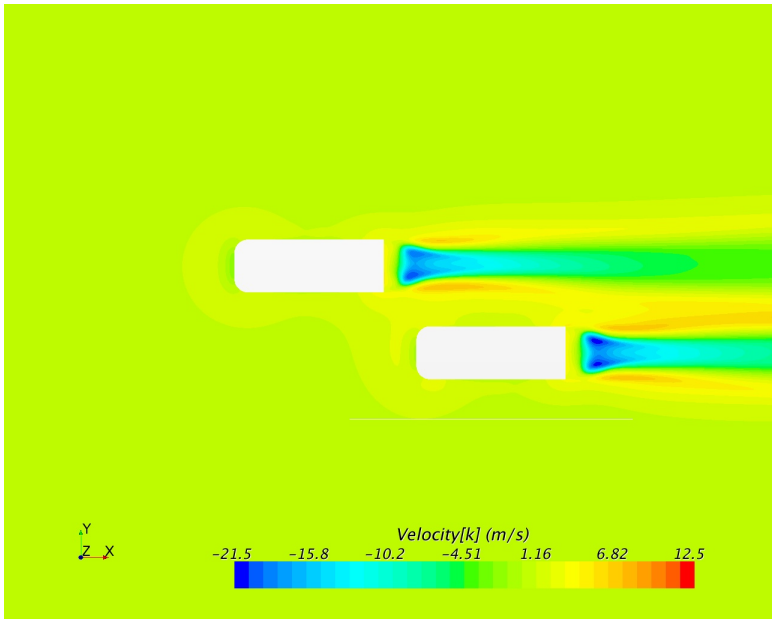

Figure 66: V_z across the mid-plane of both bodies in the Z direction at $X/L = -1.25$

in the Y and Z directions were noted at the front of the overtaking body. In the Y direction specifically, a pocket of higher velocity fluid was noted at the front of the overtaking body. This resulted in the fluid in front of the overtaking vehicle effectively pushing against the rear of the overtaken body, and accounts for the negative trend

in the yawing moment of the overtaken body.

These changes became clearer when looking at the image taken in the YZ plane at a distance of $-1.25L$ from the front of the overtaken vehicle (Figure 67). In this image the stagnation point at the nose of the overtaking vehicle comes into sharp focus and highlights the difference in pressure between the overtaking body and it's surrounding. The wake of the overtaken body was still being suppressed slightly by the presence of the overtaking body, the magnitude, however, had decreased from that demonstrated in figure 62, and as a result the drag coefficient of the overtaken body began to rise significantly.

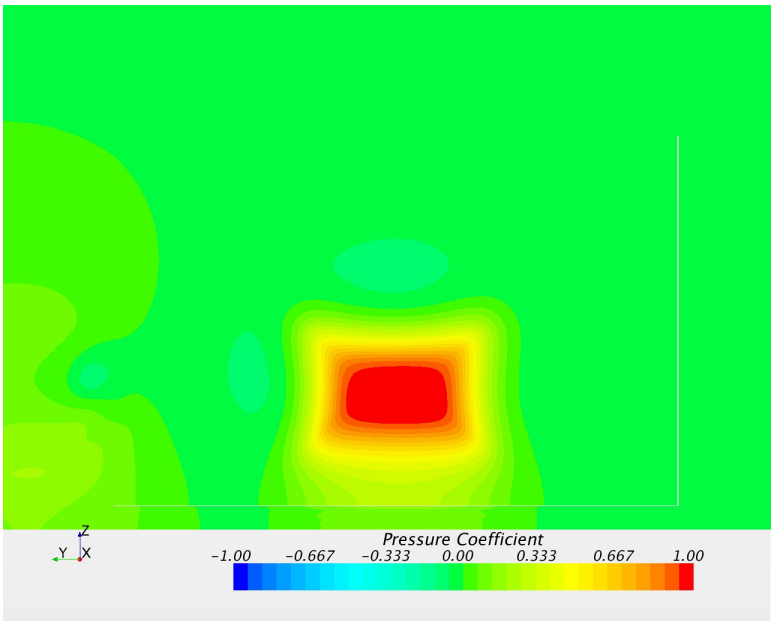

Figure 67: Pressure coefficient at a distance of $0.25L$ from the rear of the overtaken body in the YZ plane, $X/L = -1.25$. Image shows the Nose of the overtaking body as the high pressure region

Plotting the various velocity components at this same location show the interaction between the two bodies. In the scene of V_y (Figure 69) in this plane, the vortices generated by the overtaken body can be seen on the left side of the image. As

the overtaking vehicle approached the velocity in the Y direction induced by its motion began to interact with the flow at the rear of the lead body, forcing it to change shape and thereby affecting the air flow around the overtaken body. The large difference in pressures and velocities between the two bodies undoubtedly influenced the characteristics of both bodies, and help understand the change in the C_D and C_s observed earlier

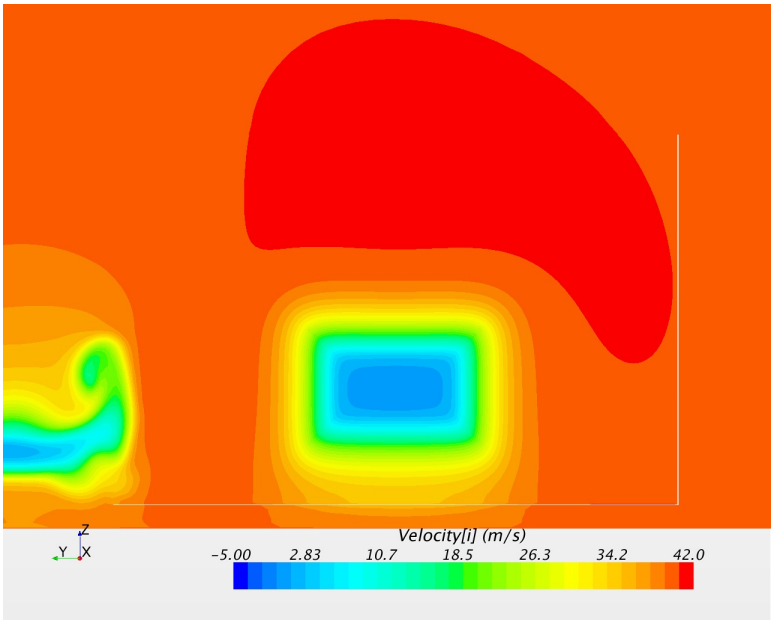

Figure 68: V_x at a distance of $0.25L$ from the rear of the overtaken body in the YZ plane, $X/L = -1.25$. Image shows the Nose of the overtaking body on the right side

When the front of the overtaking body was in line with the rear of the overtaken body, these pressure and velocity interactions became even more pronounced than before, resulting in a peak in the side force coefficient for the overtaken body, as well as it's yawing moment. Figures 70 to 73 showed that once again the pressure field at the front of the overtaking body was influenced by the presence of the overtaken body, resulting in a suppression of the pressure field towards the overtaken body. Again this suppression of pressure resulted in the fluid surrounding the overtaking

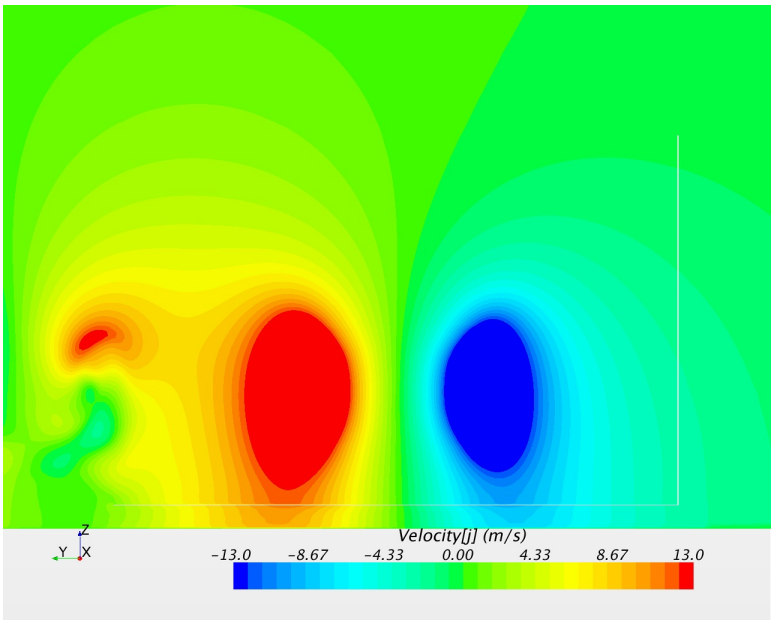

Figure 69: Vy at a distance of $0.25L$ from the rear of the overtaken body in the YZ plane, $X/L = -1.25$. Image shows the Nose of the overtaking body on the right side

body effectively pushing against the overtaken body, and causing the peaks in both side force and yawing moment about the center of the body. The results at this point matched very well with the side force measurements taken by Gillerion et al. [3], which also demonstrated a peak in side force for the overtaken body at this point.

With the pressure field at the front of the overtaking body now interacting less with the wake of the overtaken body, and more along its side, the rapid increase in drag coefficient for the overtaken body up to this point began to slow significantly, causing a noticeable plateau in the drag force coefficient of the body. The rate of change for the overtaking body also slowed considerably as a result.

To better demonstrate these changes in pressure and velocity fields, scenes were generated in the YZ plane at the rear of the overtaken body. Figure 74 showed the front of the overtaking body at the center of the image, with the rear of the overtaken body on the left. In this image a clear difference in pressure between the regions was

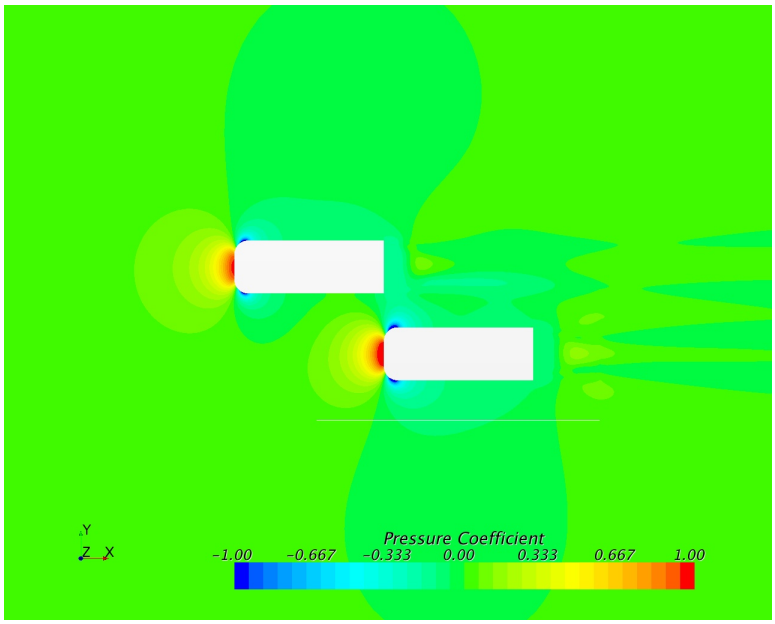

Figure 70: Pressure coefficient across the mid-plane of both bodies in the Z direction at $X/L = -1$

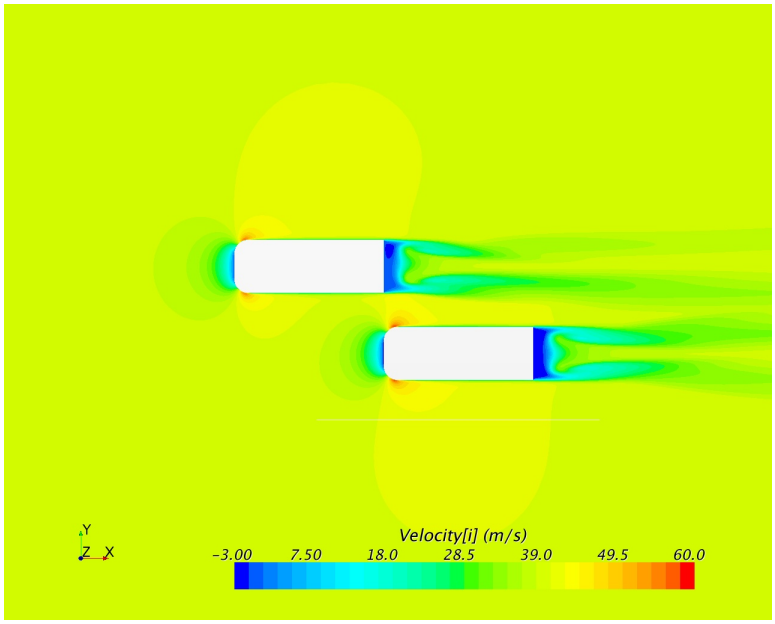

Figure 71: V_x across the mid-plane of both bodies in the Z direction at $X/L = -1$

noted, a factor caused by the interaction of the velocity fields visible in figures 75 to 77. As the front of the overtaking body caused an increase in velocity in the Y and Z directions, while stagnating it in the X direction, the velocity fields at the rear of

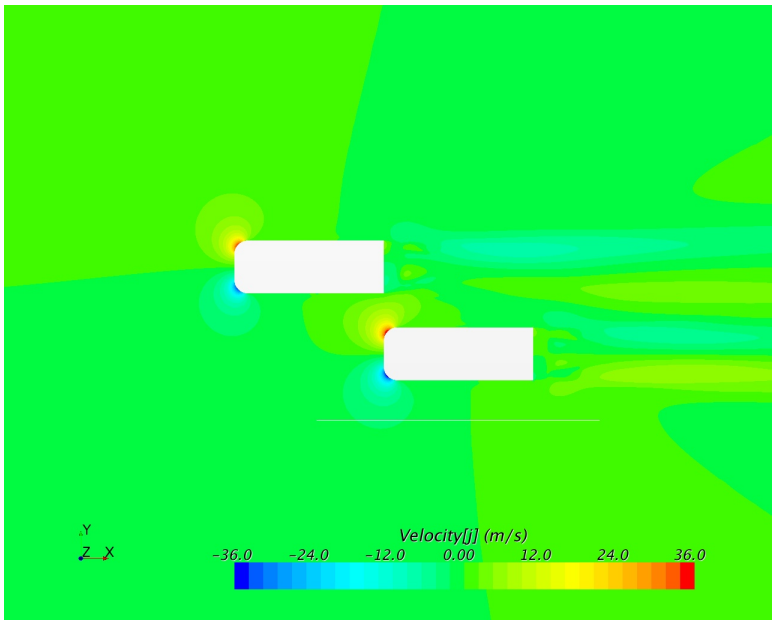

Figure 72: V_y across the mid-plane of both bodies in the Z direction at $X/L = -1$

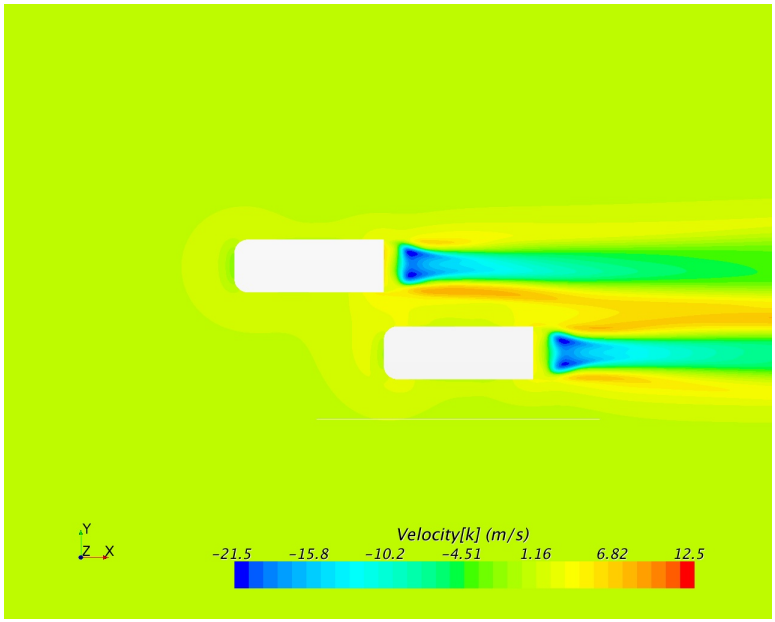

Figure 73: V_z across the mid-plane of both bodies in the Z direction at $X/L = -1$

the overtaken body were affected. Most notably again was the large velocity induced in the positive Y direction by the front of the overtaking body, which resulted in the peaks for side force and yawing moment noted earlier.

The images shown above highlight the effects the two bodies had on each other up

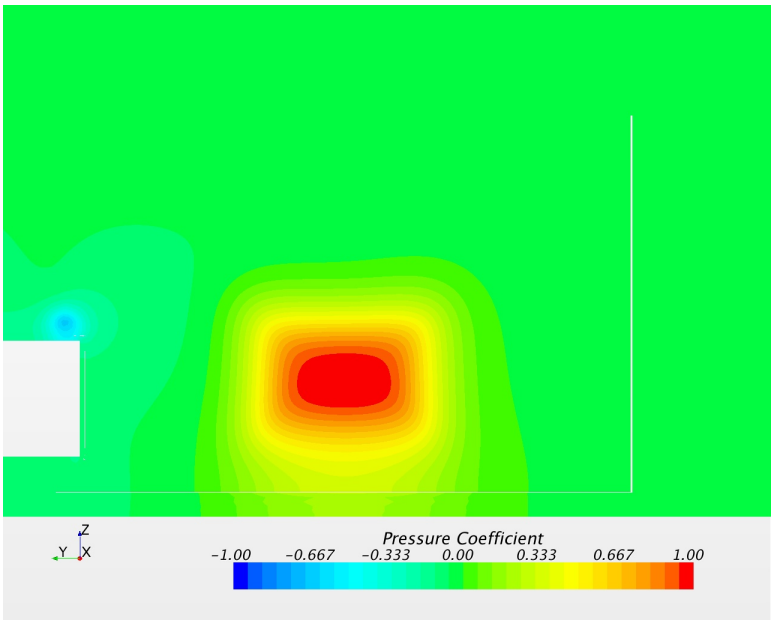

Figure 74: Pressure Coefficient at the rear of the overtaken body in the YZ plane, $X/L = -1$. Image shows the Nose of the overtaking body on the right side

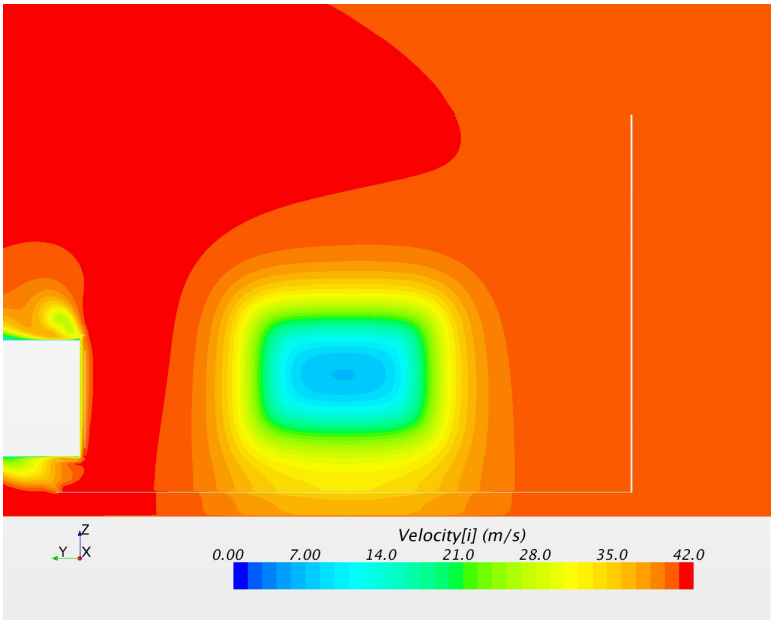

Figure 75: V_x at the rear of the overtaken body in the YZ plane, $X/L = -1$. Image shows the Nose of the overtaking body on the right side

to the point where the nose of the overtaking body was in line with the rear of the overtaken body. They demonstrated most significantly the changing effect of the high pressure region at the front of the overtaking body as it interacted first with the wake

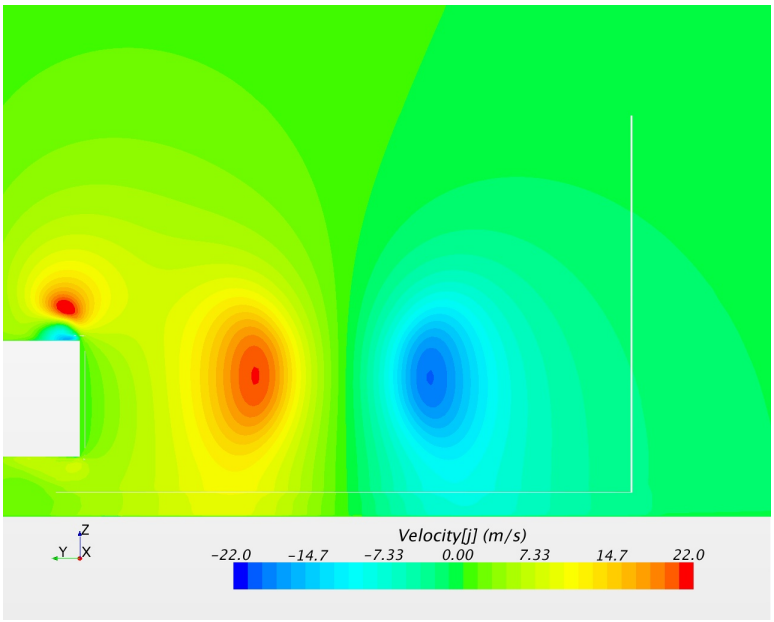

Figure 76: V_y at the rear of the overtaken body in the YZ plane, $X/L = -1$. Image shows the Nose of the overtaking body on the right side

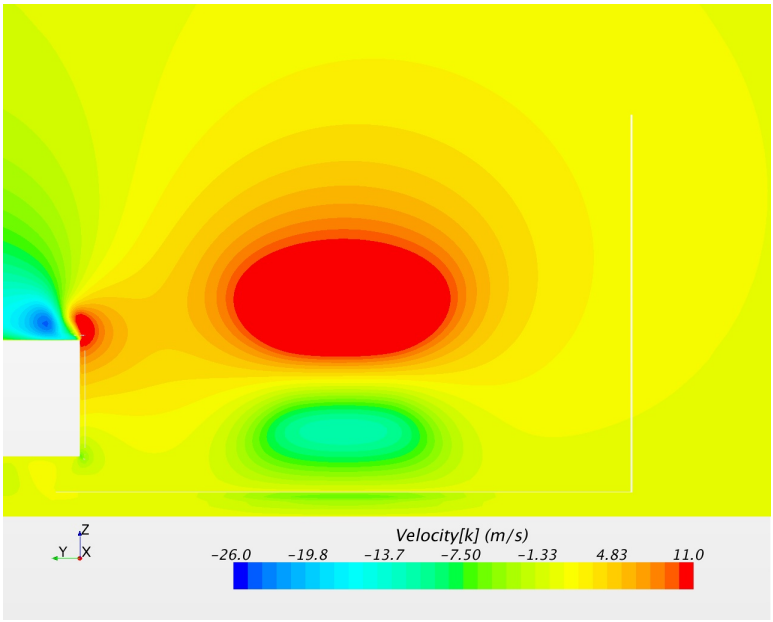

Figure 77: V_z at the rear of the overtaken body in the YZ plane, $X/L = -1$. Image shows the Nose of the overtaking body on the right side

of the overtaken body and subsequently with the body itself. These changes resulted in peaks for side force, drag coefficient, as well as yawing moment for the overtaken body. Beyond this point the interaction between this high pressure region and the

wake of the overtaken body would reduce significantly. The two bodies now no longer behaved as two vehicle bodies in convoy at all, and the majority of the interaction between them occurred in the gap between the two bodies, as opposed to the strong wake-stagnation interactions that had been noted before.

4.7 X/L from -1 to 0

As the front of the overtaking body pulled past the rear of the overtaken body and closer to being side by side, significant changes began to occur to the side force on the overtaken body. This coefficient had reached a universal maximum when the overtaking body was at the tail of the overtaken body, and its value began to drop rapidly past this point. This occurred due to the high pressure region at the front of the overtaking body no longer interacting directly with the low pressure wake of the overtaken body, but instead with the side of the body itself. In the case of the overtaking body, the side force coefficient began to rise as the bodies pulled closer to being side by side. The two values appeared to coincide when the nose of the overtaking body was approximately $0.5L$ behind the nose of the overtaken body, prompting further analysis into the causes for this.

Between -1L and -0.5L, the drag coefficients of both bodies followed an interesting trend. The drag coefficient of the overtaken body rose dramatically until $X/L = -1$, beyond which it continued to rise at a far slower rate, reaching a universal peak at $X/L = -0.5$. The drag coefficient of the overtaking body, however, did not show as abrupt a change, and continued to fall slowly until it reached its universal minimum at $X/L = -0.5$.

The plot of yawing moment coefficient was especially interesting at this point. When the overtaking body was at $-1L$, the yawing moment had reached a local peak, however, as soon as the overtaken body had crossed this point the moment changed signs extremely quickly. This helped to confirm the results indicated by the side force monitor, and explained the rapid drop off in side force past this point. This yawing moment appeared to hit a peak when the bodies were once again $0.5L$ apart. These various dramatic changes in the trends at this point prompted further analysis into the scenes generated.

The image of pressure coefficient along the XY mid-plane of both cars, displayed as figure 78 helped to explain some of the reasons for these changes. As the overtaking body approached the front of the overtaken body, the high pressure regions at the front of both began to interact with each other, as can be seen in figure 78. In addition, the low pressure region generated between both bodies grew significantly larger than it had been before. With the pressure and velocity fields at the front of the two bodies beginning to interact with each other, the yawing moment on the overtaken body reached a universal peak at this point. With the high pressure region of the overtaking body now interacting with the front half of the overtaken body, rather than the rear, the direction of yawing moment changed for the overtaken body.

In order to further analyze the effects at this point, several scenes were generated in the YZ plane at the mid-point of the overtaken body and can be seen below as figures 82 to 85

As can be seen from the images of pressure and velocity at in these scenes, there was a region of significantly higher velocity and lower pressure in the gap between the

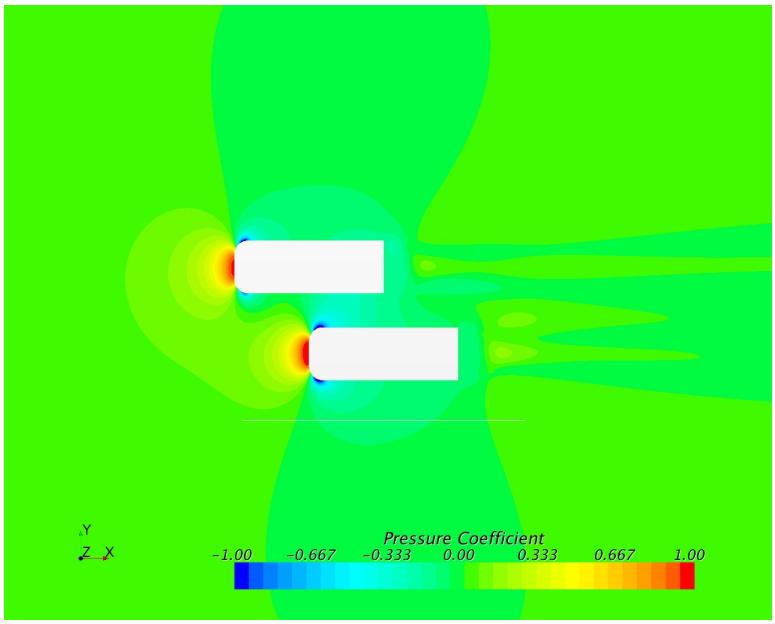

Figure 78: Pressure coefficient across the mid-plane of both bodies in the Z direction at $X/L = -0.5$

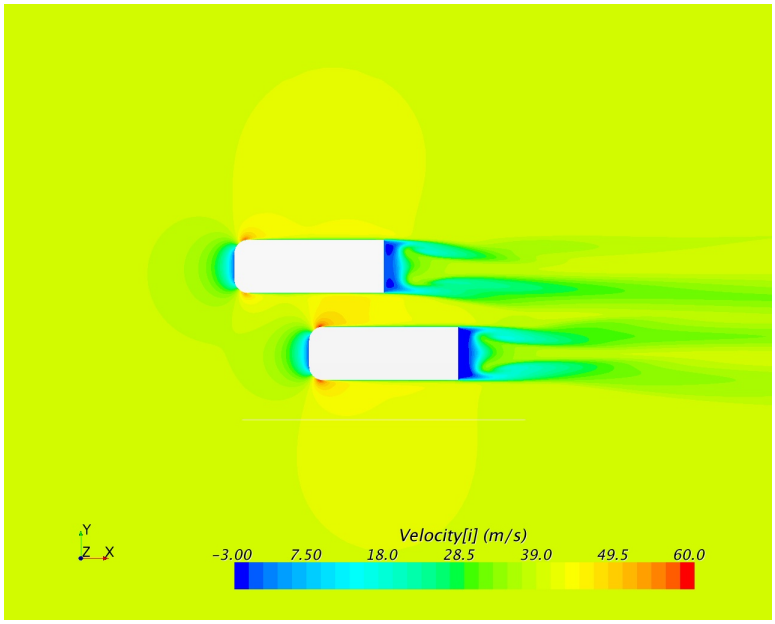

Figure 79: V_x across the mid-plane of both bodies in the Z direction at $X/L = -0.5$

two bodies this point during the overtaking maneuver, causing a change in almost all the aerodynamic coefficients on both bodies. To further analyze the various changes occurring in the gap between the bodies, scenes were created in the XZ plane as well.

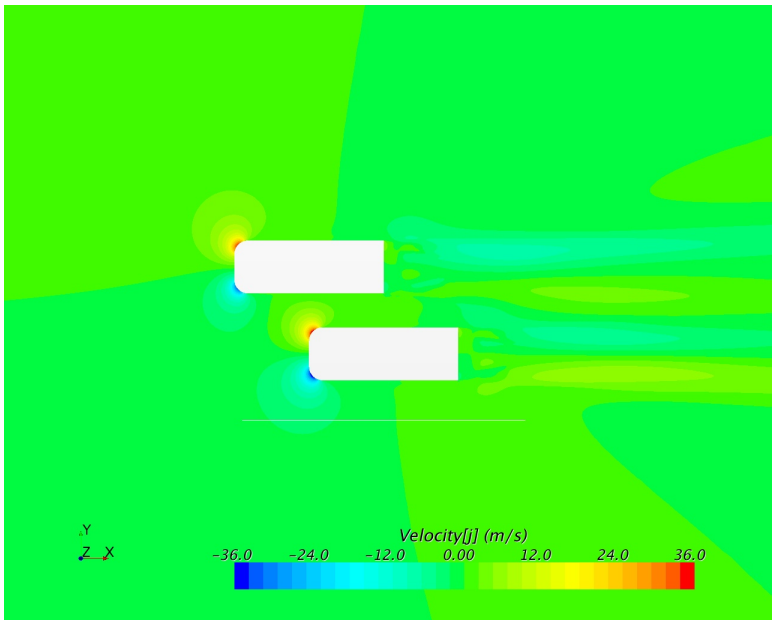

Figure 80: V_y across the mid-plane of both bodies in the Z direction at $X/L = -0.5$

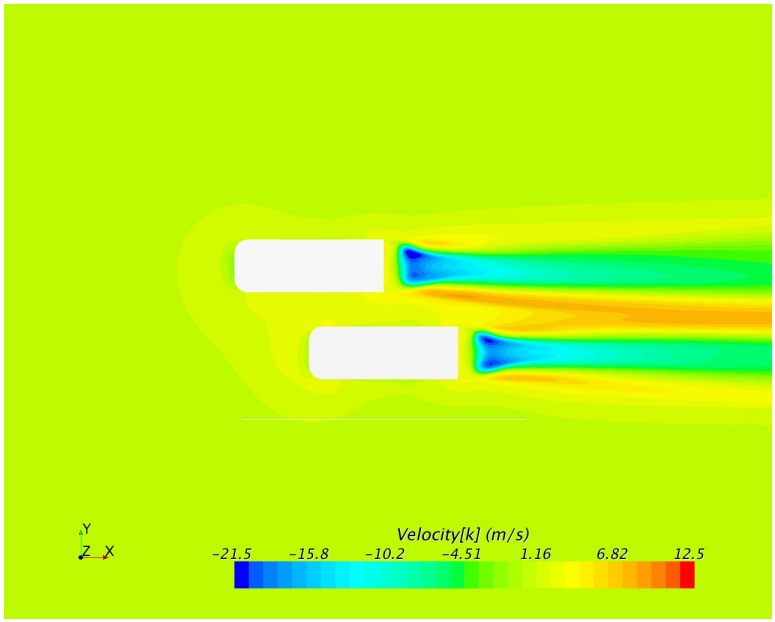

Figure 81: V_z across the mid-plane of both bodies in the Z direction at $X/L = -0.5$

As could be seen in the images at the mid point between the two cars, the overtaking body caused an acceleration of the fluid in the gap as it pulled forward, causing a distinct effect in velocity in the X, Y, and Z directions. This increase in velocity led to the development of the low pressure bubbles clear in figure 86. This change in

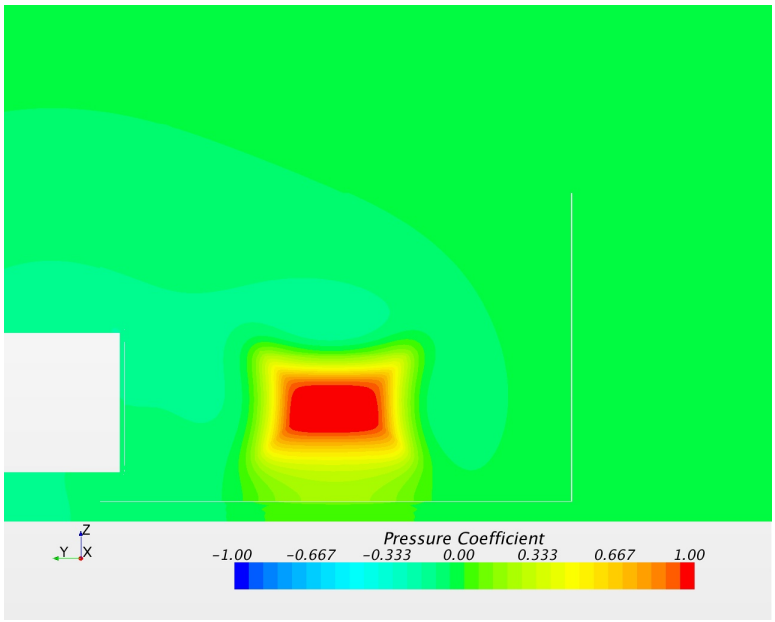

Figure 82: Pressure Coefficient at the middle of the overtaken body in the YZ plane, $X/L = -0.5$. Image shows the Nose of the overtaking body on the right side

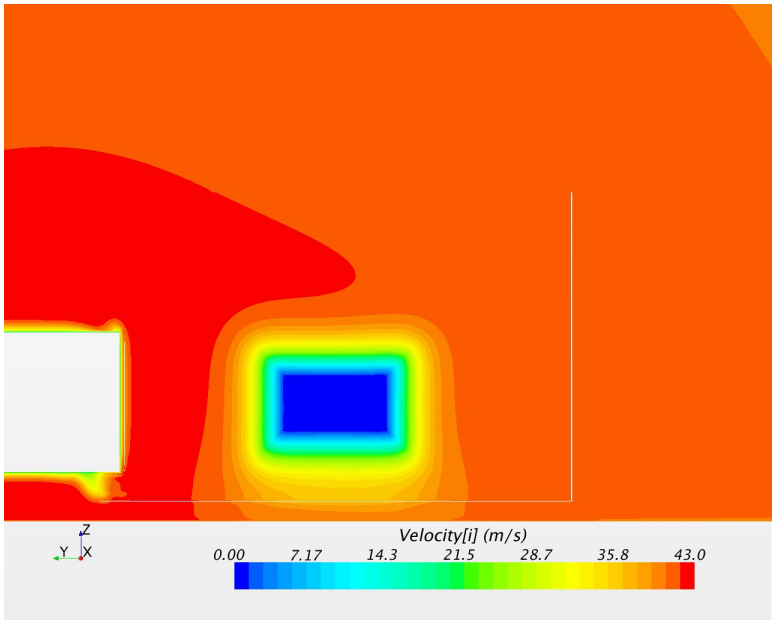

Figure 83: V_x at the middle of the overtaken body in the YZ plane, $X/L = -0.5$. Image shows the Nose of the overtaking body on the right side

velocity and pressure resulted in a peak for the yawing moment of the lead car. At this point, when the nose of the overtaking body was in line with the middle of the overtaken body, the yawing moment of the overtaken body reached it's maximum

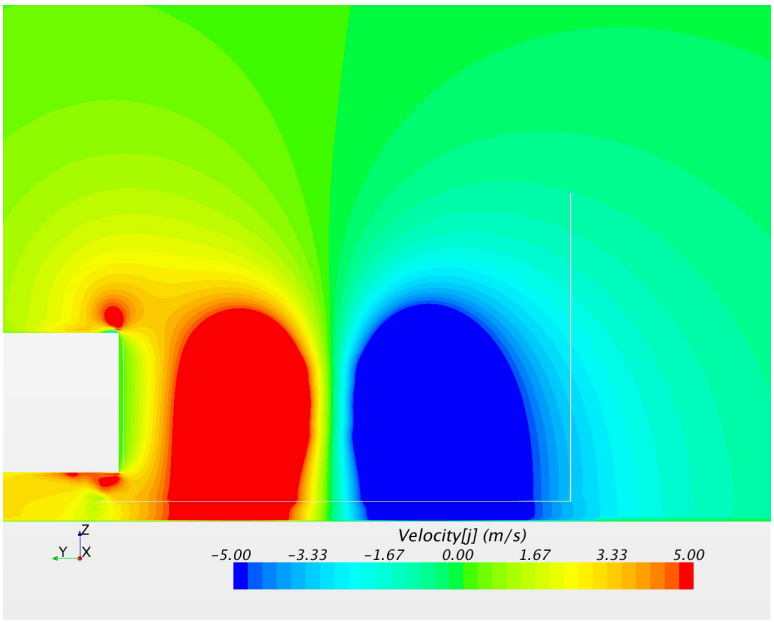

Figure 84: V_y at the middle of the overtaken body in the YZ plane, $X/L = -0.5$. Image shows the Nose of the overtaking body on the right side

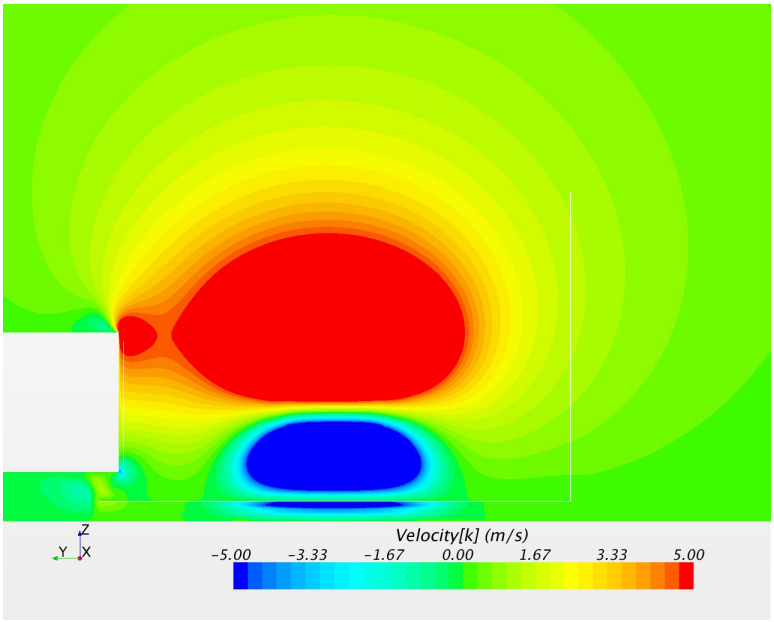

Figure 85: V_z at the middle of the overtaken body in the YZ plane, $X/L = -0.5$. Image shows the Nose of the overtaking body on the right side

positive value. As the high pressure region began to move further forward, beginning to push against the front half of the overtaken body as opposed to the rear half, the yawing moment changed direction and began to decrease. This change in position

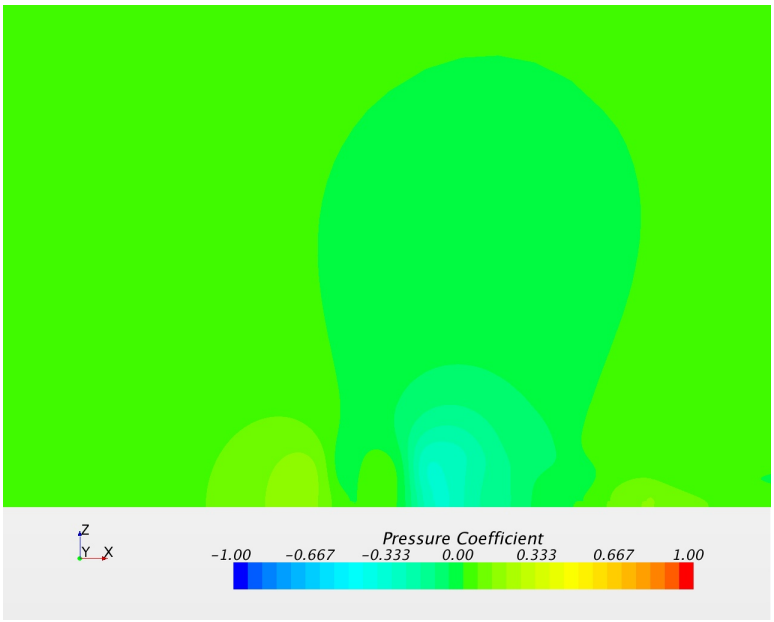

Figure 86: Pressure Coefficient in the XZ plane at the mid plane between the two bodies, $X/L = -0.5$.

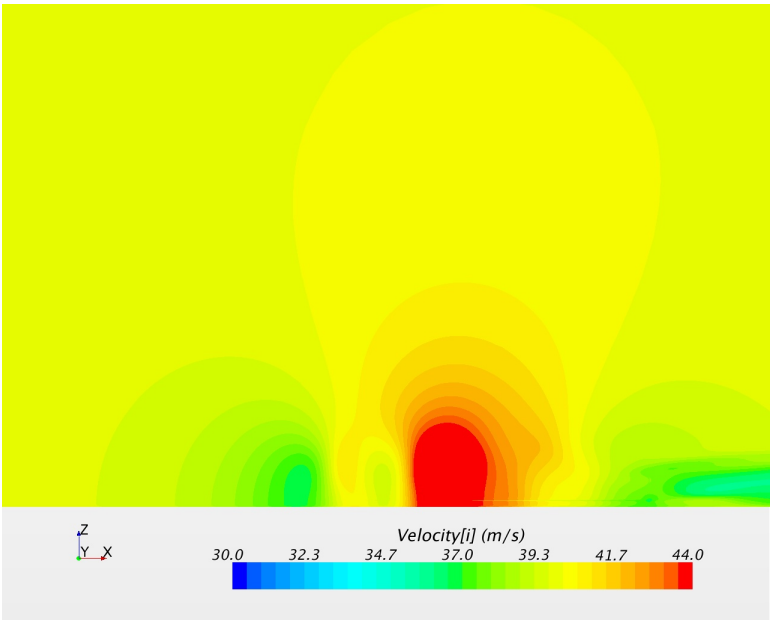

Figure 87: V_x in the XZ plane at the mid plane between the two bodies, $X/L = -0.5$.

of the high pressure region also began to effect the drag coefficients of both bodies. Beyond $-0.5L$, the drag coefficient of the overtaking body began to increase as its high pressure region began to interact with the overtaken bodies own high pressure

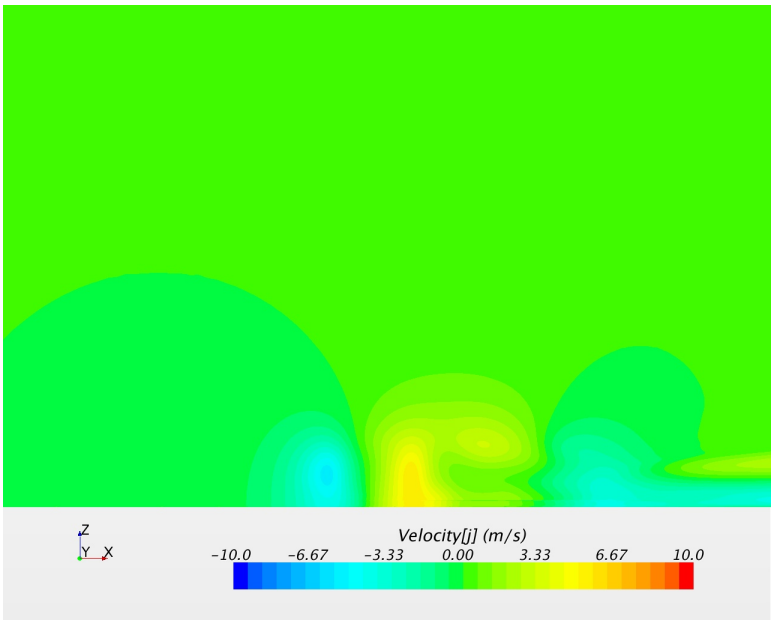

Figure 88: V_y in the XZ plane at the mid plane between the two bodies, $X/L = -0.5$.

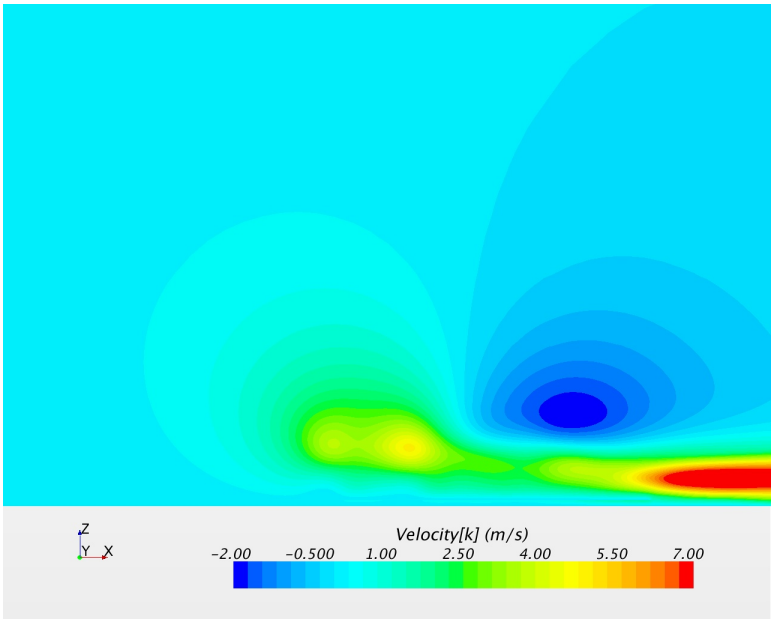

Figure 89: V_z in the XZ plane at the mid plane between the two bodies, $X/L = -0.5$.

region. This corresponded to a a drop in the drag coefficient of the overtaken body. It was also at approximately this point that the side force coefficients of both bodies became equal, but were trending in opposite directions.

The changes in the side force coefficient corresponded to changes in the yawing

moment for the overtaken body, which experienced a maximum value of yaw at $X/L = -0.5$. Beyond this point the high pressure region of the overtaking body, which was inducing this yawing moment on the overtaken body, began to act on the front half of the body instead of the rear, changing the direction of the moment. These trends continued until the two bodies were side-by side.

Once the two bodies were side-by-side some very interesting effects became clear. At this point the drag coefficients of both bodies were equal, but interestingly the drag coefficient of either body was slightly higher than that of a single body in isolation. A clue to the reason for this could first be seen in the plot for side force coefficient (Figure 37) When the two bodies were side by side, the side force coefficient of both bodies reached their respective peak values. The magnitudes of these two values was almost the same, with the overtaking body exerting a slightly larger side force on the overtaken body in terms of magnitude due to its higher velocity. It was also interesting to note that since side force was defined as positive in the positive Y direction, the two bodies were essentially pushing against each other at this point.

Once again, to better understand the causes of these trends, the pressure and velocity scenes were investigated.

Figure 90 brought some clarity to the causes of these effects. As the two bodies were side-by-side, the high pressure regions generated at the front of both bodies interacted considerably, forming effectively one large high-pressure bubble at the front of both bodies. Similarly, in the wake of both bodies, a larger low-pressure region was generated. These large changes in pressure, considerably higher than for a single body in isolation, resulted in an increase in drag value for each body form one in

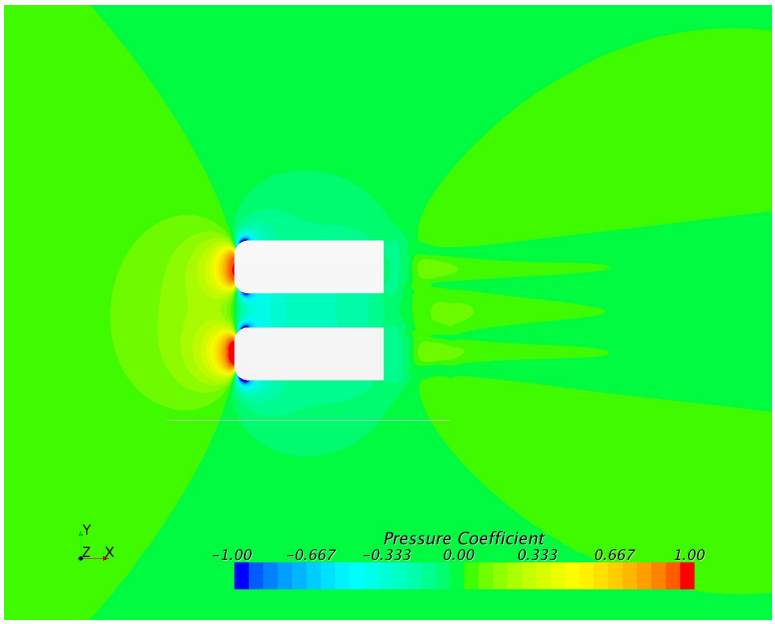

Figure 90: Pressure coefficient across the mid-plane of both bodies in the Z direction at $X/L = 0$

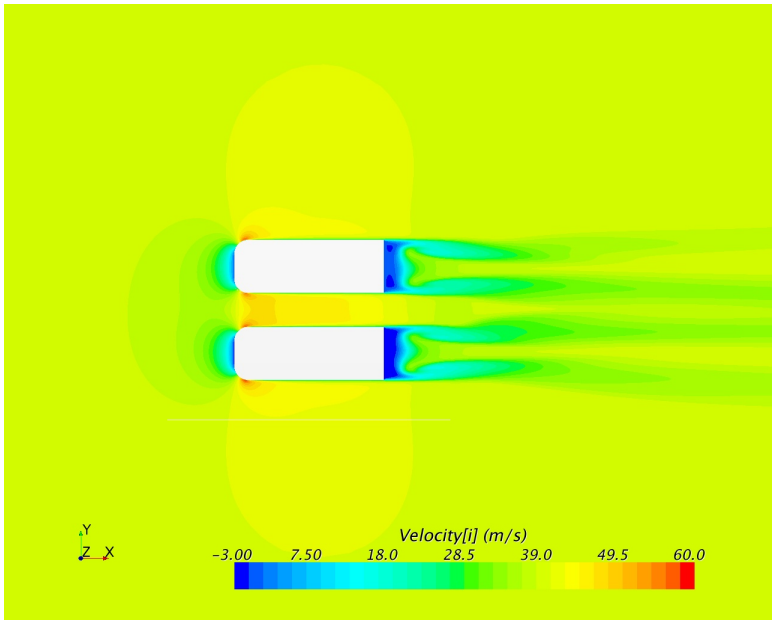

Figure 91: V_x across the mid-plane of both bodies in the Z direction at $X/L = 0$

isolation.

Analysis of the velocity fields provided further information. The two bodies being side-by-side slowed the velocity of air at the front of the two bodies, funneling it into

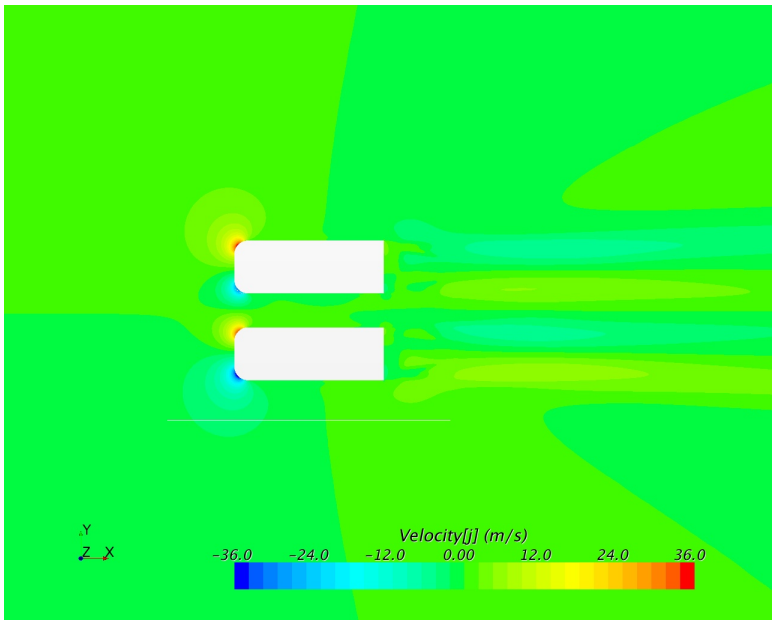

Figure 92: V_y across the mid-plane of both bodies in the Z direction at $X/L = 0$

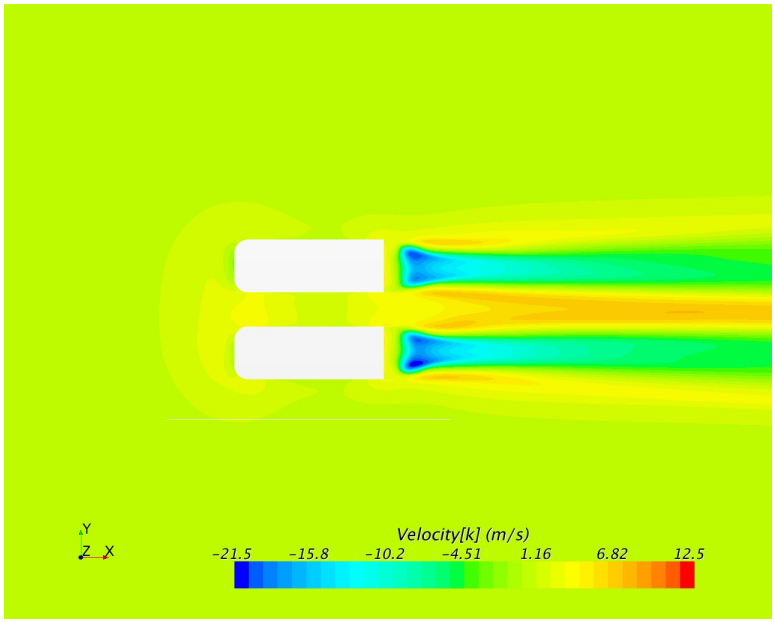

Figure 93: V_z across the mid-plane of both bodies in the Z direction at $X/L = 0$

the gap between them. This situation created a partial Bernoulli effect similar to the one reported by Corin et al. [4], accelerating the flow in the gap between the two bodies, as can be seen in figures 91 to 93. Since Corin's study was conducted in 2D, the effect in that situation was far more noticeable there than it was in these

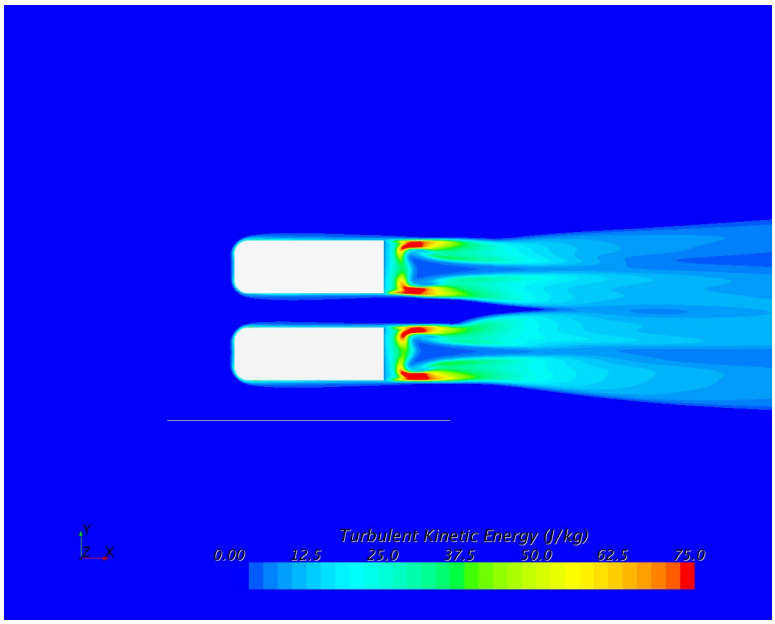

Figure 94: Turbulent Kinetic Energy across the mid-plane of both bodies in the Z direction at $X/L = 0$

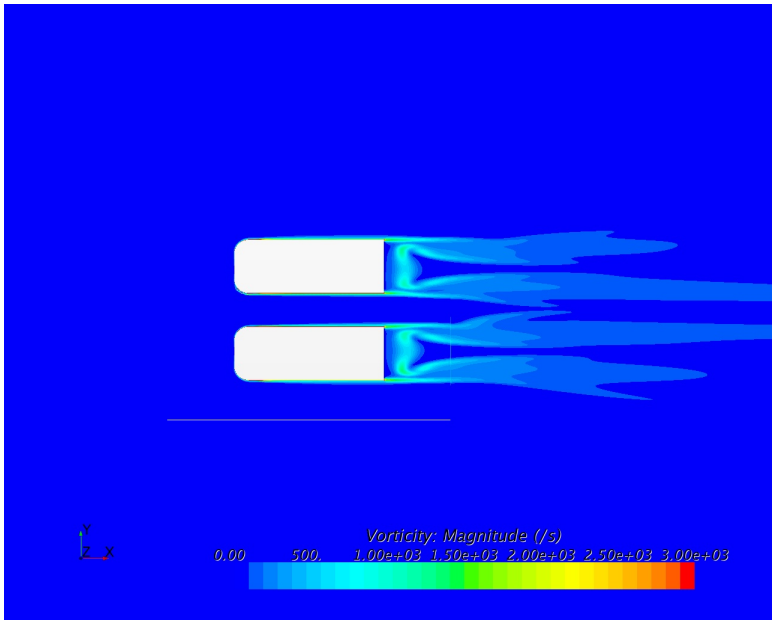

Figure 95: Vorticity across the mid-plane of both bodies in the Z direction at $X/L = 0$

results. This was due to the air not being restricted to the 2D plane, and being able to accelerate in the Z direction as well. Still, from figure 91 there was a clear acceleration of the fluid in this gap between the two bodies, resulting in a low pressure region in

this gap. This low pressure region explained the peaks noted in side force for both bodies at this point, as they were effectively pushing against each other.

The wake structures also provided interesting information. From figure 90, it became clear that similarly to the high pressure regions at the front of the vehicles, the low pressure wakes were also interacting with each other to a significant degree. This effect was seen most clearly in the image of Vz (figure 93), where the velocity fields of both the vehicle bodies caused a significant change in the Z direction from before, accelerating the flow in the region behind the gap between the two bodies. This change in velocity contributed largely to changes occurring in drag coefficient for both vehicles, and goes a long way to explaining why the drag coefficients of these two bodies in tandem was significantly higher than of any one single body in isolation.

Another interesting factor from these scenes was the symmetry of the flow fields around both bodies. In each of the images at this point, the flow patters appeared almost perfectly symmetric about the middle of the gap between the two bodies. The relatively higher velocity of the overtaking body at this point accounts for any of the discrepancies in this symmetry, of which there were very few. This symmetry also accounts for the effects on side force for both vehicle bodies, as well as the yawing moment of the overtaken body. As mentioned before, at this point the side forces exerted on both vehicles were almost equal and opposite in value, while the yawing moment of the overtaken body was 0. To further understand these effects, the scenes at this gap were once again examined.

The plot for pressure coefficient (figure 96) highlighted the low pressure region generated between the two bodies as they were side-by-side, a factor which was confirmed

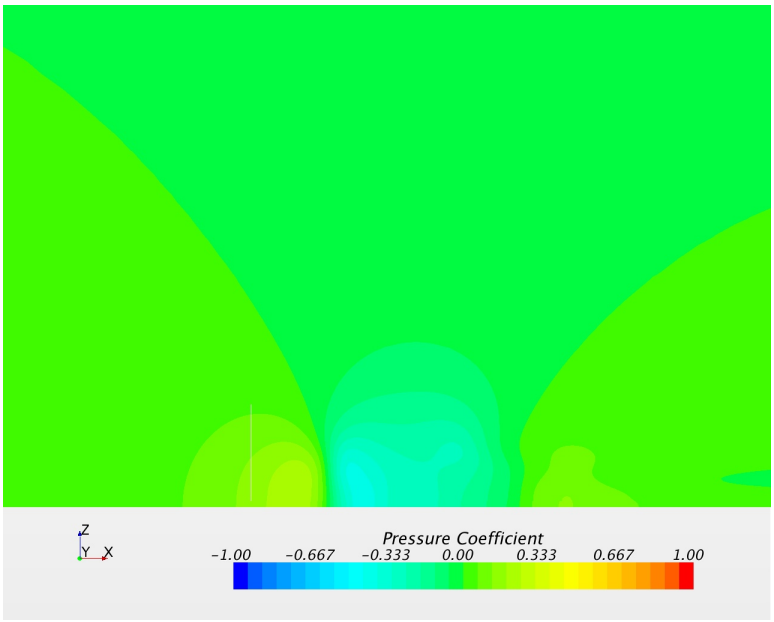

Figure 96: Pressure Coefficient in the XZ plane at the mid plane between the two bodies, $X/L = 0$.

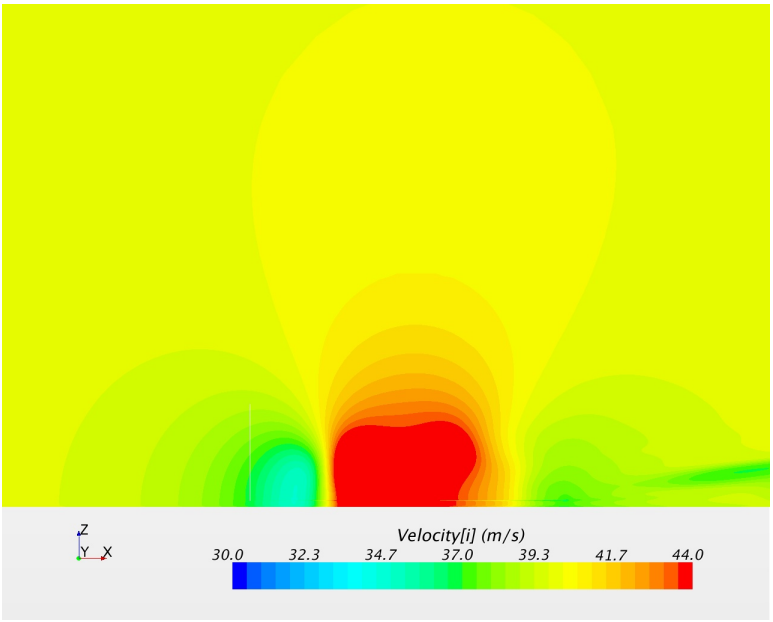

Figure 97: V_x in the XZ plane at the mid plane between the two bodies, $X/L = 0$.

by the large increase in velocity in the X direction as seen in figure 97. Another interesting point to note was the very small change in V_y as evidenced by figure 98, which showed only a small magnitude of V_y at this point. This was due to the velocities

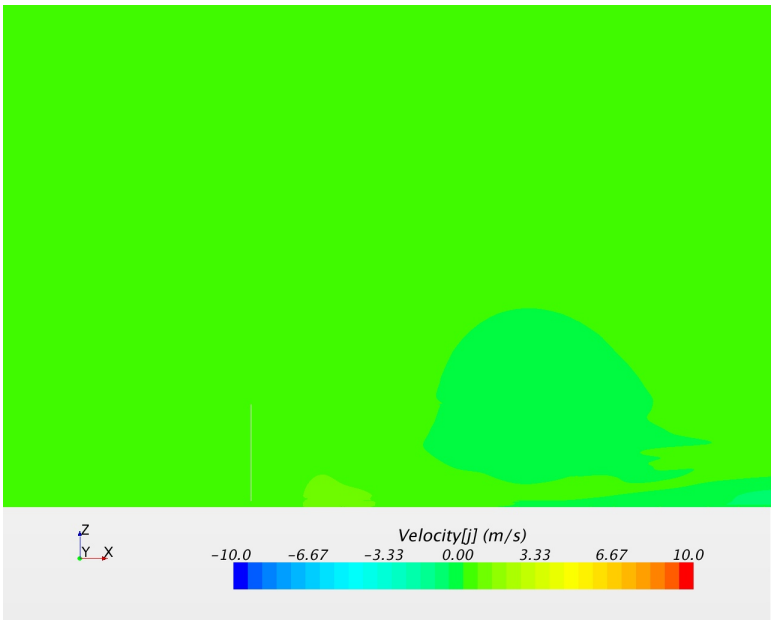

Figure 98: V_y in the XZ plane at the mid plane between the two bodies, $X/L = 0$.

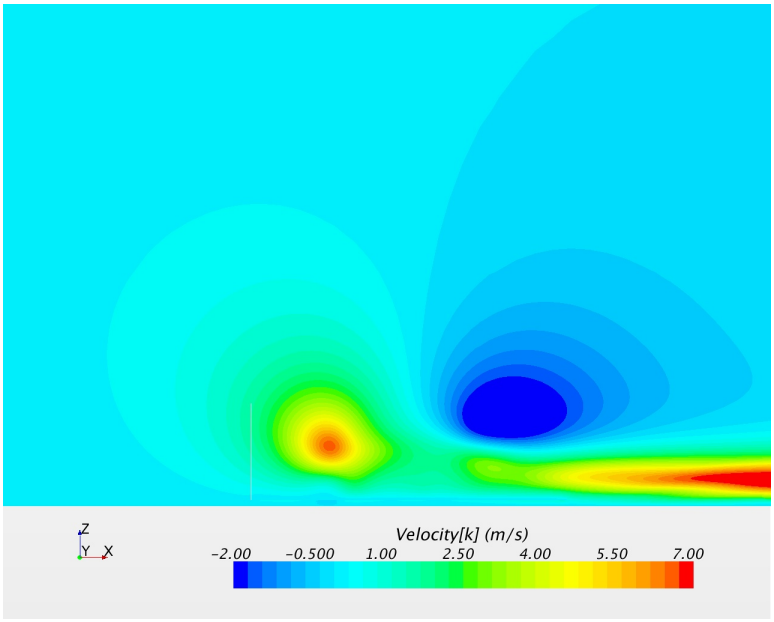

Figure 99: V_z in the XZ plane at the mid plane between the two bodies, $X/L = 0$.

of both bodies effectively canceling each other out in this plane, and resulted in the yawing moment of the overtaken body being 0 at this point. It also accounted for the side force coefficients at this point being equal, but opposite in nature. This negation of V_y also helped to understand the significant increase in velocity in both the X and

Z directions (figures 97 and 99, respectively). With the flow from both bodies pushing against each other, the fluid was forced to accelerate in both these directions.

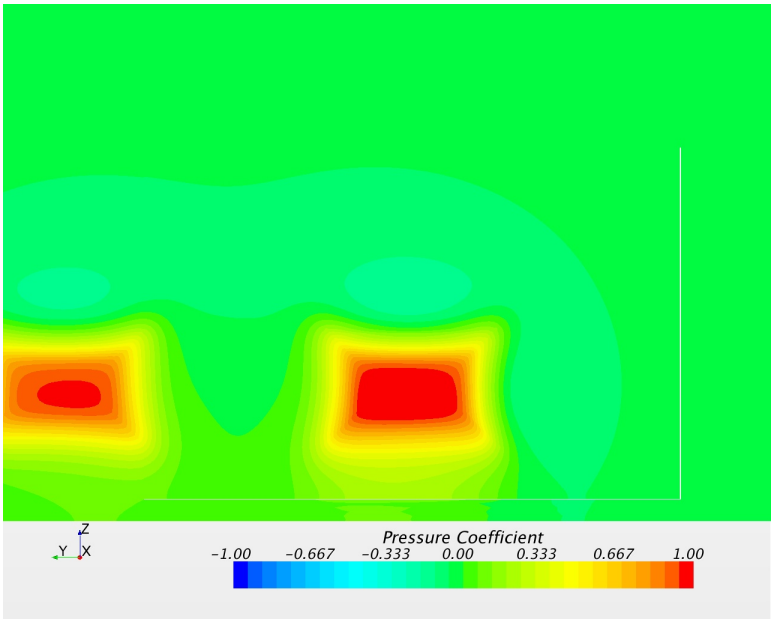

Figure 100: Pressure Coefficient in the YZ plane at the front of the two bodies, $X/L = 0$.

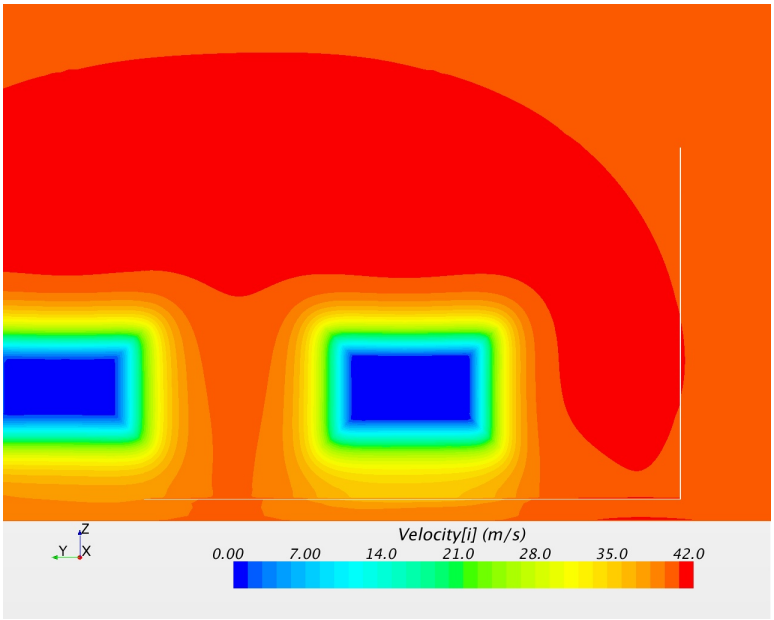

Figure 101: V_x in the YZ plane at the front of the two bodies, $X/L = 0$.

To further understand the effects occurring at this point scenes at the front of the

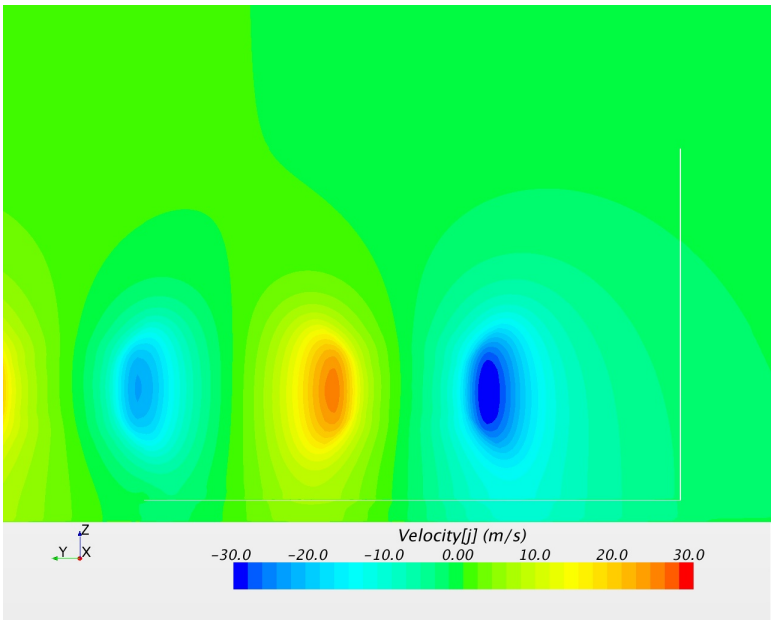

Figure 102: V_y in the YZ plane at the front of the two bodies, $X/L = 0$.

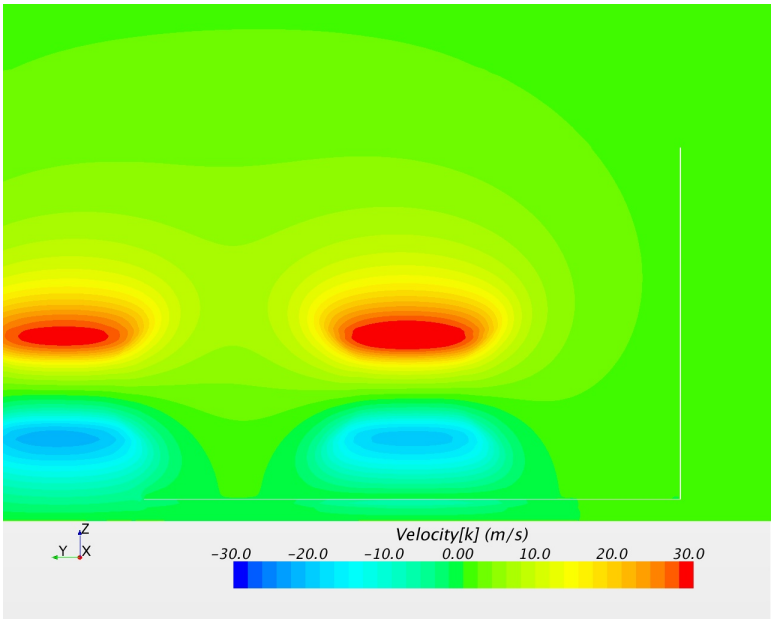

Figure 103: V_z in the YZ plane at the front the two bodies, $X/L = 0$.

two bodies were also investigated. From the scene of pressure coefficient (figure 100), the first thing to notice was that the C_p at the front of the overtaking body (the body on the right in all the images) appeared to be higher than that of the overtaken body. This was due to the field functions for the pressure coefficient being defined by the

universal free stream velocity, and not accounting for the increase in velocity caused by the relative motion of the overtaking body. This was expected when running the simulation, but no computationally viable solution could be found. In all the velocity scenes (figures 101 to 103), however, it was clear that the flow patterns were perfectly symmetrical about the gap between the two bodies, with the magnitude for the overtaking body being slightly higher in all cases as a result of its higher relative velocity.

Once again a clear symmetry was noted between the two bodies in all the scenes generated, which served to confirm the trends in the various aerodynamic coefficients for both bodies.

With the two bodies now exchanging position, and the overtaking body now pulling ahead of the overtaken body, the trends seen up until this point began to reverse. A brief analysis was conducted from this point forward, to help further understand the changes occurring.

4.8 X/L from 0 to 1.5

As the two bodies were side-by-side, their drag coefficients were equal, with that of the overtaken body trending in the negative direction, while that of the overtaking body was on the rise. These trends continued as the overtaking body pulled ahead of the overtaken body. The drag coefficient of the overtaken body reached its minimum value when the overtaking body was at $0.5L$ ahead of it. At this same point the drag coefficient of the overtaking body also appeared to reach a peak in its value, mirroring what happened when the positions of the two bodies were interchanged.

It was also at this point that the yawing moment coefficient of the overtaken body reached a peak, once again mirroring the result from when the overtaking body was at $-0.5L$. It could be inferred from this data that similar effects were occurring as before, however to ensure that this was the case the scenes at this position were once again investigated.

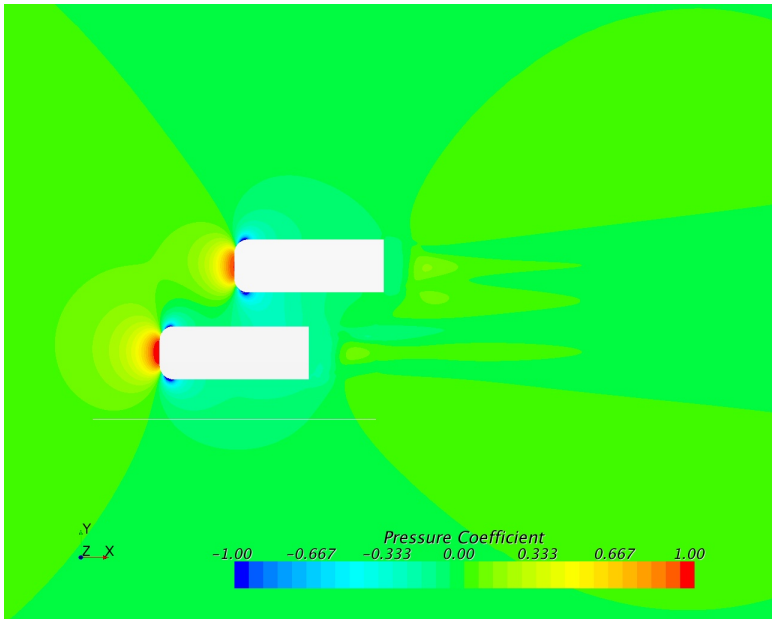

Figure 104: Pressure coefficient across the mid-plane of both bodies in the Z direction at $X/L = 0.5$

From the image of pressure coefficient at $X/L = 0.5$ (figure 104), it could be seen that the high pressure regions at the front of each vehicle were still interacting with one another to some extent, while the low pressure region along the side of the overtaking body passed directly alongside the front of the overtaken vehicle. This difference in pressure accounted for the effects seen on the yawing moment of the overtaken body, causing it to reach a peak. The presence of this region was confirmed in the image of V_x (figure 105), where a bubble of higher velocity fluid could be seen passing in between the two bodies. In addition, the velocity in the wake of the overtaking body

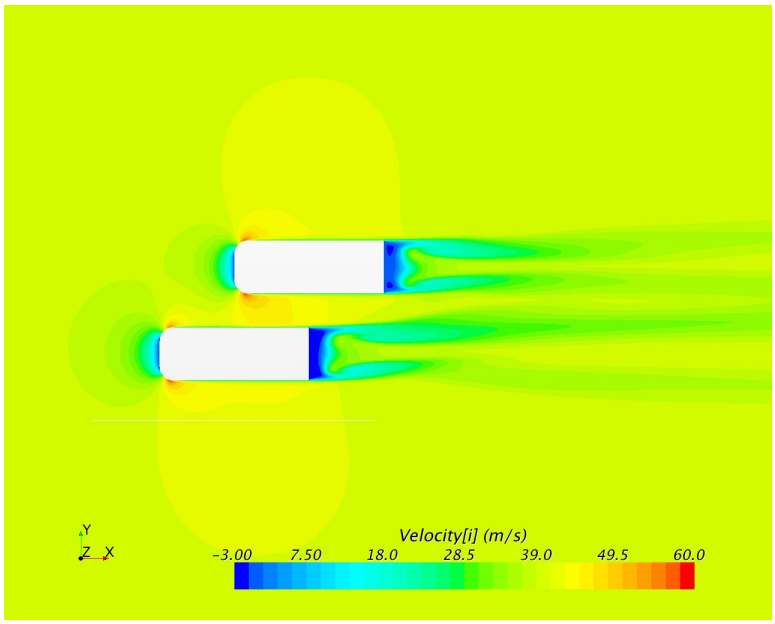

Figure 105: V_x across the mid-plane of both bodies in the Z direction at $X/L = 0.5$

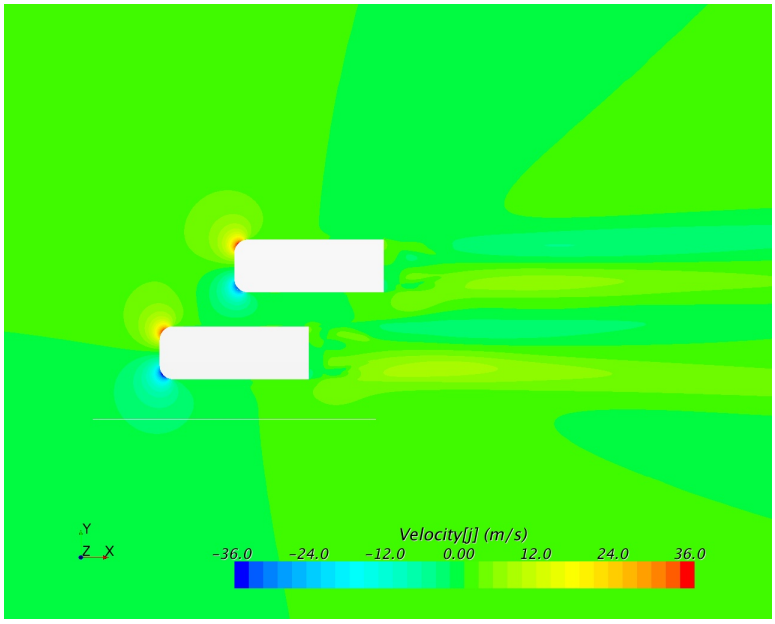

Figure 106: V_y across the mid-plane of both bodies in the Z direction at $X/L = 0.5$

could be seen to be affected by the presence of the overtaken body, becoming slightly higher on the side of the overtaking body away from the overtaken body. This was likely the result of the vortex shedding structure behind the two bodies, as could be seen in figure 108. In addition, there was a much clearer interaction of these wake

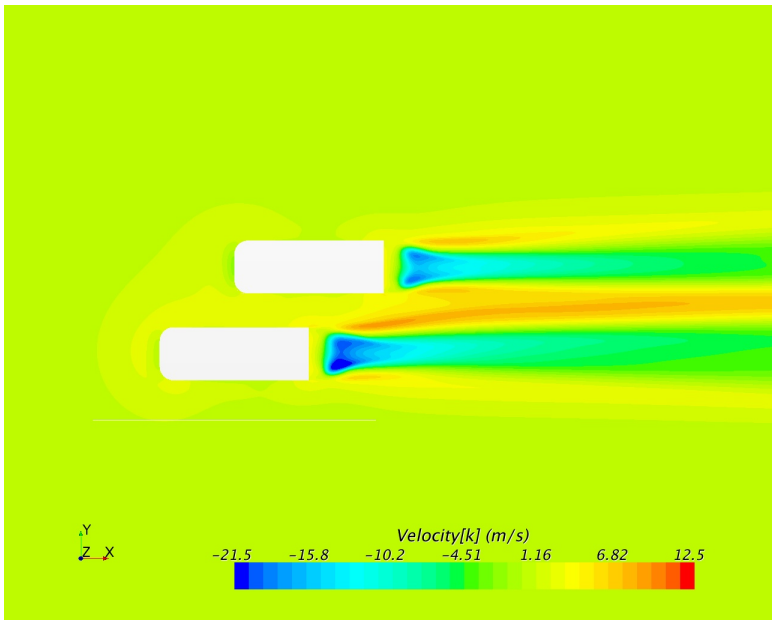

Figure 107: V_z across the mid-plane of both bodies in the Z direction at $X/L = 0.5$

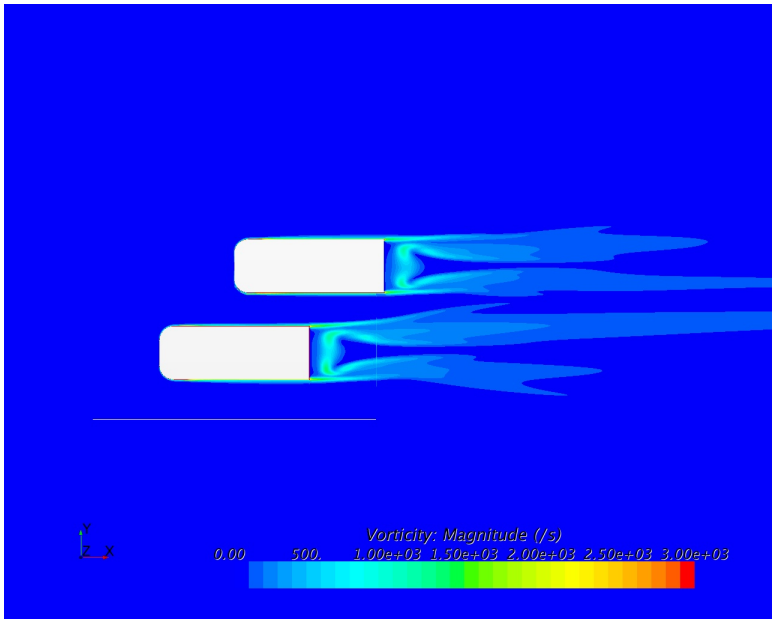

Figure 108: Vorticity across the mid-plane of both bodies in the Z direction at $X/L = 0.5$

regions in figure 107, which showed the the velocity in the Z direction. The overtaking body generated a a significantly higher velocity in the Z direction in it's wake on the side that was closer to the overtaking body, indicating the interaction between the

vortices behind both bodies.

The vortex structure at $X/L = 0.5$ (figure 108) was very different to that at $X/L = 0$ (figure 95), indicating the effect of the relative positions the two bodies had on each other, and going some way to explain the changes occurring between the two bodies as they passed. As the bodies were at $X/L = 0.5$, the vortices on the far side of the overtaking body were considerably smaller than those on the side closer to the overtaken body. In addition, there were higher frequency vortices in the wake of the overtaking body that extended further behind the overtaking body than before.

Between $X/L = 0.5$ and $X/L = 1$ an interesting trend was noted in the plot of drag coefficient. The drag coefficient of the overtaken body had reached a minimum at $X/L = -0.5$, and began to rise significantly beyond this point. For the overtaking body, however, the drag coefficient continued to rise slowly, reaching a peak when the tail of the overtaking body was in line with the nose of the overtaken body at $X/L = 1$. This result mirrors the results from $X/L = -1to - 0.5$, as expected, with the trends of the two bodies being switched.

At $X/L = 1$ the two bodies had resumed behaving as vehicles in convoy, with the wake from the overtaking body now being influenced by the presence of the overtaken body. The suppression of the wake of the overtaking body by the front of the overtaken body caused the drag coefficient of of the overtaking body to decrease. This subsequently also led to an increase in the drag coefficient for the overtaken body due to the increase in pressure at the front of the body.

It was also at this point, wherein the bodies were oriented nose to tail with the overtaking body in front of the overtaken body, that the side force coefficient of the

overtaking body reached a universal peak. This was once again due to the presence of the high pressure region of the overtaken body at the tail of the overtaking body, exerting a significant amount of force against the body and causing it to rotate.

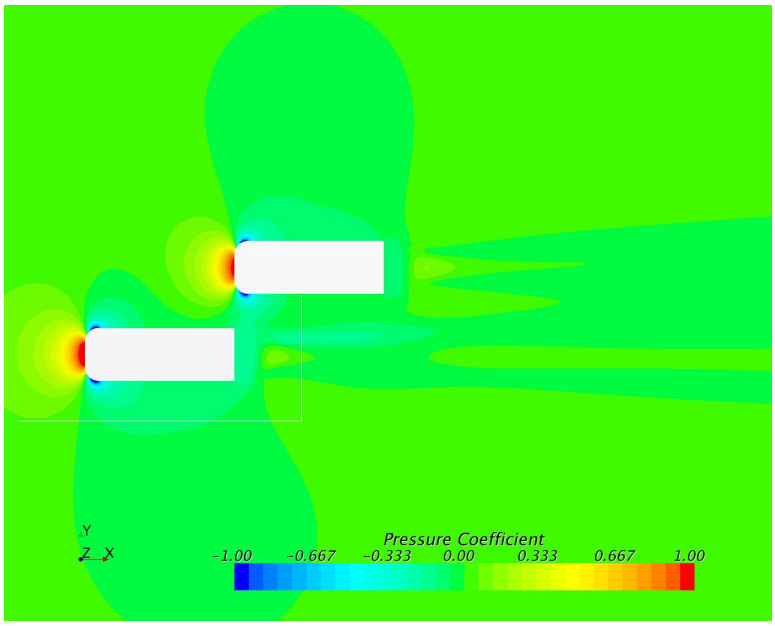

Figure 109: Pressure coefficient across the mid-plane of both bodies in the Z direction at $X/L = 1$

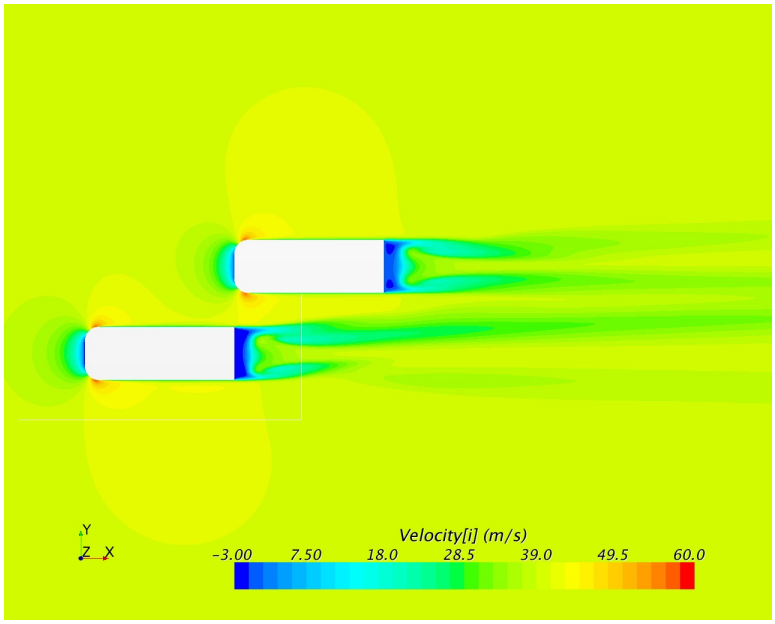

Figure 110: V_x across the mid-plane of both bodies in the Z direction at $X/L = 1$

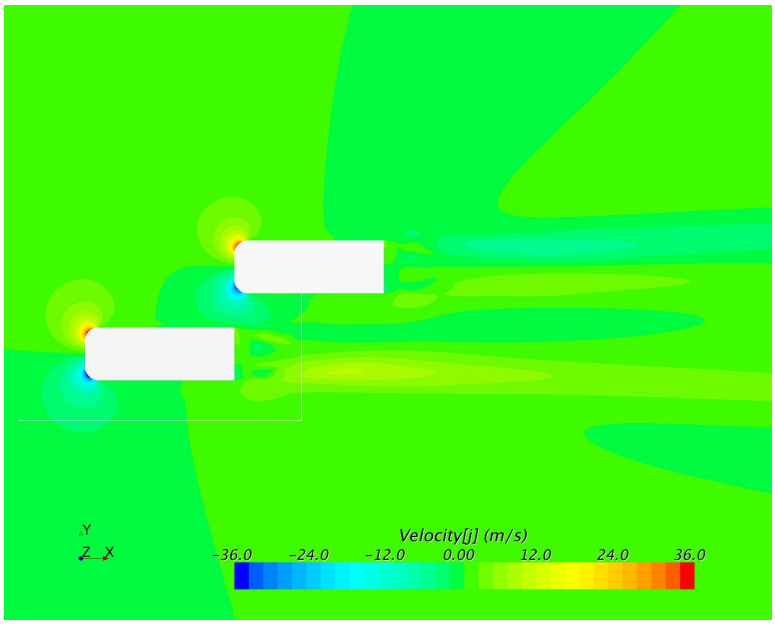

Figure 111: V_y across the mid-plane of both bodies in the Z direction at $X/L = 1$

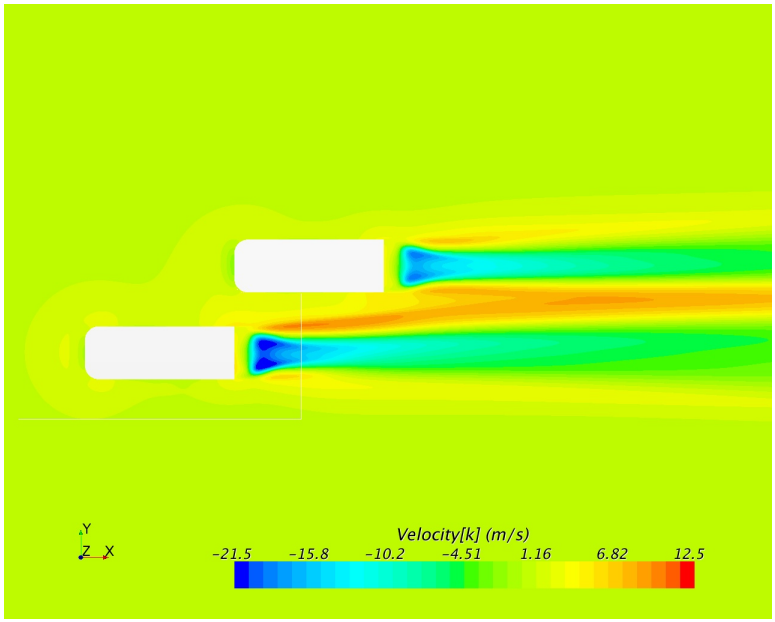

Figure 112: V_z across the mid-plane of both bodies in the Z direction at $X/L = 1$

Once again it could be seen from the figures that the wake structure of the overtaking body was significantly influenced by the presence of the overtaken body directly in its wake. This influence was demonstrated in each of the velocity profiles generated, showing the wake in the trail of the overtaking body. The velocity in the

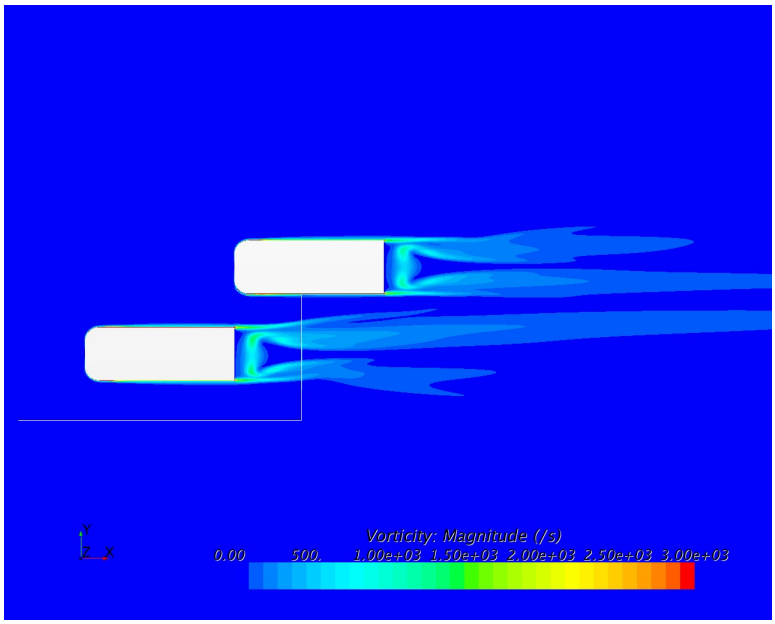

Figure 113: Vorticity across the mid-plane of both bodies in the Z direction at $X/L = 1$

Z direction was accelerated significantly in the gap between the two bodies, caused by the interaction of the vortices off the rear of the overtaking vehicle and the low pressure region along the side of the overtaken body. In the X and Y directions a different effect was noticed, wherein the flow off the rear of the overtaking body on the side away from the overtaken body was accelerated, while the flow on the inside was slowed down significantly. The effect of this positioning on the vortices at the rear of the overtaking vehicle showed a much larger trail of higher frequency vortices than had been present before, further highlighting the effect the overtaken body had on the wake of the overtaking body. This increase in vorticity and velocity at the rear of the vehicle helped to explain the peak in side force coefficient for the overtaking vehicle at this point.

As the overtaking body advanced to $1.5L$, the side force coefficients for both bodies began returning to their neutral values. At $1.5L$, the drag force coefficient of both

bodies once again became equal, while the yawing moment of the overtaken body returned to its original value. These results all mirrored the results at $-1.5L$, as was expected. For the overtaking body, the C_D value continued to fall until it was $1.5L$ behind the overtaking body, while that of the overtaken body rose up until this same point.

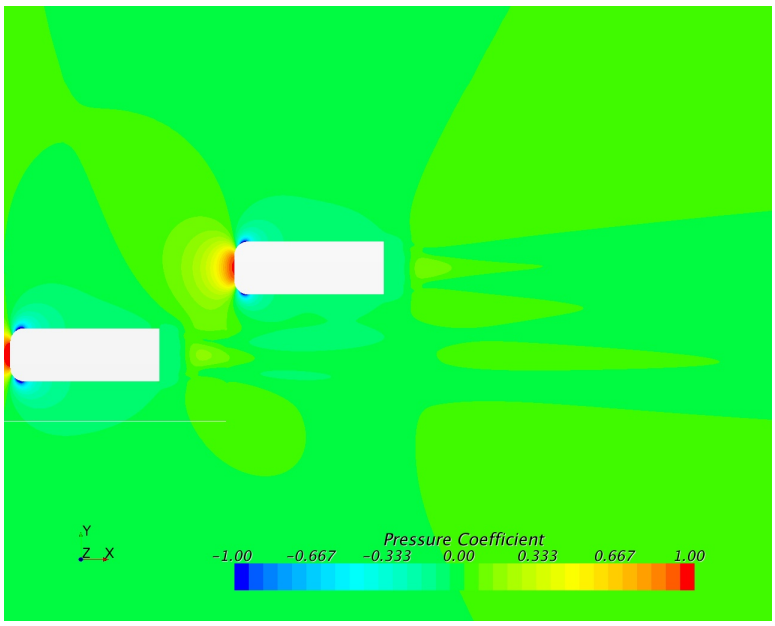

Figure 114: Pressure coefficient across the mid-plane of both bodies in the Z direction at $X/L = 1.5$

Upon analyzing the scenes, it could be seen that now the high pressure region at the front of the overtaken body was interacting with the wake of the overtaking body, but no longer with the body itself (figure 114). This explained the reduction in side force coefficient for both bodies, as well as the trends noticed in the drag coefficients of both bodies. Scenes of velocity and vorticity (figures 115 to 118) showed the wake structure at the rear of the overtaking body begin to return to it's original shape, no longer being as influenced by the presence of the overtaken body.

In the figure for V_x at this point (figure 115) the wake suppression of the over-

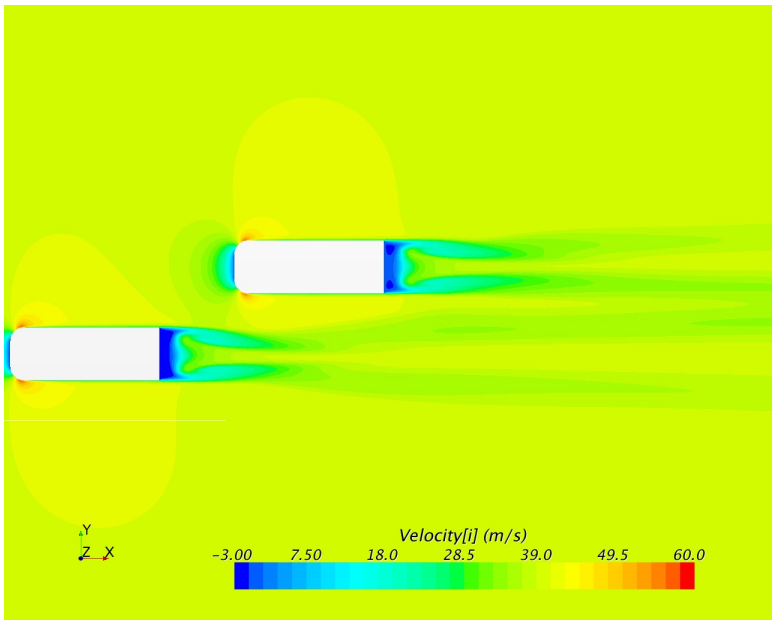

Figure 115: V_x across the mid-plane of both bodies in the Z direction at $X/L = 1.5$

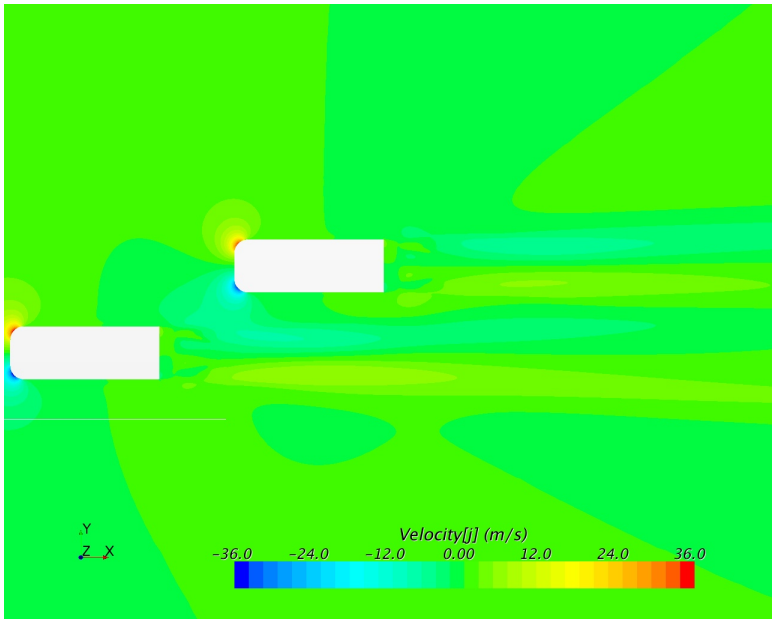

Figure 116: V_y across the mid-plane of both bodies in the Z direction at $X/L = 1.5$

taking body can be seen, and directly compared to the relatively cleaner wake of the overtaken body. The wake of the overtaken body is still slightly affected by the presence of the overtaking body, but significantly less so than before. In addition, the scene of pressure coefficient (figure 114) shows a similar suppression of the wake

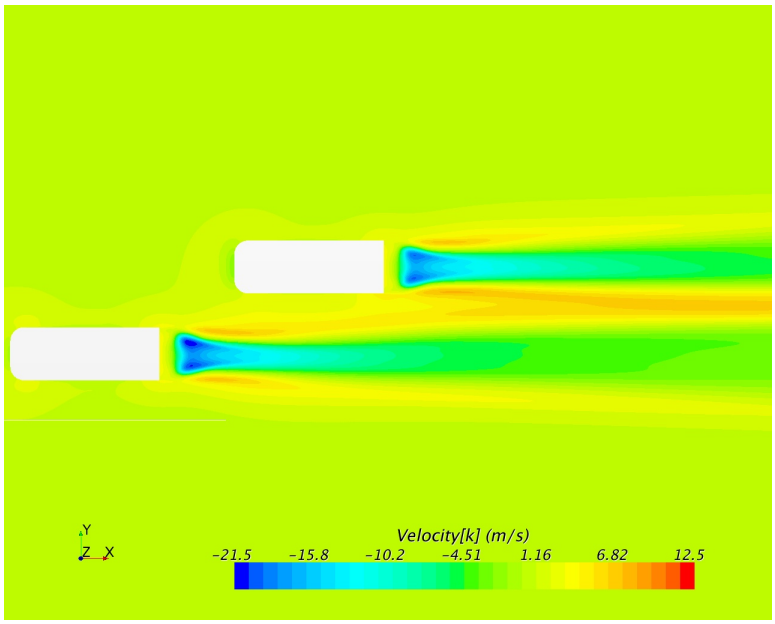

Figure 117: V_z across the mid-plane of both bodies in the Z direction at $X/L = 1.5$

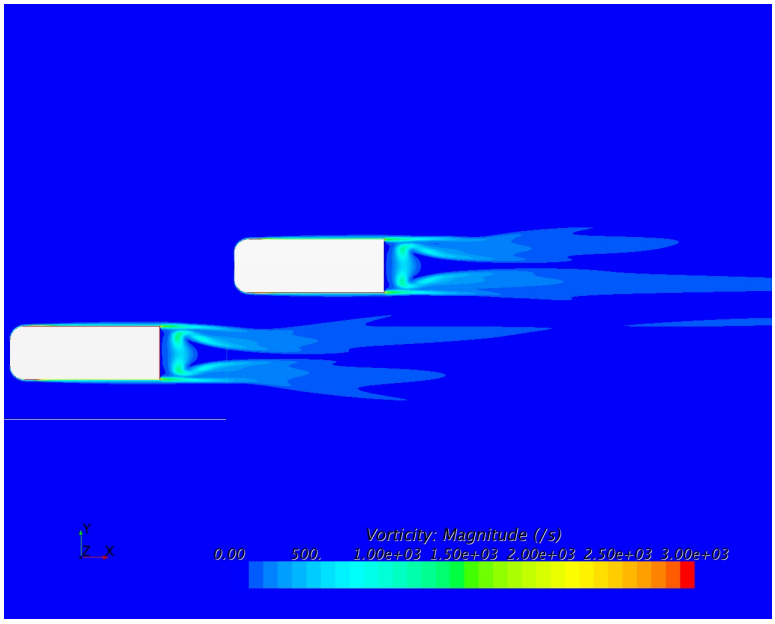

Figure 118: Vorticity across the mid-plane of both bodies in the Z direction at $X/L = 1.5$

for the overtaking body as was observed when the overtaking body was behind the overtaken body.

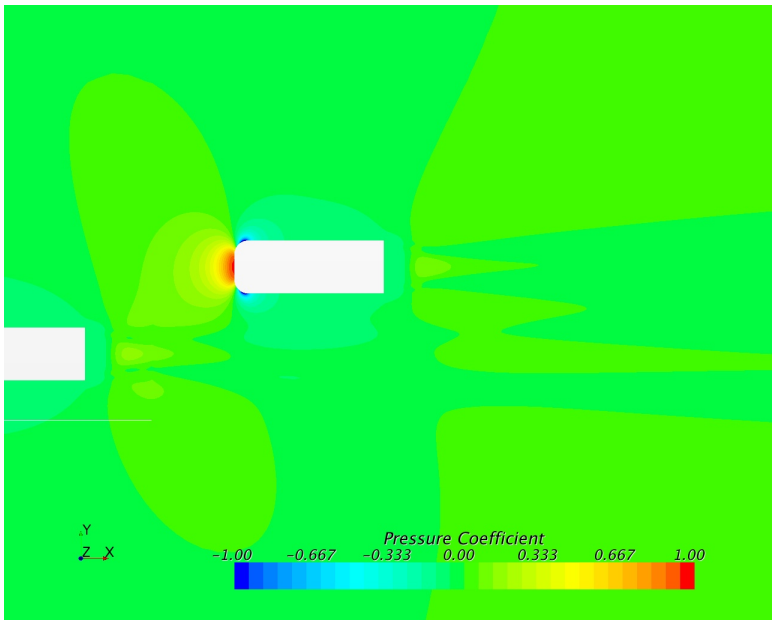

Figure 119: Pressure coefficient across the mid-plane of both bodies in the Z direction at $X/L = 2$

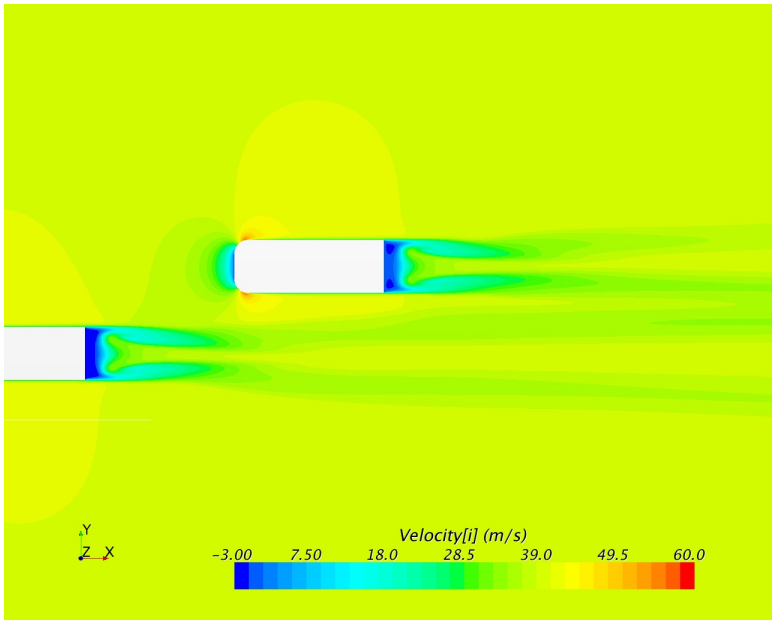

Figure 120: V_x across the mid-plane of both bodies in the Z direction at $X/L = 2$

4.9 X/L from 1.5 to end

For the overtaken body, which now sat in the wake of the overtaking body, there was still a large influence as a result of the overtaking body. As observed earlier, the

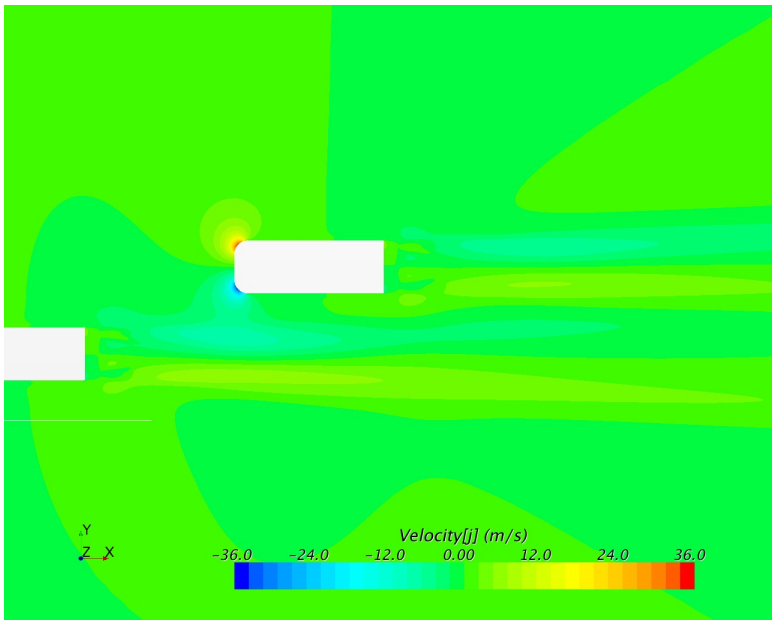

Figure 121: V_y across the mid-plane of both bodies in the Z direction at $X/L = 2$

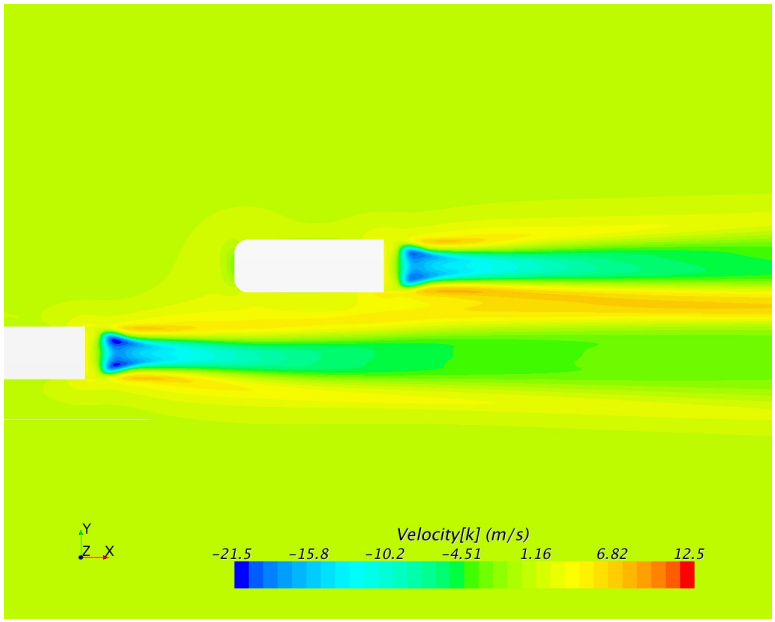

Figure 122: V_z across the mid-plane of both bodies in the Z direction at $X/L = 2$

flow in front of the body beyond this point would no longer be perfectly horizontal, and therefore even when the overtaking body was $2L$ in front of the overtaken body (figures 119 to 123), it's wake structure influenced the flow around the overtaken body.

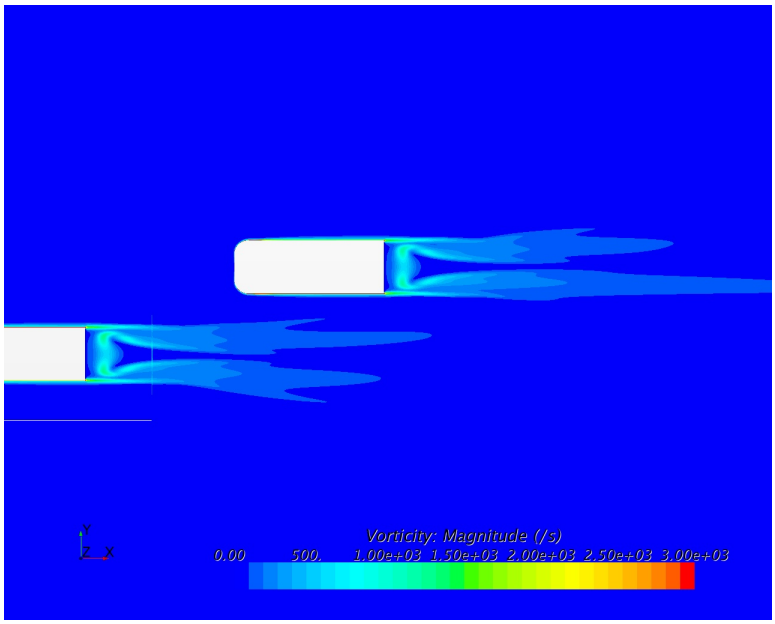

Figure 123: Vorticity across the mid-plane of both bodies in the Z direction at $X/L = 2$

Once again the bodies behaved similar to two bodies traveling in convoy, with the lead body (overtaking body in this case) having a lower drag coefficient than the trailing (overtaking) body. These results once again corresponded very well with the results from the convoy studies conducted. Once again, the impingement of the wake from the rear of the overtaking body on the front of the overtaken body was the major cause for this trend in drag coefficient. This was demonstrated in the images for velocity and pressure at this point of the simulation (figures 119 to 122). The velocity fields in the wake of the overtaken body were affected less than those of the overtaking body, while the pressure and velocity fields at the front of the overtaken body were interacting significantly with the wake of the overtaking body.

Beyond $X/L = 2$, the values for side force coefficient and yawing moment would begin to return to their original values for both bodies. For drag coefficient, however, it was different. Initially, the drag coefficient for the overtaking body had been

higher than that of the overtaken body, due to the change in velocity vectors caused by the overtaken body and the wake impingement of the overtaken body on the overtaking body. Now the roles were reversed, with the wake of the overtaking body influencing the flow around the overtaken body. As a result, the drag coefficient of the overtaking body was now lower than that of the overtaken body, once again mirroring the observations from the beginning of the simulation. These values continued until the end of the simulation, and to highlight the causes for this figures 124 to 128 were generated.

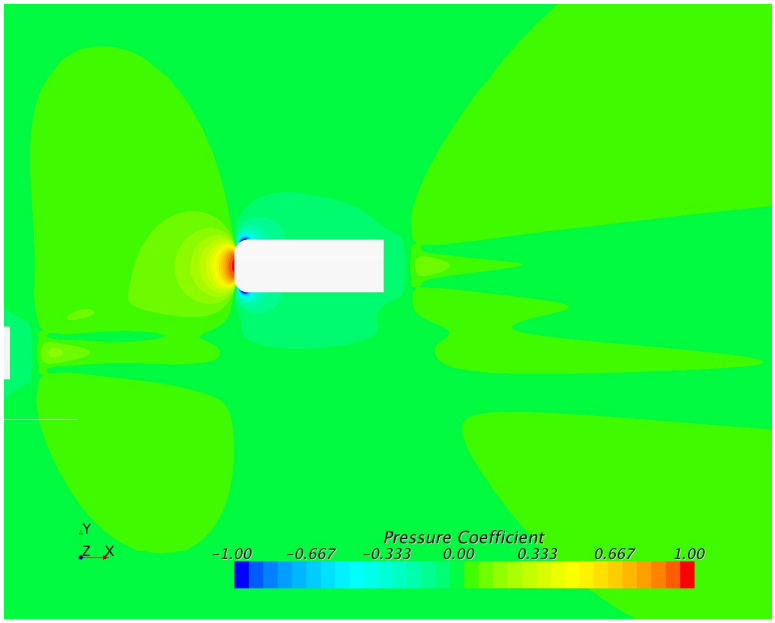

Figure 124: Pressure coefficient across the mid-plane of both bodies in the Z direction at $X/L = 2.5$

As could be seen in the scalar scenes generated, the flow at the rear of the overtaking body had a large influence on the flow around the front of the overtaken body, without being as influenced itself. This flow caused a drastic change in the velocity components around the front of the overtaken body, and explain why the drag coefficient of the overtaken body does not return to its original value. This was in keeping with the

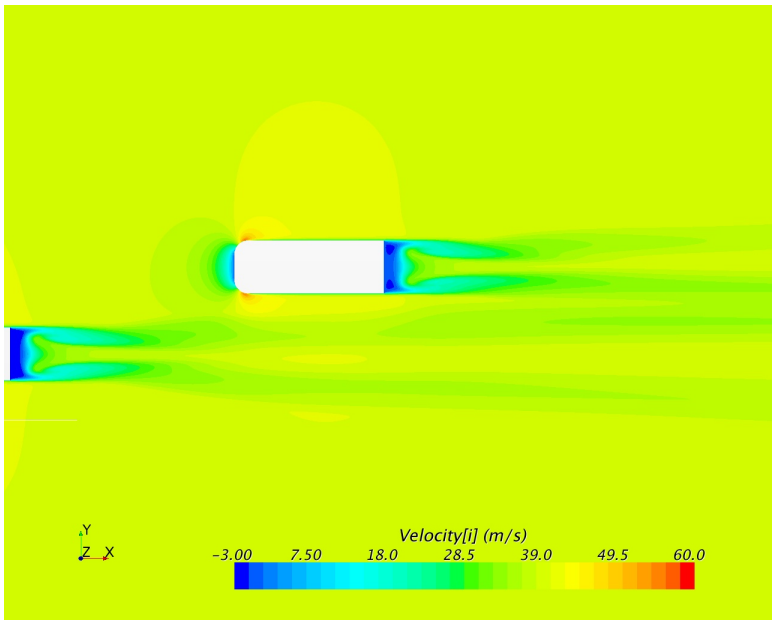

Figure 125: V_x across the mid-plane of both bodies in the Z direction at $X/L = 2.5$

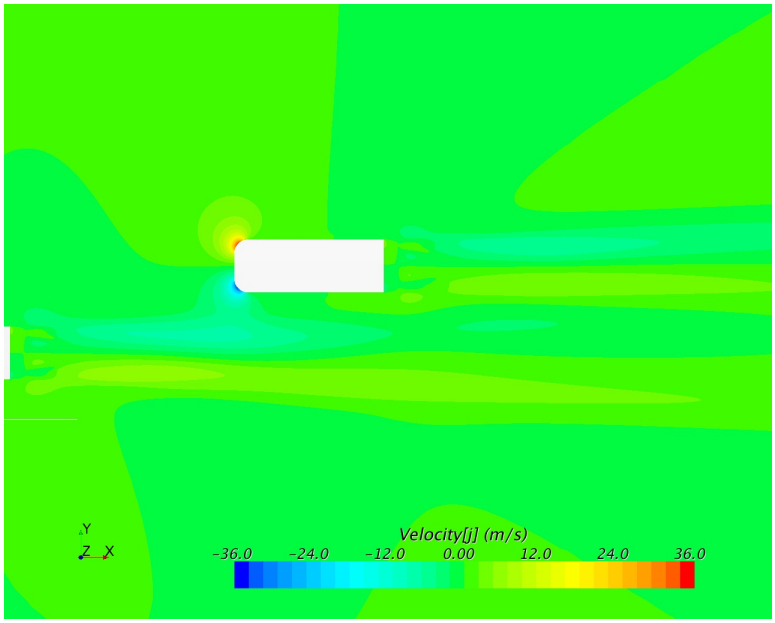

Figure 126: V_y across the mid-plane of both bodies in the Z direction at $X/L = 2.5$

findings of Watts [17], who had demonstrated that the realizable $k - \epsilon$ turbulence model allowed the wake of the lead body to propagate almost infinitely.

This completed the qualitative analysis of the overtaking maneuver. The trends in coefficients observed in the simulation of this maneuver using the overset mesh

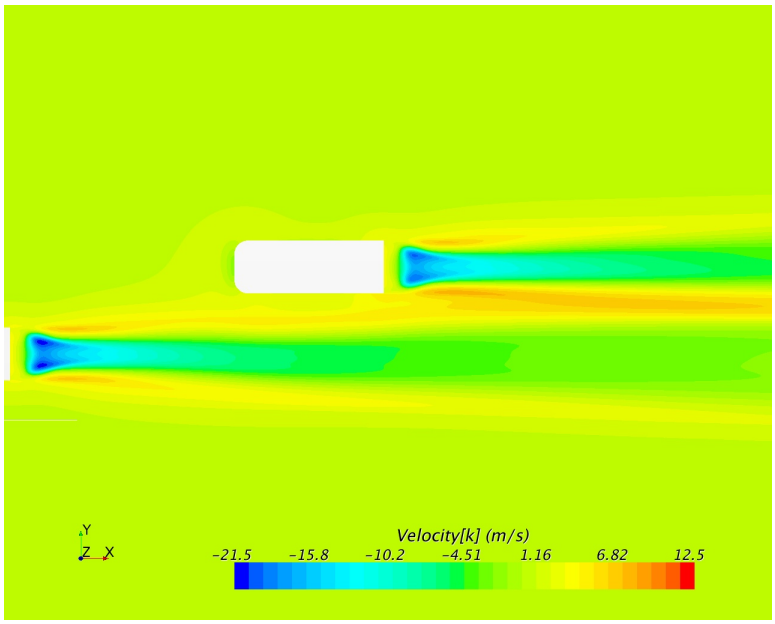

Figure 127: V_z across the mid-plane of both bodies in the Z direction at $X/L = 2.5$

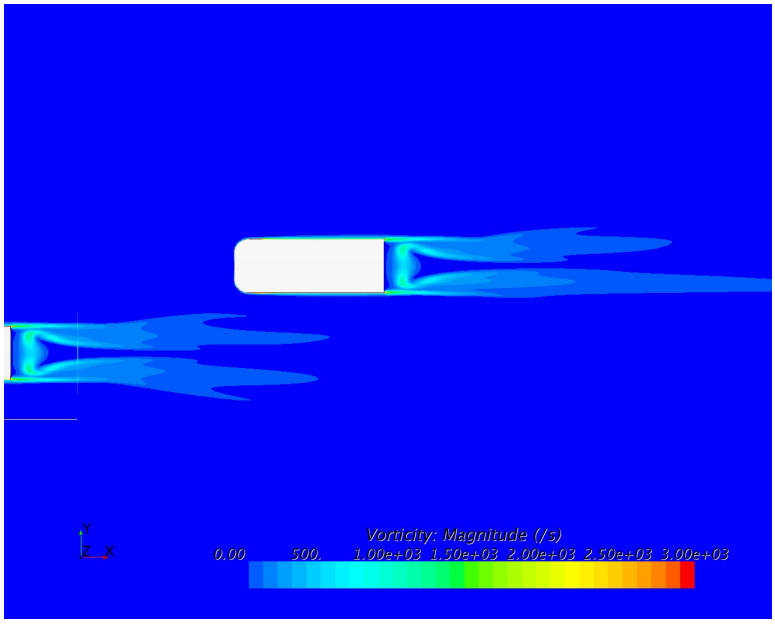

Figure 128: Vorticity across the mid-plane of both bodies in the Z direction at $X/L = 2.5$

matched well with the experimental results presented earlier by Noger et al. [1], and also highlighted several interesting aerodynamic phenomena occurring during the maneuver. In addition, the flow patterns generated by the bodies also corresponded

considerably well with the results from the various studies conducted on the isolated Ahmed body, as well as the studies on multiple Ahmed bodies in convoy. The changes in aerodynamic coefficients for both the bodies were interesting to note, and the simulation provides an excellent springboard for further analysis of the overtaking maneuver with various other factors such as yaw angle and relative velocity taken into consideration.

4.10 Limitations of the Simulation

While the simulation served as an extremely useful tool in analyzing the overtaking maneuver, there were a few limitations to its use:

- Large computational time: In order to fully capture the various transient effects occurring during the simulation, a very fine mesh along with a small time step had to be chosen. As a result, the simulation required a significant amount of computational time to complete.

- Limited V_r: With the overset mesh method, the motion of the overset mesh was limited to no more than 1 cell per time step, resulting in a compromise between mesh refinement and desired velocity. In the case of the study conducted above, the velocity chosen was relatively small which made this less of an issue. However, should larger relative velocities be desired, they may come at the cost of accuracy.

- Scene generation: To fully capture all the effects of the flow around the bodies several scenes were generated. In order for these scenes to be of use though, each one had to be defined before the simulation was actually run. In most

cases this was a relatively straightforward process, however for some it required some guesswork to ensure adequate scales were placed in the scenes.

Despite these limitations, the simulation of the overtaking maneuver using the overset mesh and simplified vehicle models proved to be a success, highlighting several important flow interactions between the bodies.

CHAPTER 5: CONCLUSION

5.1 Conclusion

The aim of this thesis was to develop a simulation capable of modeling an overtaking maneuver using two simplified vehicle bodies, and to subsequently use the simulation to analyze the transient effects that occur during the overtaking maneuver. The research began with developing an understanding of the overset mesh methodology, and then adapting it to suit the case being studied. The overset mesh method allowed for the development of a moving mesh around the overtaking body, effectively maintaining mesh parameters around the body in question whilst still maintaining a reasonable computational time for the simulation.

With the capabilities of the overset mesh method demonstrated, the simplified Ahmed model was studied in great detail, both in isolation as well as in combination with other Ahmed bodies, to fully understand the flow characteristics expected of the body. Results from isolated Ahmed body simulations were compared to known results from studies conducted by various researchers such as Ahmed [6], Serre et al. [7], and Watkins et al. [14], to ensure that the flow was properly resolved, and force coefficients were accurately predicted, primarily the drag coefficeint. The drag coefficient predicted was within 2% of those found by Serre et al., a margin of error that can be considered acceptable for the case being studied.

Using the simulation methodology that predicted both the flow pattern and drag coefficient around an isolated Ahmed body, studies were conducted on the effects of having multiple Ahmed bodies in tandem. Studies conducted by Vino [15], Pagliarella [2], Rajamani [16], and Watts [17] showed that for two or more Ahmed bodies traveling in convoy, there was always a reduction in drag for the leading Ahmed body, while the trailing body demonstrated an unexpected increase in drag, due to the suppression of the wake of the leading body.

In addition to studies of the convoy, studies of an overtaking maneuver were also analyzed. The wind tunnel studies conducted by Noger et al. [1] and Gillerion [3] [19] provided the largest database of information for the overtaking maneuver, and were therefore the studies against which the results of the simulation were compared.

With a reasonable understanding of the expected behavior patterns associated with the overtaking maneuver, the simulation was run to completion with a relative velocity of 2 m/s applied to the overtaking body. The raw data did require some smoothing due to the significant presence of numerical noise in the system. The results for drag coefficient and side force coefficient of the overtaken body matched very well with the results from Nogers experimental study [1]. With the well correlated results between the experiment and CFD studies for the force coefficients the simulation can be considered to have captured the major flow characteristics reasonably well and a more detailed analysis into the causes for the trends in force coefficients could be conducted with a reasonable level of confidence.

In the initial stages of the maneuver, the two vehicle bodies behaved very similarly to two bodies in convoy, with the drag coefficient of the overtaking body being in-

creased slightly, while that of the overtaken body was reduced. When the overtaking body was within $1L$ of the overtaken body, the overtaken body saw a dramatic increase in drag as the overtaking body drew closer. This was due to the interaction of the high pressure region at the front of the overtaking body with the low pressure regions at the rear and side of the overtaken body. The drag coefficients of both bodies reached their respective peaks at a separation distance of $0.5L$, beyond which C_D vs distance reversed and became equal as the two bodies were side-by-side. Once the overtaking body began to pull past the overtaken body, the trends described previously were reversed, as was expected.

The results for the side force showed that the overtaken body demonstrated a maximum value of side force when the high pressure region at the front of the overtaking body was at its rear, and that the overtaking body demonstrated it's maximum value of side force, in the opposite direction to that of the overtaken body, when the positions were reversed. These results were caused by the high pressure regions of each body interacting heavily with the very low pressure region generated at the rear of each body, thereby causing a rotation on each of the bodies present. When the two bodies were side-by-side, they appeared to exert equal forces on each other in the Y-direction, but in opposite directions, a result which was as expected.

The results from the simulation correlated well with the results from various experiments and highlighted the capability of the overset mesh method to accurately capture the transient flow characteristics occurring during the overtaking maneuver. While the overset mesh method was still computationally expensive, the simulation was successful in highlighting the intricate flow patterns that occur during an over-

taking maneuver, and provides a springboard for future research.

5.2 Future Steps

With the study showing that the overset mesh method was capable of analyzing the flow around bodies undergoing an overtaking maneuver, it opened the door for several interesting projects in the future. Analysis of the effects of various factors such as V_r, yaw angle, transverse spacing, etc. can be conducted to better understand the flow effects around two bodies in the overtaking situation. In addition, studies could be conducted on more representative vehicle models such as the DriveAer model to gain an even larger understanding of these transient effects.

The relative simplicity of the overset mesh method, along with its versatility make it a very interesting tool for future research, for which this thesis aimed to be a starting point.

REFERENCES

[1] Noger C., Regardin C., Szechenyi, E., Investigation of the transient aerodynamic phenomena associated with passing manouevres. Journal of Fluids and Structures, **21** (2005), pp 231-241

[2] Pagliarella R. On the aerodynamic performance of automotive platoons featuring pre and post-critical leading forms, PhD Thesis, RMIT University (2009)

[3] Gillerion P., Noger C., Contribution to the analysis of transient aerodynamic effects acting on vehicles. SAE paper no. 2004-01-1311.

[4] Corin R.J., He L., Dominy R.G., A CFD investigation into the transient aerodynamic forces on overtaking road vehicle models. Journal of Wind Engineering and Industrial Aerodynamics **96** (2008) pp 1390-1411

[5] Uystrpruyst D. and Krajnovic S, Numerical simulation of the transient aerodynamic phenomena induced by passing manouervres. Chalmers University of Technology, Gothenburg, Sweden

[6] Ahmed S., Ramm G., And Faltin G., Some Salient Features of the Time Average Ground Vehicle Wake . SAE Transactions **93**(1984), pp 1-31

[7] Serre E et al. On simulating the turbulent flow around the Ahmed body: A French-German collaborative evaluation of LES and DES, Computers and Fluids **78** (2013) pp 10-23

[8] Hinterberger C., Garcias-Villalba M., and Rodi, W. Large eddy simulation of flow around the Ahmed body

[9] Guilmineau, E. Computational study of flow around a simplified car body. Journal of Wind Engineering and Industrial Aerodynamics **96** (2008), pp 1207-1217

[10] Minguez M., Pasquetti R., Serre E. High-order large-eddy simulation of flow over the "Ahmed body" car model. Physics of Fluids **20** (2008)

[11] Kapadia S., Roy S., Vallero M., Wurtzler K., and Forsythe J., Detached-eddy simulation over a reference Ahmed car model. AIAA paper no. 2003-0857, 2003

[12] Vino G., Watkins S., Mousley P., Watmuff J., and Prasad S. Flow structures in the near-wake of the Ahmed model. Journal of Fluids and Structures **20** (2005), pp 673-695

[13] Martinuzzi R.J. and Havell B., Turbulent flow around two interfering surface-mounted cubic obstacles in tandem arrangement, Journal of Fluids Engineering **122**(2000), pp 24-31

[14] Pagliarella R., Watkins S., and Tempia, A. Aerodynamic performance of vehicles in platoons: the influence of backlight angles, SAE paper 2007-01-1547 (2007)

[15] Vino G. An experimental investigation into the aerodynamics of a simplified passenger vehicle in isolation and in convoys, PhD Thesis, RMIT University (2005)

[16] Rajamani G.K. CFD analysis of air flow interactions in vehicle platoons, Masters thesis, RMIT University (2006)

[17] Watts A. Computational characterization of drag reduction for platooning heavy vehicles, Masters Thesis, Auburn University (2015)

[18] Yamamoto, S., Yanagimoto, K., Fukuda H., China H., Natagawa K., Aerodynamic influence of a passing vehicle on the stability of the other vehicle JSAE Review **18** (1997), pp39-44

[19] Gillerion P., Detailed analysis of the overtaking process, Journal of Mechanical Engineering **53**, 2003.

[20] Chan W., Gomez III, R. J., Rogerst, S, and Buning , P. Best practices in overset grid generation. AIAA paper no 2002-3191

[21] Houzeaux G., Eguzkitza B., Aubry R., Owen H., Vazquez M., A Chimera method for incompressible Navier-Stokes equations. International journal for for numerical methods in fluids **75** (2014) pp 155-183

[22] StarCCM+ User Manual

[23] Li Y., Paik K., Xing T., Carrica P.M., Dynamic overset CFD simulations of wind turbine aerodynamics

[24] Iaccarino G., Ooi A., Durbin P.A., Behnia M., Reynolds averaged simulation of unsteady separated flow, International Journal of Heat and Fluid Flow **24** (2003), pp 147-156

[25] Davis P.L., Rinehimer A.T., Uddin M., A Comparison of RANS-based turbulence modeling for flow over a wall-mounted square cylinder, North Carolina Automotive Research Center

[26] Gorji S. et al. A comparative study of turbulent models in a transient channel flow. Computers and Fluids **89** pp 111-123

[27] Eleni D., Athanasios T, and Dionissios M., Evaluation of the turbulence models for the simulation of the flow over a National Advisory Committee of Aeronautics (NACA) 0012 airfoil. Journal of Mechanical Engineering Research /bf 4 (2012) pp 100-111

[28] Tennekes H., and Lumley J.L. A First Course in Turbulence, MIT Press, 1972.

[29] Tran T, Kim D, Song J, Computational Fluid Dynamic analysis of a floating offshore wind turbine experiencing platform pitching motion, Energies **7** (2014)

[30] Browand F. and Hammache M. The limits of drag behavior for two bluff bodies in tandem, Vehicle Aerodynamics (2004)